The Dissertation Committee for Ying Sun Certifies that this is the approved version of the following dissertation:

Role of Mesophyll CO_2 Diffusion and Large-Scale Disturbances in the Interactions between Climate and Carbon Cycles

Committee:

Robert E. Dickinson, Supervisor

Rong Fu

Zong-Liang Yang

Kenneth R. Young

Lianhong Gu

Role of Mesophyll CO_2 Diffusion and Large-Scale Disturbances in the Interactions between Climate and Carbon Cycles

by

Ying Sun, B.S.

Dissertation

Presented to the Faculty of the Graduate School of
The University of Texas at Austin
in Partial Fulfillment
of the Requirements
for the Degree of

Doctor of Philosophy

The University of Texas at Austin
May, 2013

Dedication

For my mother, who has instilled in me the value of knowledge and wisdom and offered me an example of a great woman.

For my father, who has taught me to know the world and swept away all the difficulties I have encountered in my life.

Acknowledgements

I am very grateful to my supervisor Dr. Robert Dickinson for his support and advice throughout my years as a graduate student. He encouraged me to develop my own research interests, guided me when difficulties were encountered, and reminded me not to lose the overall picture. I have benefitted tremendously from his deep knowledge, far insights, and warmth of his smiles. Dr. Lianhong Gu, my mentor in Oak Ridge National Laboratory, has been continuously clarifying difficult scientific issues for me, confronting me to work on challenging problems, and comforting me when I encountered setbacks. The classes taught by Drs. Rong Fu, Zong-Liang Yang, and Kerry Cook in the first year of my graduate study enlightened me and switched me from a “remote sensor” to a “climate modeler”. Dr. Kenneth Young, who let me join his class in the last minute, has broadened my scientific perspective and deepened my understanding of ecological effects of disturbances. My capacity for scientific reasoning and skills has been greatly enhanced by intensive communication with my mentors at Max Planck Institute for Biogeochemistry in Germany, Drs. Sonke Zaehle, Markus Reichstein, and Nuno Carvalhais. Their scientific enthusiasm and hardworking spirit impressed me and motivated me to work harder and better. I also thank the following scientists who have given me insights and helpful discussions: Drs. Yongjiu Dai, Mac Post, Gordon Bonan, Peter Thornton, Martin Jung, Christian Beer, Miguel Mahecha, Jiafu Mao, Xiaoying Shi, Xiaojuan Yang, Yaxing Wei, Guo-Yue Niu, Kaicun Wang, Xiaoyan Jiang, Hua Su, Sergey Fomel, and Clark Wilson. Special thanks go to Philip Guerrero, who has been clarifying me complicated University rules and making my life a lot easier. My group colleagues, Dr. Bing Pu, Wenting Fu, Binyan Yan, Kai Wang, Hua Yuan, Jamie Wentz,

Dr. Shaikh Muhammad, and David Spindler, have been providing me countless help both scientifically and technically.

The coauthors of my published papers have made great contributions to my research by providing datasets, insightful comments to the science, and detailed polishing to my writing.

I am in debt to my parents, who forgive me to be 11, 000 miles away for so long to pursue my Ph.D. They injected me tremendous powers when I was sick; they helped me fulfill all my dreams when I was a child; they made me better in every way possible. Whenever I need help and I turn around, they are always there. Without them, I cannot complete my study. I thank my husband Bo, who forgives me to have spent so much time in office and makes me realize how lucky I am in the journey of pursuing my degree.

This research was funded by the National Science Foundation, the Department of Energy, the Higher Education Research Experiences at Oak Ridge National Laboratory, and the Jackson School of Geosciences.

Role of Mesophyll CO_2 Diffusion and Large-Scale Disturbances in the Interactions between Climate and Carbon Cycles

Ying Sun, Ph.D.

The University of Texas at Austin, 2013

Supervisor: Robert E. Dickinson

Reliable prediction of climate change and its impact on and feedbacks from terrestrial carbon cycles requires realistic representation of physiological and ecological processes in coupled climate-carbon models. This is hampered by various deficiencies in model structures and parameters. The goal of my study is to improve model realism by incorporating latest advances of fundamental eco-physiological processes and further to use such improved models to investigate climate-carbon interactions at regional to global scales. I focus on the CO_2 diffusion within leaves (a key plant physiological process) and large-scale disturbances (a fundamental ecological process) as extremely important but not yet in current models.

The CO_2 diffusion within plant leaves is characterized by mesophyll conductance (g_m), which strongly influences photosynthesis. I developed a g_m model by synthesizing new advances in plant-physiological studies and incorporated this model into the Community Land Model (CLM), a state-of-art climate-carbon model. I updated associated photosynthetic parameters based on a large dataset of leaf gas exchange measurements. Major findings are: (1) omission of g_m underestimates the maximum carboxylation rate and distorts its relationships with other parameters, leading to an incomplete understanding of leaf-level photosynthesis machinery; (2) proper

representation of g_m is necessary for climate-carbon models to realistically predict carbon fluxes and their responsiveness to CO_2 fertilization; (3) fine tuning of parameters may compensate for model structural errors in contemporary simulations but introduce large biases in future predictions. Further, I have corrected a numerical deficiency of CLM in its calculation of carbon/water fluxes, which otherwise can bias model simulations.

Large-scale disturbances of terrestrial ecosystems strongly affect their carbon sink strength. To provide insights for modeling these processes, I used satellite products to examine the temporal-spatial patterns of greenness after a massive ice storm. I found that the greenness of impacted vegetation recovered rapidly, especially in lightly and severely impacted regions. The slowest rebound occurred over moderately impacted areas. This nonlinear pattern was caused by an integrated effect of natural regrowth and human interventions.

My results demonstrate mechanisms by which terrestrial carbon sinks could be significantly affected and help determine how these sinks will behave and so affect future climate.

Table of Contents

List of Tables

List of Figures

Chapter 1: Introduction

This dissertation aims to achieve better understanding of the coupling between terrestrial ecosystems and climate change and how human perturbation alters such coupling beyond fossil fuel emission. The major tool to advance this understanding is the state-of-art coupled climate-carbon cycle models, which are yet challenged by predictive uncertainty. As a modeler, I attempt to improve the biogeochemical realism of these models, focusing on fundamental processes, and so as to enhance the model predictability for the future fate of our climate system. My research work embodied in the chapters of this dissertation informs the principles that should be integrated into the studies of global environmental changes.

1.1. MOTIVATION AND OBJECTIVES

Climate warming is driven by increasing radiative forcing that arises primarily from rising concentrations of atmospheric greenhouse gases, especially CO_2 (Dickinson 2012; Denman et al. 2007). The atmospheric CO_2 is increasing at a slower rate than total emissions from fossil fuels and land use changes, with only ~43% of annual emissions staying airborne on average in the last five decades and the rest consistently removed by natural carbon sink reservoirs: ocean and land (Keeling et al. 1996, 1995; Canadell et al. 2007; Le Quéré et al. 2009). These carbon sinks alleviate the radiative warming. On the other hand, the strength of carbon sinks critically depend on climate, including long-term climate change (e.g., Nemani et al. 2003), climate variability such as ENSO (e.g., Le Quéré et al. 2010; Lintner 2002), climate extremes, e.g., heatwaves and droughts (e.g., Phillips et al. 2009; Ciais et al. 2005), and climate perturbation from volcanic eruption, e.g., Mt. Pinatubo (e.g., Angert et al. 2004; Gu et al. 2003a). So climate and carbon cycles strongly interact.

Coupled climate-carbon cycle models generally predict a diminishing capacity in the future of carbon uptake by both ocean and land, leading to a positive climate-carbon feedback (Friedlingstein et al. 2006; Fung et al. 2005; Cox et al. 2000). However, the extent to which carbon sink strength is predicted to change by the end of 21st century and the estimated magnitude of the climate-carbon feedback differ remarkably among models. Some studies have suggested that the decline of carbon uptake efficiency may be already underway in recent decades (Le Quéré et al. 2009; Canadell et al. 2007), because of negative responses of carbon cycle processes to climate change and variability, e.g., droughts (Zhao and Running 2010) and autumn warming (Piao et al. 2008). However, these reported declines were questioned (e.g., Sarmiento et al. 2010; Knorr 2009), and some other studies found increases of carbon uptake (e.g., Ballantyne et al. 2012), supported by the increasing carbon storage in the intact tropical forests across Amazon and Africa (Phillips et al. 2008; Lewis et al. 2009; Pan et al. 2011). These findings imply that changes in carbon sinks are highly uncertain, challenging the current predictability of future atmospheric CO_2 and its induced warming. Therefore, it is critical to reduce the uncertainties.

Land, or its terrestrial ecosystem, is a large carbon sink on Earth, which balances ~30% of annual carbon emissions over a historical average (Canadell et al. 2007; Le Quéré et al. 2009). It absorbs carbon from the atmosphere through plant photosynthesis and stores in vegetation and soils. Land ecosystems also release carbon to the atmosphere primarily in the form of CO_2 by soil (i.e., microbial activities) and plant respiration, and also by disturbance processes (e.g., deforestation and afforestation, fires, insect outbreaks). The net land-atmosphere exchanges of CO_2, i.e., the differences of these counteracting processes, have been carbon sinks in the last 30 years (Denman et al. 2007), largely a consequence of secondary forest regrowth, fire suppression, climate changes, longer growing seasons, carbon and nitrogen fertilizations (Schimel et al. 2001). In addition, these factors are not independent but interact to influence carbon sink; for example, secondary forest regrowth can be stimulated by nitrogen fertilization (e.g., Yang et al. 2010), and growing season lengthens as a benefit from a warming climate. Land carbon sinks show large interannual variability, dominating the observed persistent year-to-year fluctuation of atmospheric growth rate of CO_2 (Le Quéré et al. 2009). This variability is driven by climate variations in precipitation, surface temperature, and radiation (Sitch et al. 2010; Mercado et al. 2009).

Unlike the well-constrained estimates of oceanic uptake (e.g., Sabine et al. 2004), quantification of land carbon sinks, however, remains quite uncertain (Denman et al. 2007). In particular, regional partitioning of the global land sink is not very consistent: with some earlier studies largely attributing this sink to northern extratropical areas (e.g., Schimel et al. 2001), while others showing weaker northern but stronger tropical land uptake (e.g., Stephens et al. 2007). The longitudinal attribution of the northern land sinks among Europe, North America, and North Asia is even more uncertain (Denman et al. 2007; Schimel et al. 2000). Uncertainty also remains as to the contributions from various mechanisms (e.g., CO_2 fertilization, changing climate, nutrient limitation, or forest regrowth) that drive the land-atmosphere exchanges differentially at different time- and spatial scales (Schimel et al. 2000; Norby et al. 2005; Pacala et al. 2001; Zaehle and Dalmonech 2011; Luo et al. 2004; Bonan 2008a). Furthermore, human interventions exacerbate these existing uncertainties by modifying natural mechanisms, e.g., anthropogenic deposition of nitrogen fertilizer, tropospheric ozone pollution that inhibits photosynthesis, and aerosol emissions that may enhance CO_2 uptake by cooling the climate and by inducing more diffuse radiation (Gu et al. 2003a; Angert et al. 2004). Thus, identifying mechanisms, both natural and human processes, that are responsible for uncertainties in global and regional carbon budgets is critical not only for refining current knowledge in biogeochemical cycling of carbon but also for reliably predicting future climate and hence informing proper mitigation policies for climate changes. My dissertation research aims to disentangle some aspects of uncertainties involved in terrestrial carbon cycles with a human dimension, and to advance scientific understanding of climate-carbon interactions.

1.2. COUPLED CLIMATE-CARBON MODELS

A major tool to achieve my research goal is the state-of-art coupled climate-carbon models, which explicitly integrate the biogeochemical carbon cycling and its feedbacks to climate change (Friedlingstein et al. 2006). These models have been intensively applied to simulate historical changes of carbon fluxes and storage (e.g., Cramer et al. 2001; Bonan and Levis 2010; Sitch et al. 2010). They have been evaluated against various data streams that are available in certain time frames, including satellite observations, eddy-covariance fluxes, and *in-situ* inventory measurements (e.g., Randerson et al. 2009; Luo et al. 3857; Piao et al. 2013; Mao et al. 2012; Keenan et al. 2012a; Beer et al. 2010; Bonan et al. 2011, 2012, 2013). Overall they are capable of depicting how environment, e.g., temperature, moisture, and radiation, shapes ecosystem structures and functions, as were found from observations (e.g., Law et al. 2002; Nemani et al. 2003). Although current models have achieved first-order accuracy due to injection of constraining data streams, they still suffer major deficiencies for predicting future changes, such as in simulating certain variables (e.g., decomposition rate, Bonan et al. 2013) and in achieving proper model sensitivity to environmental conditions (e.g., moisture and temperature, Piao et al. 2013).

Furthermore, models should be able to predict the future for other issues about which humans are more concerned yet observations are unavailable. Many attempts have been made to perform inter-comparisons of coupled climate-carbon models in their projections of the coming century (e.g., Friedlingstein et al. 2006; Sitch et al. 2010). The terrestrial carbon storage is generally modeled to increase with rising atmospheric CO_2 by which plant photosynthesis and growth can be stimulated (a negative feedback), and to decrease with warming temperatures that can induce higher plant respiration and soil decomposition rate (a positive feedback, e.g., Friedlingstein et al. 2006). Collectively, the latter processes, i.e., the positive feedback, have generally dominated the modeled terrestrial carbon storage in the future (Friedlingstein et al. 2006). Nevertheless, the magnitude of both the positive and negative feedbacks as well as their resulting net effects differ remarkably among coupled climate-carbon models. The differences in the net feedback lead to a large spread of an additional 20 to 220 ppm in the predicted growth of atmospheric CO_2 and an additional warming uncertainty between 0.1 and 1.5 ^{O}C under the A2 emission scenario (Friedlingstein et al. 2006). These feedback factors, as estimated by models, strongly depend on the processes that are included in the model (Dickinson 2012), whose degree of realism in turn determines the magnitude of uncertainty. For example, more recent studies (Sokolov et al. 2008; Bonan and Levis 2010; Zaehle et al. 2010b), with inclusion of nitrogen dynamics, found that nitrogen significantly constrains the stimulation of carbon uptake by CO_2 fertilization (i.e., weakening of the negative feedback). They also showed that warming promotes nitrogen release from soils. The warming-induced nitrogen release partially alleviates nitrogen limitation and enhances plant growth, which hence compensates for the soil carbon loss under warmer temperature (i.e., weakening of the positive feedback). The joint effect of nitrogen cycling is a more positive climate-carbon feedback, since the latter process shows a lesser impact (Bonan 2008a; Bonan and Levis 2010). Again, carbon-nitrogen interactions add new uncertainties, demonstrated by inconsistent estimates of future carbon storage by different modeling studies (Zaehle et al. 2010a; Thornton et al. 2009). Inclusion of other nutrient limitations such as phosphorus (e.g., Zhang et al. 2011; Wang et al. 2010) or ozone effects (e.g., Lombardozzi et al. 2012) may amplify or reduce model uncertainties, but such roles in modifying climate-carbon feedbacks have not been quantified yet.

To reduce model uncertainties, considerable efforts have been made. For example, Xia et al. (2013) developed techniques to decompose the modeled terrestrial carbon storage term into traceable components so as to more objectively attribute uncertainty to different processes. Model-data fusion approaches (e.g., Wang et al. 2009; Keenan et al. 2012b), which are more commonly used to minimize uncertainties associated with both model and data, are plausible but provide limited information for future predictions.

My philosophy to reduce the predictive uncertainty of models is to improve their realism in representing fundamental processes, such as those reviewed in section 1.1. This is because models should be capable of forecasting the future, which depends strongly on credibility of the model "process" description.

Throughout this dissertation, my research works are heavily built upon models, since they are currently the best tools available to test scientific hypotheses, to pin down mechanisms, and finally to improve understanding of carbon-climate couplings and feedbacks at a continuum of spatial- and timescales.

1.3. RESEARCH FOCUSES

A number of gaps remain between process-based studies and modeling community. In this dissertation, I focus on two principal pathways along which coupling between climate and carbon cycles can be better represented by models: plant physiological and ecological processes. This coupling is explored at spatial scales from plant cells, i.e., mesophyll diffusion process inside leaves (a critical physiological process), to large-scale disturbances (an important ecological phenomenon). These two processes are key aspects of terrestrial carbon cycles; yet their representations in models are either nonexistent or remain crude.

1.3.1. The Mesophyll Diffusion Process inside Leaves

My interest to study the mesophyll diffusion process of CO_2 inside leaves comes from its strong constraints on leaf photosynthesis. During photosynthesis, CO_2 moves from atmosphere to the leaf surface, and then diffuses to the leaf intercellular air space through stomata, and finally transfers to the site of caboxylation inside the leaf chloroplast through leaf mesophyll, i.e., mesophyll diffusion of CO_2. The three processes jointly control the actual CO_2 concentration available for carbon assimilation. They are characterized with leaf boundary layer conductance, stomatal conductance, and mesophyll conductance (or referred to as internal conductance) for CO_2 transfer. The first two conductance terms have been represented in large-scale models for a long time. Mesophyll conductance, however, has yet to be accounted for in these models.

Plant physiologists have long recognized that the mesophyll CO_2 transfer is an important process limiting photosynthesis (e.g., Harley et al. 1992; Niinemets et al. 2009a; von Caemmerer and Evans 2010) and consistently suggested that this process should be accounted for in global change studies (e.g., Niinemets et al. 2011). Mesophyll conductance has been measured around the world for hundreds of species. A consistent finding is that it is sufficiently small to substantially decrease CO_2 concentrations at the sites of carboxylation, hence limiting photosynthesis comparable in magnitude to that of stomatal conductance. The reduction of photosynthesis caused by this limitation can be up to 25% for crop species and up to 75% for natural vegetation (e.g., Terashima et al. 2006). Studies have also shown that mesophyll conductance is a major contributor to photosynthesis reduction under water stress, perhaps more profound than the limitation of stomata and biochemical capacity (Keenan et al. 2010a; Egea et al. 2011). Niinemets et al. (2011) highlighted the role of mesophyll conductance in regulating photosynthesis capability under elevated CO_2.

A limited number of canopy-level models have considered mesophyll conductance (Williams et al. 1996; Le Roux et al. 2001; Cai et al. 2008; Keenan et al. 2010a; Egea et al. 2011; Oliver et al. 2012), providing local-scale insights concerning its effect on ecosystem functioning. However, to my knowledge, no attempt has been made to represent mesophyll conductance for large-scale simulations. By omitting representation of this diffusion process, modelers implicitly assume that mesophyll conductance is infinite and thus the CO_2 concentration at the site of carboxylation in the leaf chloroplasts is the same as it is inside the leaf intercellular air space. This assumption is clearly invalid according to the findings from physiological studies.

My overall strategy is to develop a modeling framework of mesophyll conductance that can be broadly applied to global biomes, and by implementing this framework into carbon models to address its global and regional impact on carbon cycles.

1.3.2. Large-Scale Disturbances

My impetus to study disturbances emerges because of their disproportional role in shaping ecosystem structures and functioning (e.g., Gutschick and BassiriRad 2003;

Amiro et al. 2010). Disturbances are irregularly occurring damage to ecosystems, driven by temporal shifts of external forcings both naturally or human-induced (Gutschick and BassiriRad 2003). Disturbances can trigger large transfers of carbon from living biomass to dead organic matter and subsequent decomposition, causing dramatic and sudden shifts of sizes of and fluxes between various carbon pools (Girardin et al. 2009). They are distinguished from the influence of “mean climate” on ecosystems due to their disproportional impacts and persistent “post-effects” (Gutschick and BassiriRad 2003), and consequently pose a high risk to terrestrial carbon sinks. A number of observational records are available in the current literatures, reporting the powerful ecological, biogeochemical and biophysical influences of fires (e.g., Randerson et al. 2006; Page et al. 2009), insect outbreaks (e.g., Kurz et al. 2008), hurricanes (e.g., Chambers et al. 2007; Zeng et al. 2009), unseasonable freezes (e.g., Gu et al. 2008), massive ice storms (e.g., Millward and Kraft 2004; Zhou et al. 2011a), droughts (e.g., Allen and Breshears 1998; McDowell et al. 2008; Phillips et al. 2009), and heat waves (e.g., Ciais et al. 2005).

There is a growing awareness that climate change can stimulate an upward trend of occurrences and intensities of extreme climate events (e.g., Girardin et al. 2009; Meehl et al. 2007) that in turn can trigger disturbances. Therefore, their impacts and feedbacks must be studied as an integral part of climate-carbon interactions because such events, once having occurred, may be the primary driver of the transformation of ecosystem structures and functions and alteration of terrestrial carbon cycle feedbacks to climate change, overwhelming the role of mean climatic variables, which are commonly used for predictions (Gutschick and BassiriRad 2003). There is a growing investigation of impacts and ecological feedbacks of disturbances in the context of climate change (e.g., Gutschick and BassiriRad 2003; Jentsch et al. 2007; Gu et al. 2008; Running 2008).

The role of disturbances on short and long-term carbon dynamics in terrestrial ecosystems has been identified as one of the critical uncertainties. However, their influence is not adequately represented in the current climate-carbon cycle models (Girardin et al. 2009; Running 2008). This study attempts to better represent the forcing and feedbacks of disturbances on terrestrial carbon cycle in current models, and to better quantify the exchange of CO2 between ecosystems and atmosphere.

1.4. ORGANIZATION OF THE DISSERTATION

The studies on mesophyll conductance involve development of a modeling framework that can be widely applied to global biomes, implementation of developed representation to global models, and recalibration of photosynthetic parameters that coincide with inclusion of mesophyll conductance. This dissertation starts from a leaf-level investigation by a comprehensive meta-analysis of how mesophyll conductance (g_m) shapes the values of photosynthetic parameters and functional relationships among them (Chapter 2). This study paves the ways for a full implementation of g_m model in global carbon models. Chapter 3 develops a global g_m model based on synthesizing the latest advances of field plant physiological studies. This g_m model is further implemented to the Community Land Model (CLM), one of the state-of-art climate models that include terrestrial carbon cycles, to simulate its effect on global vegetation productivity, i.e., GPP. Chapter 4 extends the studies of mesophyll conductance to its role on GPP responsiveness to historical CO_2 changes. Implications for terrestrial carbon uptake strength in the future are also discussed. Chapter 5 addresses a numerical issue of CLM in its calculation of photosynthesis, which was accidentally found during the g_m implementation. The consequence of this numerical deficiency is provided. With intent to represent large-scale disturbances in carbon models, I develop a unified theoretical framework to quantify their short- to long-term impact on terrestrial ecosystems. A case study, i.e., the massive 2008 Chinese ice storm, is applied to verify its effectiveness by synthesizing satellite observation and ground measurements (Chapter 6). The post-disturbance evolution of impacted ecosystems is fully evaluated with integrated natural and anthropogenic perspectives. Finally, major findings in all the research presented are summarized and future directions as well as implications for model development and predictability are discussed (Chapter 7).

Chapter 2: Differential effects of mesophyll conductance on fundamental photosynthetic parameters and their relationships estimated from leaf gas exchange measurements

2.1. ABSTRACT

Systematic studies are needed to fully understand how mesophyll conductance (g_m) affects photosynthetic parameters and their relationships estimated from A/C_i curves. We analyzed worldwide measurements of over 100 C_3 species covering all major plant functional types from herbaceous temperate plants to woody tropical species with growth environments ranging from greenhouse to natural vegetation. Furthermore, extensive model simulations were conducted to corroborate findings from measurement analyses. We found the assumption of infinite g_m results in up to a 75% underestimation for maximum carboxylation rate V_cmax, 60% for maximum electron transport rate J_max, and 40% for triose phosphate utilization rate T_u. V_cmax is most sensitive, J_max is less sensitive, and T_u has the least sensitivity to the variation of g_m. As a consequence of the differential effects of g_m, the ratios of J_max to V_cmax, T_u to V_cmax, and T_u to J_max are all overestimated under the infinite g_m assumption. Also, this assumption limits the freedom of variation of estimated parameters and artificially constrains parameter relationships to stronger shapes. A nonlinear function can be used to convert the parameters estimated under the infinite g_m assumption to proper values if an estimated g_m is available, which is very useful for large-scale carbon cycle modeling.

2.2. INTRODUCTION

Leaf gas exchange measurements that relate CO_2 assimilation (A) to changes of CO_2 partial pressure in leaf substomatal cavity (C_i), i.e., the so-called A/C_i curves, provide crucial information on photosynthetic processes (Wullschleger 1993; Long et al.

1996; Long and Bernacchi 2003; von Caemmerer 2000). Key biochemical parameters of photosynthesis can be estimated by fitting to A/C_i curves the mechanistic Farquhar-von Caemmerer-Berry (FvCB) model (Farquhar et al. 1980; Farquhar and von Caemmerer 1982) as modified by Sharkey (1985) and by von Caemmerer (2000). Parameter estimation approaches with the FvCB model have been discussed previously (Dubois et al. 2007; Ethier et al. 2006; Gu et al. 2010; Manter and Kerrigan 2004; Miao et al. 2009; Sharkey et al. 2007; Yin et al. 2009). The estimated parameters are then related to physiological or environmental variables such as leaf morphology and nutrient contents, canopy environmental gradients, and soil conditions to characterize the underlying eco-physiological processes (Ellsworth et al. 2004; Hikosaka 2005; Niinemets et al. 2001; Warren et al. 2003; Busch et al. 2013; Onoda et al. 2005a,b). They are also employed in ecosystem and land surface models to simulate responses of terrestrial carbon and water cycles to environmental variations at various spatial and temporal scales (Kattge et al. 2009; Bonan et al. 2011).

The theoretical framework of the FvCB model requires the CO_2 partial pressure at the carboxylation site, i.e., the chloroplast (C_c), not C_i (Niinemets et al. 2009a). Most previous studies, however, have ignored the internal diffusion process of CO_2 from leaf substomatal cavity to chloroplast and applied the FvCB model directly to C_i, a practice that compromises the theoretical integrity of the FvCB model. The integrity of the model can be maintained if it is extended to explicitly consider this internal diffusion process from leaf substomatal cavity to chloroplast, which can be characterized by a parameter referred to as mesophyll conductance (g_m) (Ethier and Livingston 2004; Gu et al. 2010; Niinemets et al. 2009a). The extended FvCB model can then be fitted to the A/C_i curves to estimate biochemical parameters, together with g_m. In this way, C_c, instead of C_i, is directly applied to the FvCB model, as if the A/C_c curves were being fitted, and the parameters obtained can be appropriately termed A/C_c -based parameters to differentiate them from the conventional A/C_i -based parameters.

The mesophyll conductance g_m controls the CO_2 drawdown from C_i to C_c (Evans et al. 1986; Niinemets et al. 2009a,b). This drawdown vanishes only if g_m is infinitely large. However, plant species have a finite value of g_m, which can significantly affect photosynthetic rates (Evans et al. 1986; Ethier and Livingston 2004; Ethier et al. 2006; Flexas et al. 2008; Niinemets et al. 2009b; Warren 2008). Without explicitly considering g_m, the A/C_i-based estimates of key biochemical parameters as well as the relationships among them may be biased (Niinemets et al. 2009a,b,c). Furthermore, the use of biased A/C_i-based values of these parameters to predict photosynthesis under field conditions may either overestimate or underestimate actual photosynthesis, depending on the magnitude of g_m and environmental stresses (Niinemets et al. 2009a,b,c).

A vast amount of A/C_i curves have already been analyzed without explicit consideration of g_m. Photosynthetic parameters derived from such analyses have been widely used in process-based studies of plant physiology, ecology, and global change biology as well as in local, regional and global modeling research. Evaluation of the reliability of these studies requires a clear understanding of the effects of g_m on photosynthetic parameter estimation. Previously-published papers that included raw A/C_i data would allow a refitting to estimate the A/C_c-based parameters with explicit consideration of g_m using approaches such as that of Gu et al. (2010). Unfortunately, the large majority of the past papers did not include raw data, making refitting unfeasible. A systematic and quantitative understanding of how g_m affects the values of key photosynthetic parameters as well as the functional relationships among them is needed in order to make better use of the rich resources represented in the past literature of A/C_i curve analyses.

Mesophyll conductance g_m varies widely across leaf traits and plant functional types (Flexas et al. 2008; Niinemets et al. 2009b; Syvertsen et al. 1995), light gradients inside plant canopies (Hanba et al. 2002; Piel et al. 2002; Laisk et al. 2005; Terashima et al. 2006; Warren et al. 2007; Montpied et al. 2009; Han et al. 2010), and with environmental stress factors (Chazen and Neumann 1994; Miyazawa et al. 2008). For a small set of samples with very limited variations in g_m and photosynthetic capacities, a simple linear relationship may be used to convert the biased A/C_i-based parameters to the corresponding unbiased A/C_c-based parameters (Zeng et al. 2010). But it is unlikely that a universal correction factor exists across species and environmental gradients given the large variations of g_m (Niinemets et al. 2009b). Schemes that can achieve this conversion will at least have to use g_m as input. Such schemes will be very useful in facilitating the transition from A/C_i-based to A/C_c-based parameter estimation and in large-scale terrestrial carbon cycle modeling.

This study presents a systematic evaluation of the effects of g_m on the values and relationships of photosynthetic parameters V_cmax (the maximum carboxylation rate), J_max (the maximum electron transport rate) and T_u (the triose phosphate utilization rate) estimated through A/C_i analyses. An emphasis is placed on the functional relationships among these parameters because accurate quantification of these relationships will improve the understanding of the photosynthetic machinery at leaf scale. We are also interested in developing practical solutions for large-scale carbon cycle models should such models enable representation of g_m. We build upon past insightful work by Ethier and Livingston (2004), Ethier et al. (2006), Evans et al. (1986), Niinemets et al. (2009a,b,c), and Warren (2008), among others, to highlight the importance of g_m in the study of photosynthesis from leaf to canopy. We use worldwide measurements of leaf gas exchange of more than 100 species from all major plant functional types and climates to identify general patterns. The data collection was made possible by a free web-based tool (http://leafweb.ornl.gov/), which conducts automated A/C_i and A/C_c curve analyses and also provides an estimate of g_m. The findings from these field measurements are further corroborated with analyses based on systematically simulated A/C_i curves (see the 2.3 for details). The following specific questions are addressed in this study:

1. For a given value of g_m, how do the 'apparent', i.e., A/C_i–based V_cmax, J_max and T_u parameters (denoted as $V_\mathrm{cmax,i}$, $J_\mathrm{max,i}$ and $T_\mathrm{u,i}$, respectively), vary with the 'true', i.e., A/C_c– based V_cmax, J_max and T_u parameters (denoted as $V_\mathrm{cmax,c}$, $J_\mathrm{max,c}$ and $T_\mathrm{u,c}$, respectively)?
2. Are different A/C_i–based parameters equally sensitive to the variation of g_m?
3. For a given set of the A/C_c–based parameters, how do the A/C_i–based parameters vary with g_m?
4. How do the relationships among $V_\mathrm{cmax,c}$, $J_\mathrm{max,c}$ and $T_\mathrm{u,c}$ differ from those among $V_\mathrm{cmax,i}$, $J_\mathrm{max,i}$ and $T_\mathrm{u,i}$?
5. Is there a mathematical function that can be used to accurately convert the A/C_i–based parameters to the A/C_c –based parameters for a wide range of photosynthetic capacities, g_m values, and environmental factors?

2.3. METHODS

Both actual and simulated A/C_i curves are used in this study. The simulated A/C_i curves, although artificial, allow the true values of parameters of interest to be controlled and thus make it possible to answer some questions with absolute certainty (e.g., for a given value of the true, A/C_c– based parameter, how does the apparent, A/C_i–based parameter vary with g_m?). The analysis of the simulated A/C_i curves also provides an independent check on findings obtained from actual A/C_i curves. Both the actual and simulated A/C_i curves are analyzed with and without explicit consideration of g_m. The obtained parameters are then compared (see Section 2.4).

The term mesophyll conductance as used in this study is defined technically as the ratio of net photosynthetic rate (A_{net}) to the difference between C_i and C_c, that is, $g_m = A_{net}/(C_i - C_c)$, consistent with Fick's law of diffusion and definitions of other conductance terms such as stomatal and boundary-layer conductance. The same phrase has also been used to describe the initial slope of A/C_i curves in some previous papers (e.g., Sinclair et al. 1977) as well as in current manuals of some instruments of leaf gas exchange measurements (e.g. http://www.licor.com/env/products/photosynthesis/manuals.html, LI-6400/LI-6400XT Instruction Manual, Version 6). These two uses of the term mesophyll conductance would become identical only if C_c equals zero, which is unlikely to be true as it would imply a zero carboxylation rate for changing C_i. To avoid confusion, we suggest that the concept of mesophyll conductance be used exclusively in the framework of Fick's law of diffusion.

2.3.1. A/C_i Curve Measurements

The measurements of A/C_i curves used in this study were made on over 100 C_3 plant species in Brazil, China, France, Ireland, Panama, and USA. In total, more than 1000 measured curves were actually used in the analysis. Although LeafWeb had accumulated more curves, we excluded those that did not yield adequate fitting. The standards used to select measured curves were detailed in Gu et al. (2010) and briefly described later in the A/C_i curve fitting subsection. The Table 2.1 lists the species and their locations. The functional types of these species cover grasses, herbs, crops, shrubs, and trees (deciduous and evergreen broadleaf and conifers). They came from diverse growth environments, including greenhouses (seed germinations or root cuttings), plantations, and natural vegetation. The climates ranged from temperate to tropical. Both juvenile and adult individuals were used in the study. The species were either native to their local environments or introduced. All A/C_i curves were measured with Li-6400 portable photosynthetic systems (LiCor Environmental Sciences, Lincoln, Nebraska, USA). Measurements used the instrument manual instructions as reference and generally followed standard protocols recommended in the literature (Long et al. 1996; Long and Bernacchi 2003). Targeted light response curves were used to ensure that light intensities were set at saturating levels appropriate to species and their growth environments. Leaf temperatures were controlled according to ambient air temperatures and relative humidities were set generally between 55% and 75%. Flow rates were mostly between 300 to 500 mol/s. CO_2 injectors were used to control reference CO_2 in typical sequences starting from a value close to ambient (e.g., 400 ppm), decreasing to a minimum value (e.g., 50 ppm), returning to the starting value (as a check point), and then increasing to a maximum value (e.g., 1500 ppm). The reference and sample chambers were matched manually or automatically as needed. Ample times were allowed for leaves to adapt to chamber environment and to changes in CO_2 concentrations. For coniferous species, variables and parameters were based on projected leaf areas. Quality controls of measured A/C_i curves are described later in the A/C_i curve fitting subsection.

2.3.2. A/C_i Curve Simulations

The simulated A/C_i curves were generated with the FvCB model extended with the g_m representation. The extended FvCB model was fully described by Gu et al. (2010) and will not be repeated here. The simulation procedures were adapted from Gu et al. (2010). The values of key photosynthetic parameters and sampling points were all selected randomly except for certain constraints that were set to either satisfy the conditions required by the FvCB model or to answer particular questions.

More specifically, each simulated A/C_i curve contained 15 points and each point in a curve was limited either by Rubisco, or by RuBP regeneration, or by the triose phosphate utilization. For a curve to be valid, all three limitation states must occur in the same curve in an orderly fashion with at least 3 points for Rubisco, 3 points for RuBP regeneration, 2 points for TPU. The minimum number requirements for limitation states depend on the number of state-specific parameters and are consistent with the analyses of measured A/C_i curves (Gu et al. 2010). They ensure that no over-fitting occurs and the actual parameters used in generating the A/C_i curves can be properly retrieved during the curve fitting with explicit consideration of mesophyll conductance. The FvCB model expects that the Rubisco-, RuBP-, and TPU- limited points occupy the low, intermediate, and high ranges of CO_2, respectively, along the C_i (C_c) axis. Gu et al. (2010) gave a detailed proof for this pattern. The C_i values of the 15 points of a simulated A/C_i curve were, respectively, 5, 10, 15, 20, 25, 30, 35, 40, 45, 50, 55, 60, 70, 80, and 90 Pa, all multiplied by a factor that randomly varied between 0.5 to 1.5. This scheme of generating C_i values was designed such that the obtained 15 C_i values were distributed realistically along the C_i axis. The randomness ensures that the C_i values varied from curve to curve. We experimented with different sequences of C_i values and did not find any qualitative difference in terms of the final results reported in this study, indicating the random process is adequate in generating representative C_i values for simulated A/C_i curves.

Different A/C_i curves were simulated by varying the values of $V_{cmax,c}$, $J_{max,c}$, $T_{u,c}$, g_m and the day respiration R_d. These parameters were varied either systematically or randomly, depending on what specific questions were addressed. Note that an A/C_i curve cannot be produced by any arbitrary combination of $V_{cmax,c}$, $J_{max,c}$, and $T_{u,c}$. Gu et al.

(2010) proved that the FvCB formulation of photosynthesis requires the following inequality to hold for all three limitation states to occur in the same A/C_i curve:

$$4V_{\mathrm{cmax,c}} > J > 12T_{\mathrm{u,c}}. \tag{2.1}$$

Here J is the actual electron transport rate and is a function of $J_{\mathrm{max,c}}$ and the incident light level on the leaf. The inequality in Equation 2.1 is a necessary condition for the orderly occurrence of the three limitation states along the C_i axis of an A/C_i curve. Thus, we imposed this condition when the parameter sets were selected.

To determine how $V_{\mathrm{cmax,i}}$ changes with $V_{\mathrm{cmax,c}}$ for a given g_m, or with g_m for a given $V_{\mathrm{cmax,c}}$, $V_{\mathrm{cmax,c}}$ and g_m were varied in prescribed intervals with nested loops (the variation in one parameter occurs within the variation of the other) while the values of $J_{\mathrm{max,c}}$ and $T_{\mathrm{u,c}}$ were randomly generated. If the randomly generated values of $J_{\mathrm{max,c}}$ and $T_{\mathrm{u,c}}$ did not satisfy the inequality Equation 2.1 or if the minimum number requirements for Rubisco-, RuBP regeneration- and TPU-limited states were not met, these values were discarded and new values of $J_{\mathrm{max,c}}$ and $T_{\mathrm{u,c}}$ were randomly generated (but the same $V_{\mathrm{cmax,c}}$ and g_m values were kept). To determine how $J_{\mathrm{max,i}}$ changes with $J_{\mathrm{max,c}}$ for a given g_m, or with g_m for a given $J_{\mathrm{max,c}}$, $J_{\mathrm{max,c}}$ and g_m were varied in prescribed intervals with nested loops while $V_{\mathrm{cmax,c}}$ and $T_{\mathrm{u,c}}$ were varied randomly. If the randomly generated values of $V_{\mathrm{cmax,c}}$ and $T_{\mathrm{u,c}}$ did not satisfy the inequality in Equation 2.1 or if the minimum number requirements were not met, these values were discarded and new values of $V_{\mathrm{cmax,c}}$ and $T_{\mathrm{u,c}}$ were randomly generated (but the same $J_{\mathrm{max,c}}$ and g_m values were kept). A similar scheme was used to generate A/C_i curves for determining how $T_{\mathrm{u,i}}$ changes with $T_{\mathrm{u,c}}$ for a given g_m, or with g_m for a given $T_{\mathrm{u,c}}$. An additional 5000 A/C_i curves were simulated by varying all parameters randomly to increase the variability of parameter values of the simulated A/C_i curves for parameter relationship analyses. During all these simulations, light was set at 1000 μmol/m^2/s (a typical value in A/C_i curve measurements), R_d at $0.015 \times V_{\mathrm{cmax,c}}$

(e.g., Bonan et al. 2011; Niinemets et al. 1998) and leaf temperature at 25°C. The Rubisco kinetic constants and the CO_2 compensation point were fixed for all simulated A/C_i curves at the values given in Table 1 of Sharkey et al. (2007).

2.3.3. A/C_i Curve Fitting

The measured and simulated A/C_i curves were analyzed with the approach of Gu et al. (2010) which is the same as that used in LeafWeb. In Gu et al.'s (2010) approach, each point of a given A/C_i curve can be in either Rubisco-, RuBP regeneration-, or TPU-limited states. The fitting procedures start by enumerating all possible combinations of limitation states occupied by the points of the curve. This strategy avoids the need to arbitrarily assign transitional thresholds for limitation states. The total number of possible combinations is reduced if one considers that instead of occurring in a random sequence, the three limitation states must follow certain pattern along the C_i (C_c) axis in order to be consistent with the FvCB model, i.e. the C_i (C_c) values for the Rubisco-limited state should be smaller than those of the RuBP regeneration-limited state, which in turn should be smaller than for the TPU-limited points. Each combination is then fit separately with the limitation state of each point fixed to ensure a smooth cost function for the change-point FvCB model. During this process, the so-called inadmissible fits are detected and corrected via a penalization strategy. Inadmissible fits are those which have such ‘optimally’ estimated parameters that the limitation states of points of the curve calculated with them do not agree with the limitation state distribution originally assigned to the combination. The disagreement arises because the FvCB model is a change-point model. Inadmissible fits should also occur in traditionally used A/C_i curve fitting methods, but had not been reported in the literature until Gu et al. (2010). Once all possible combinations of the limitation states are fitted, the combination that yields the smallest residual least square is selected. Gu et al. (2010) demonstrated that this approach can retrieve the A/C_c-based parameters used in simulating A/C_i curves while other approaches may fail.

The reliability of estimates of parameters ultimately depends on the quality of A/C_i curve measurements. Gu et al. (2010) made specific suggestions on how to make leaf gas exchange measurements that are informative for parameter estimation. They also suggested that the first and second derivatives of the cost function with respect to a parameter of interest should be used to identify fittings that have not been adequately constrained by measurements (inadequately constrained fittings have non-zero first or near-zero second derivatives). This additional step is necessary because the FvCB model can be fitted to the measurements with perfect precision, despite producing estimated values of the parameters that are not biologically meaningful. This can happen when one tries to estimate too many parameters or when the A/C_i relationships lack adequate numbers of data points in the curvature section. Details about how to identify inadequate fittings and over-fittings are described by Gu et al. (2010).

The fitting procedures described above are applied twice for each curve. In the first fitting, g_m is assumed infinite and the A/C_i -based parameters are estimated; in the second fitting, g_m is estimated together with other A/C_c -based parameters. The kinetic constants and coefficients in the temperature response functions, which are taken from Table 1 of Sharkey et al. (2007), are kept the same for all fittings. Parameters are standardized to a reference temperature of 25^{o}C.

2.4. RESULTS

2.4.1. Results Based on Actual Leaf Gas Exchange Measurements

Figures 2.1-2.3 present results on parameters inferred from measured A/C_i curves. Figure 2.1 shows the ratios of the estimated A/C_i-based to A/C_c-based parameters as a function of mesophyll conductance. The A/C_i -based parameters are smaller than the A/C_c-based values, indicating that omission of g_m leads to underestimation of true parameters. The degree of underestimation depends on the magnitude of g_m and can be up to 75, 60, and 40% for V_{cmax}, J_{max}, and T_u, respectively. As mesophyll conductance increases, the two sets of parameters tend to converge. This consequence is expected because the A/C_i-based estimation assumes an infinite mesophyll conductance. It also appears that $V_{cmax,i}$ (Figure 2.1a) is the most sensitive parameter to the variation of mesophyll conductance, while $J_{max,i}$ (Figure 2.1b) and $T_{u,i}$ (Figure 2.1c) have the intermediate and lowest sensitivity, respectively.

Due to variable parameter sensitivities to mesophyll conductance, the relationships among $V_{cmax,i}$, $J_{max,i}$ and $T_{u,i}$ differ from those among $V_{cmax,c}$, $J_{max,c}$ and $T_{u,c}$. Figure 2.2 shows these functional relationships obtained from A/C_i-based (Figure 2.2a, c, e) and from A/C_c-based estimations (Figure 2.2b, d, f). The ratios of $J_{max,i}$ to $V_{cmax,i}$ (1.6835), $T_{u,i}$ to $V_{cmax,i}$ (0.1246), and $T_{u,i}$ to $J_{max,i}$ (0.0744) are all larger than their counterparts from the A/C_c -based parameters ($J_{max,c}$ / $V_{cmax,c}$ = 1.1239, $T_{u,c}$ / $V_{cmax,c}$ = 0.0775, and $T_{u,c}$ / $J_{max,c}$ = 0.0697). Moreover, the relationships among the A/C_i-based parameters are tighter than those among the A/C_c-based parameters, as indicated by the corresponding R^2 values. These results are important as they suggest that the actual coupling among the key parameters V_{cmax}, J_{max}, and T_u of the photosynthetic machineries, which has been exploited widely both in experimental and modeling studies, may not be as strong as previously thought.

Among the three photosynthetic parameters, the relationship between T_u and J_{max} is tighter than that between J_{max} and V_{cmax}, which in turn is tighter than that between T_u and V_{cmax}. The same order of goodness-of-fit relationship is preserved regardless whether g_m is assumed infinite (Figure 2.2a, c, e) or estimated explicitly (Figure 2.2b, d, f).

Figures 2.1-2.2 indicate that a simple linear function is not adequate to convert the A/C_i-based parameters to the corresponding A/C_c-based values, confirming the suggestion by Niinemets et al. (2009b). To achieve more accurate conversion, we used a nonlinear model with both the A/C_i-based parameter and g_m as inputs:

$$y = x\exp\left(a\frac{x^c}{g_m^b + d}\right). \tag{2.2}$$

In the above equation, (x, y) represents the pairs of $(V_{cmax,i}, V_{cmax,c})$, $(J_{max,i}, J_{max,c})$, and $(T_{u,i}, T_{u,c})$ and a, b, c, and d are empirical constants that differ among these pairs. The values of a, b, c, and d are given in Table 2.2.

Figure 2.3 demonstrates that this nonlinear function performs well in quantifying the relationships between the apparent and corresponding true parameters. The performance benefits from an inherent feature of Equation 2.2 with respect to the effect of g_m: when g_m is infinitely large, the A/C_i–based parameters converge to the A/C_c-based parameters ($x = y$); when g_m decreases and thus the diffusion of CO_2 inside the leaf is retarded by greater resistance, the ratio of y/x increases, indicating the A/C_i –based parameters (x) increasingly underestimate the A/C_c –based parameters (y). In the following section, we demonstrate that these findings still hold for parameters obtained from simulated A/C_i curves.

2.4.2. Results Based on Simulated A/C_i Curves

Figure 2.4-2.6 show results obtained from simulated A/C_i curves. Figure 2.4 examines the apparent, A/C_i-based parameters as functions of mesophyll conductance for multiple fixed values of the true parameters (Figure 2.4a, c, e); also shown are the ratios of A/C_i-based parameters to true parameters (Figure 2.4b, d, f). In Figure 2.4, mesophyll conductance is shown up to 2 μmol m^{-2} $s^{-1}Pa^{-1}$ because this is the range with which most sensitive variations occur. The analysis of simulated A/C_i curves again shows that the apparent, A/C_i-based parameters generally underestimate the corresponding true values and the underestimation is more pronounced at lower g_m values. These findings are consistent with results from measured A/Ci curves (comparing Figure 2.4b, d, f with Figure 2.1a, b, c). The simulated A/C_i curves provide several additional patterns that are difficult to obtain with measured A/C_i curves. First, for a given value of true parameter $V_\mathrm{cmax,c}$, the A/C_i-based $V_\mathrm{cmax,i}$ initially increases with g_m and asymptotically approaches its true value as g_m increases (Figure 2.4a). Second, the covariation of $V_\mathrm{cmax,i}$ and g_m (the slope of the $V_\mathrm{cmax,i} - g_m$ curve for a given $V_\mathrm{cmax,c}$) is steeper at lower g_m values but becomes flat as g_m increases (Figure 2.4a). Third, the magnitude of the true parameter $V_\mathrm{cmax,c}$ affects the relationship between g_m and the apparent, A/C_i-based $V_\mathrm{cmax,i}$, with a larger $V_\mathrm{cmax,c}$ resulting in a greater deviation of $V_\mathrm{cmax,i} / V_\mathrm{cmax,c}$ ratio from unity (Figure 2.4b), suggesting that the assumption of an infinite g_m disproportionately biases the estimation of plants with high photosynthetic capacities.

Similar characteristics are found for the apparent parameters $J_\mathrm{max,i}$ and $T_\mathrm{u,i}$, but again, with reduced sensitivities (Figure 2.4c-f). Note the missing points in Figure 2.4c-f at low g_m values. Without explicit consideration of g_m, A/C_i curve analyses would not be able to properly identify the three limitation states in a set of points. When g_m values are quite small, even the very presence of RuBP regeneration and TPU limitation states in the dataset may not be identified, explaining the missing points in Figure 2.4c-f.

Figure 2.5 emphasizes different aspects from Figure 2.4. It shows the apparent, A/C_i-based parameters as functions of corresponding true A/C_c-based parameters for multiple fixed g_m values (Figure 2.5a, c, e). The ratios between the two sets of corresponding parameters are also displayed (Figure 2.5b, d, f). The underestimated $V_{\mathrm{cmax,i}}$ increasingly deviates from $V_{\mathrm{cmax,c}}$ as $V_{\mathrm{cmax,c}}$ increases and as g_m decreases (Figure 2.5a). The ratio of $V_{\mathrm{cmax,i}}$ to $V_{\mathrm{cmax,c}}$ decreases with $V_{\mathrm{cmax,c}}$, with a faster rate at low $V_{\mathrm{cmax,c}}$ and g_m values than at high $V_{\mathrm{cmax,c}}$ and g_m values (Figure 5b). Again, Figure 2.5 demonstrates that the effects of mesophyll conductance on $J_{\mathrm{max,i}}$ and $T_{\mathrm{u,i}}$ are broadly similar to those on $V_{\mathrm{cmax,i}}$ but with reduced sensitivities (Figures 5c-f). The decreasing sensitivity to mesophyll conductance from $V_{\mathrm{cmax,i}}$ to $J_{\mathrm{max,i}}$ to $T_{\mathrm{u,i}}$ is revealed by an increasingly tighter linear relationship between the apparent and true parameters (from Figure 5a to c to e) and by having ratios increasingly close to unity (from Figure 5b to d to e).

Consistent with patterns shown in Figure 2.2 from measured A/C_{i} curves, Figure 2.6 demonstrates that the relationships among V_{cmax}, J_{max} and T_{u} are altered in the absence of explicit consideration of g_m. The relationships among $V_{\mathrm{cmax,i}}$, $J_{\mathrm{max,i}}$ and $T_{\mathrm{u,i}}$ are tighter than those among $V_{\mathrm{cmax,c}}$, $J_{\mathrm{max,c}}$ and $T_{\mathrm{u,c}}$. The higher goodness-of-fit is essentially an artifact, a consequence of the decreased freedom of variation in the estimated $V_{\mathrm{cmax,i}}$, $J_{\mathrm{max,i}}$ and $T_{\mathrm{u,i}}$ when a finite g_m is assumed to be infinitely large. The ratio of $J_{\mathrm{max,i}}$ to $V_{\mathrm{cmax,i}}$ (1.69), is larger than the ratio of $J_{\mathrm{max,c}}$ to $V_{\mathrm{cmax,c}}$ (1.30). Similarly, the ratios of $T_{\mathrm{u,i}}$ to $V_{\mathrm{cmax,i}}$ (0.11, Figure 2.6c) and to $J_{\mathrm{max,i}}$ (0.07, Figure 2.6e) are larger than the corresponding ratios of $T_{\mathrm{u,c}}$ to $V_{\mathrm{cmax,c}}$ (0.08, Figure 2.6d) and to $J_{\mathrm{max,c}}$ (0.06, Figure 2.6e). The decreases in these ratios from the A/C_i-based parameters to the A/C_c-based parameters are a result of reduced underestimation and sensitivity to mesophyll conductance from $V_{\mathrm{cmax,i}}$ to $J_{\mathrm{max,i}}$ to $T_{\mathrm{u,i}}$. These ratios are very close to their counterparts obtained with measured A/C_{i} curves (comparing the corresponding slope values listed in Figure 2.2 and 2.6).

Also consistent with results based on measured A/C_i curves is the order of goodness-of-fit of the relationships among V_cmax, J_max, and T_u. T_u is more tightly related to J_max than to V_cmax while the goodness-of-fit between V_cmax and J_max lies between that of T_u and J_max and that of T_u and V_cmax. Whether g_m is assumed infinite (Figure 2.6a, c, e) or estimated (Figure 2.6b, d, f) does not affect this order.

2.5. DISCUSSION

To the best of our knowledge, this study is the first worldwide effort to demonstrate and quantify the differential efforts of g_m on key photosynthetic parameters and their relationships estimated from leaf gas exchange measurements. Our finding has implications for both modeling and process-based studies. Large-scale carbon cycle models often rely on the relationships among V_cmax, J_max, and T_u for parameterizations and for establishing the impact of nutrient availability on photosynthesis (Kattge et al. 2009; Bonan et al. 2011). These relationships have been also used as measures of balance among different limiting processes of the photosynthetic machineries in evaluating the response of leaf photosynthesis to changes in CO_2 concentration, temperature, and nutrient conditions (Hikosaka 2005; Onoda et al. 2005a,b). Our finding suggests that current parameterizations of photosynthetic processes in carbon cycle models may need to be re-evaluated and mesophyll conductance may complicate the interpretation of photosynthetic parameter relationships in the context of the operation of photosynthetic machineries.

In addition, our study, for the first time, provides direct avenues for improving the realism of photosynthesis representation in large-scale carbon cycle models by quantifying the role of g_m in shaping key model parameters and regulating photosynthesis. Current global carbon cycle models rely on C_i and employ photosynthetic parameters estimated under the assumption of an infinite g_m. These models ignore the drawdown of CO_2 partial pressures from the substomatal cavity to chloroplast and therefore overestimate the CO_2 concentrations at which the photosynthetic machineries are actually operating in the current atmosphere. Consequently it may be difficult for them to adequately simulate the responsiveness of terrestrial carbon cycles to rising atmospheric CO_2 concentrations. Our conversion function Equation 2.2 could be applied to transform the apparent, A/C_i -based parameters to their corresponding true values for use in mesophyll conductance - represented global carbon cycle models.

However, using a single parameter mesophyll conductance to characterize the diffusion and transport of CO_2 inside leaves has its limitations (Tholen and Zhu 2011; Tholen et al. 2012). It simplifies the three-dimensional mesophyll architecture to one big cell in which one big chloroplast resides. Furthermore, it assumes that the resistance to diffusion caused by the chloroplast envelope and stroma is much smaller than that by cell walls and plasmalemma. Tholen et al. (2012) showed when the resistance arising from chloroplast envelope is not significantly smaller than that from cell walls and plasmalemma, g_m does not entirely reflect diffusion properties of the mesophyll; it also depends on the ratio of the respiratory rate (photorespiration + day respiration) to the net photosynthetic rate, resulting in a correlation with stomatal conductance. In addition, there is evidence that aquaporin proteins and carbonic anhydrase may be involved in CO_2 transport (Flexas et al. 2008; Bernacchi et al. 2002). If so, CO_2 movement inside leaves may not be a purely passive diffusion process, which in turn may complicate the direct application of the conductance or resistance concept. Analysis of measured A/C_i curves can potentially be influenced by these complications. They apparently do not fundamentally alter the patterns and relationships reported in this study because the results based on the analysis of measured A/C_i curves are corroborated by those from the analysis of simulated A/C_i curves. However, individual values of particular parameters can be affected and therefore their interpretation requires caution.

The g_m values estimated from our measured A/C_i curves were overwhelmingly within the range of 0.1 to 10 μmol $\mathrm{m^{-2}\,s^{-1}\,Pa^{-1}}$. However, the entire range of variation in estimated g_m covers several orders of magnitude (Figure 2.1). How can such large variations in g_m be explained? How does leaf structure regulate the magnitude of g_m? We don't have enough information to answer these two questions with certainty. But it is possible that the large variations are caused by simplifying assumptions of A/C_i curve analysis as discussed above. More complicated models and parameters could be introduced to relax these assumptions (Tholen et al. 2012; Tholen and Zhu 2011). However, their application may be limited by the fact that the FvCB model is already over-parameterized with respect to typical leaf gas exchange measurements (Gu et al. 2010). It is also possible that measurement uncertainties and lack of constraining power in A/C_i curves can cause outliers in estimated g_m. The measurement procedures discussed by Gu et al. (2010) can be adopted to produce more informative A/C_i curves for the purpose of parameter estimation.

Regardless of the origin of extreme g_m values, there is a need to develop methods to directly measure g_m. Like the isotopic approach (Evans et al. 1986) and the chlorophyll fluorescence approach (Harley et al. 1992), the parameter fitting approach used in this study is an indirect way of inferring g_m. All these approaches require certain assumptions and thus potentially introduce uncertainties that are difficult to quantify. Research and technology development in this direction is needed to advance this important field (Sharkey 2012). Nevertheless it is reassuring that the results from measured and simulated A/C_i curves are consistent with each other, suggesting that any imperfection in the estimation of g_m likely does not qualitatively affect the findings reported here.

2.6. CONCLUSIONS

Using worldwide measurements across all major plant functional types and climates and massive model simulations, we demonstrated that mesophyll conductance differentially affects fundamental photosynthetic parameters and their relationships estimated from leaf gas exchange measurements. The widely adopted assumption of infinite mesophyll conductance leads to underestimation of the maximum carboxylation rate V_{cmax} (up to 75%), the maximum electron transport rate $J_{\max}$ (up to 60%) and the triose phosphate utilization rate T_{u} (up to 40%). The degree of underestimation is more pronounced at lower than at higher mesophyll conductance and when leaves have higher photosynthetic capacities (i.e., larger V_{cmax}, $J_{\max}$, and T_{u}). V_{cmax} is the most sensitive parameter to the variation of mesophyll conductance, T_{u} the least and $J_{\max}$ the intermediate. The assumption of infinite mesophyll conductance leads to overestimation of the ratios of $J_{\max}$ to V_{cmax}, T_{u} to V_{cmax}, and T_{u} to $J_{\max}$. It also results in artificially strong relationships among these parameters, a consequence of reduced freedom of variations of estimation. We also found that regardless whether mesophyll conductance is assumed infinite or estimated explicitly, the relationship between T_{u} and $J_{\max}$ is tighter than that between $J_{\max}$ and V_{cmax}, which in turn is tighter than that between T_{u} and V_{cmax}. Finally we showed that a nonlinear function can be used to convert the parameters estimated under the assumption of infinite mesophyll conductance to proper values if an estimated mesophyll conductance is available. This function can facilitate the development of mesophyll conductance representation in global carbon cycle models.

Leaf gas exchange measurements provide the basic information for understanding *in situ* photosynthetic processes and for parameterizing terrestrial carbon cycle models from local to regional to global scales. Proper interpretation of such measurements requires careful consideration of mesophyll conductance. We strongly recommend that future analyses of leaf gas exchange measurements include estimates of mesophyll conductance.

Finally we believe that there is a need for world-wide collaboration among researchers who routinely conduct leaf gas exchange measurements. Fundamental photosynthetic parameters are dynamic in space and time. Individual leaf-scale measurements rarely provide deep insights if they are not examined in proper spatial and temporal contexts. As demonstrated in the present study, collaboration among researchers world-wide is an effective and efficient way for providing such contexts and for individual leaf-scale measurements to make bigger contributions to advancing the field than otherwise possible. Furthermore, while leaf gas exchange measurements are frequently conducted by plant scientists world-wide, such measurements are rarely made available to modelers to improve their models. Open tools like LeafWeb (http://leafweb.ornl.gov/) can facilitate the collaboration among plant physiologists and ecologists and make easier the dialogue between experimental and modeling communities.

2.7. ACKNOWLEDGEMENTS

This study was carried out at multiple institutions. The support for research at UT – Austin came from Department of Energy (DE-FG02-01ER63198). The support for research at ORNL came from U.S. Department of Energy, Office of Science, Biological and Environmental Research Program, Climate and Environmental Sciences Division. The ORNL's LDRD program also partially supported the research. ORNL is managed by UT-Battelle, LLC, for the U.S. Department of Energy under contract DE-AC05-00OR22725. U.S. Department of Energy support for the University of Missouri (Grant DE-FG02-03ER63683) is gratefully acknowledged.

Table 2.1. List of species whose A/C_i curves are used in the study.

Species	Location
Abies lasiocarpa	Colorado, USA
Acalypha diversifolia	Gamboa, Republic of Panama
Acer rubrum	Michigan, USA
Acer saccharum	Missouri, USA
Achillea millefolium	North Dakota, USA
Adenostoma fasciculatum	California, USA
Agropyron repens	North Dakota, USA
Alchornea costaricensis	Gamboa, Republic of Panama
Ambrosia psilostachya	North Dakota, USA
Annona muricata	Viçosa, Brazil
Antennaria neglecta	North Dakota, USA
Arabidopsis thaliana	Tennessee, USA
Arctostaphylos patula	Oregon, USA
Artemisia absinthium	North Dakota, USA
Artemisia frigida	North Dakota, USA
Artemisia ludoviciana	North Dakota, USA
Artocarpus heterophyllus	Viçosa, Brazil
Astronium graveolens	Gamboa, Republic of Panama
Averrhoa carambola	Viçosa, Brazil
Betula papyrifera	Michigan, USA
Bixa orellana	Gamboa, Republic of Panama
Bromus inermis	North Dakota, USA
Calathea lutea	Gamboa, Republic of Panama
Calophyllum brasiliense	Gamboa, Republic of Panama
Calophyllum inophyllum	Gamboa & Balboa, Ancon, Republic of Panama
Carex heliophila	North Dakota, USA
Cariniana sp.	Viçosa, Brazil
Carya ovata	Missouri, USA
Casearia commersoniana	Gamboa, Republic of Panama
Cecropia peltata	Gamboa, Republic of Panama
Chrysophyllum cainito	Viçosa, Brazil
Cinnamomum zeylanicum	Viçosa, Brazil
Cinnamomum triplinerve	Gamboa, Republic of Panama
Cirsium arvense	North Dakota, USA
Cirsium flodmanii	North Dakota, USA

Citharexylum caudatum	Balboa, Ancon, Republic of Panama
Citrus sp.	Viçosa, Brazil
Clusia croatii	Gamboa, Republic of Panama
Clusia peninsulae	Gamboa, Republic of Panama
Clusia pratensis	Gamboa, Republic of Panama
Cochlospermum vitifolium	Gamboa, Republic of Panama
Coffea Arabica	Viçosa, Brazil
Crescentia cujete	Balboa, Ancon, Republic of Panama
Cupania scrobiculata	Gamboa, Republic of Panama
Dalbergia retusa	Gamboa, Republic of Panama
Doliocarpus dentatus	Gamboa, Republic of Panama
Doliocarpus olivaceus	Gamboa & Balboa, Ancon, Republic of Panama
Eucalyptus sp.	Southeastern Brazil
Eriobotrya japonica	Viçosa, Brazil
Eugenia uniflora	Viçosa, Brazil
Genipa Americana	Viçosa, Brazil
Geum triflorum	North Dakota, USA
Glycine max	Tennessee, USA
Helianthus pauciflorus	North Dakota, USA
Hieronyma alchorneoides	Gamboa, Republic of Panama
Hybanthus prunifolius	Gamboa, Republic of Panama
Hymenaea courbaril	Viçosa, Brazil
Inga spectabilis	Gamboa, Republic of Panama
Inga sp.	Viçosa, Brazil
Jatropha curcas	Gamboa, Republic of Panama
Juniperus virginiana	Missouri, USA
Litchi chinensis	Viçosa, Brazil
Luehea seemannii	Gamboa, Republic of Panama
Malpighia emarginata	Viçosa, Brazil
Manilkara zapota	Gamboa, Republic of Panama
Melilotus officinalis	North Dakota, USA
Merremia sp.	Gamboa, Republic of Panama
Miconia impetiolaris	Gamboa, Republic of Panama
Myroxylon balsamum	Gamboa, Republic of Panama
Nassella viridula	North Dakota, USA
Ochroma pyramidale	Gamboa, Republic of Panama
Oligoneuron rigidum	North Dakota, USA

Omphalea diandra	Balboa, Ancon, Republic of Panama
Ormosia macrocalyx	Gamboa, Republic of Panama
Oryza sativa	Viçosa, Brazil
Oxalis stricta	North Dakota, USA
Pascopyrum smithii	North Dakota, USA
Passiflora vitifolia	Gamboa, Republic of Panama
Peltogyne purpurea	Gamboa, Republic of Panama
Persea Americana	Viçosa, Brazil
Philodendron sp.	Gamboa, Republic of Panama
Phyllostachys humilis	Dublin, Ireland
Picea engelmannii	Colorado, USA
Picea mariana	Minnesota, USA
Pinus contorta	Colorado, USA
Pinus pinaster	Aquitaine, France
Pinus ponderosa	Oregon, USA
Pinus taeda	North Carolina, USA
Piper reticulatum	Gamboa, Republic of Panama
Piper sp.	Gamboa, Republic of Panama
Pithecellobium mangense	Balboa, Ancon, Republic of Panama
Platymiscium pinnatum	Gamboa, Republic of Panama
Poa pratensis	North Dakota, USA
Populus grandidentata	Michigan, USA
Populus deltoids	Tennessee, USA
Psidium guajava	Viçosa, Brazil
Purshia tridentate	Oregon, USA
Quercus alba	Missouri & Tennessee, USA
Quercus stellata	Missouri & Tennessee, USA
Quercus velutina	Missouri, USA
Quercus rubra	Michigan & Tennessee, USA
Rhapis excelsa	Balboa, Ancon, Republic of Panama
Rosa arkansana	North Dakota, USA
Schefflera sp.	Balboa, Ancon, Republic of Panama
Schima superba	Zhejiang, China
Schinus terebinthifolius	Viçosa, Brazil
Serjania sp.	Gamboa, Republic of Panama
Solidago Canadensis	North Dakota, USA
Solidago missouriensis	North Dakota, USA

Spondias mombin	Gamboa, Republic of Panama
Sterculia apetala	Gamboa, Republic of Panama
Stigmaphyllum sp.	Gamboa, Republic of Panama
Swietenia macrophylla	Viçosa, Brazil & Balboa, Ancon, Republic of Panama
Symphyotrichum ericoides	North Dakota, USA
Symphoricarpos occidentalis	North Dakota, USA
Syzygium jambos	Viçosa, Brazil
Tabebuia rosea	Gamboa & Balboa, Ancon, Republic of Panama
Taraxacum officinale	North Dakota, USA
Tectona grandis	Viçosa, Brazil
Trifolium ambiguum	Minnesota, USA
Veitchia merrillii	Balboa, Ancon, Republic of Panama
Vismia bilbergiana	Gamboa, Republic of Panama
Vitex cooperi	Gamboa, Republic of Panama
Zuelania Guidonia	Gamboa, Republic of Panama

Table 2.2. The values of empirical constants for the conversion function[*] that relates the A/C_i to A/C_c- based parameters.

	a	*b*	*c*	*d*	R^2	RMS[†] (μmol $\mathrm{m^{-2}\,s^{-1}}$)
$V_{\mathrm{cmax,c}}$	0.1190	1.2656	0.6394	0.9610	0.83	18.0749
$J_{\mathrm{max,c}}$	0.00851	0.7530	0.6201	-0.1173	0.97	7.5235
$T_{\mathrm{u,c}}$	0.1280	1.8045	0.2472	1.6298	0.99	0.3606

[*] Refer to Equation 2.2.

[†] RMS represents root mean square error.

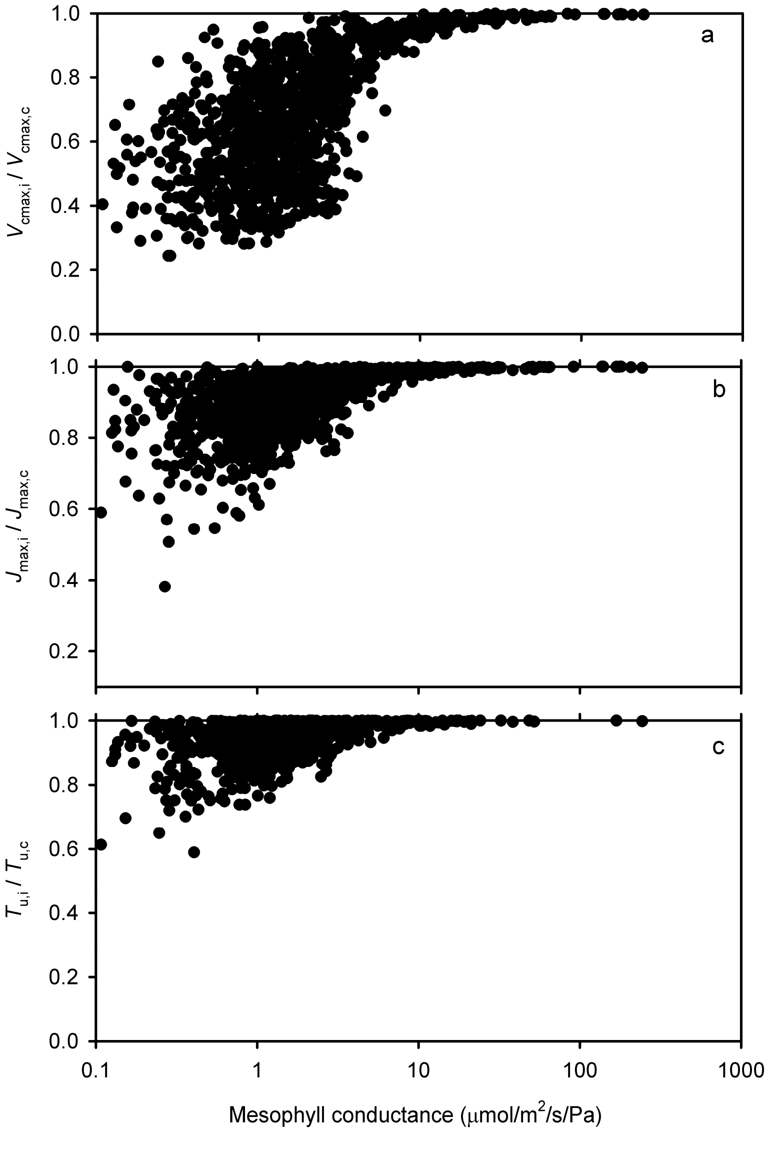

Figure 2.1. The ratios of the *A*/C_i-based to corresponding *A*/C_c-based parameters as a function of mesophyll conductance.

The *A*/C_i-based parameters are estimated by assuming infinite mesophyll conductance while the *A*/C_c-based parameters are estimated together with mesophyll conductance. Note that mesophyll conductance is in logarithmic scale. a: the ratio of *A*/C_i-based V_{cmax} ($V_{cmax,i}$) to *A*/C_c-based V_{cmax} ($V_{cmax,c}$); b: the ratio of *A*/C_i-based J_{max} ($J_{max,i}$) to *A*/C_c-based J_{max} ($J_{max,c}$); c: the ratio of *A*/C_i-based T_u ($T_{u,i}$) to *A*/C_c-based T_u ($T_{u,c}$). Results are based on measured *A*/C_i curves.

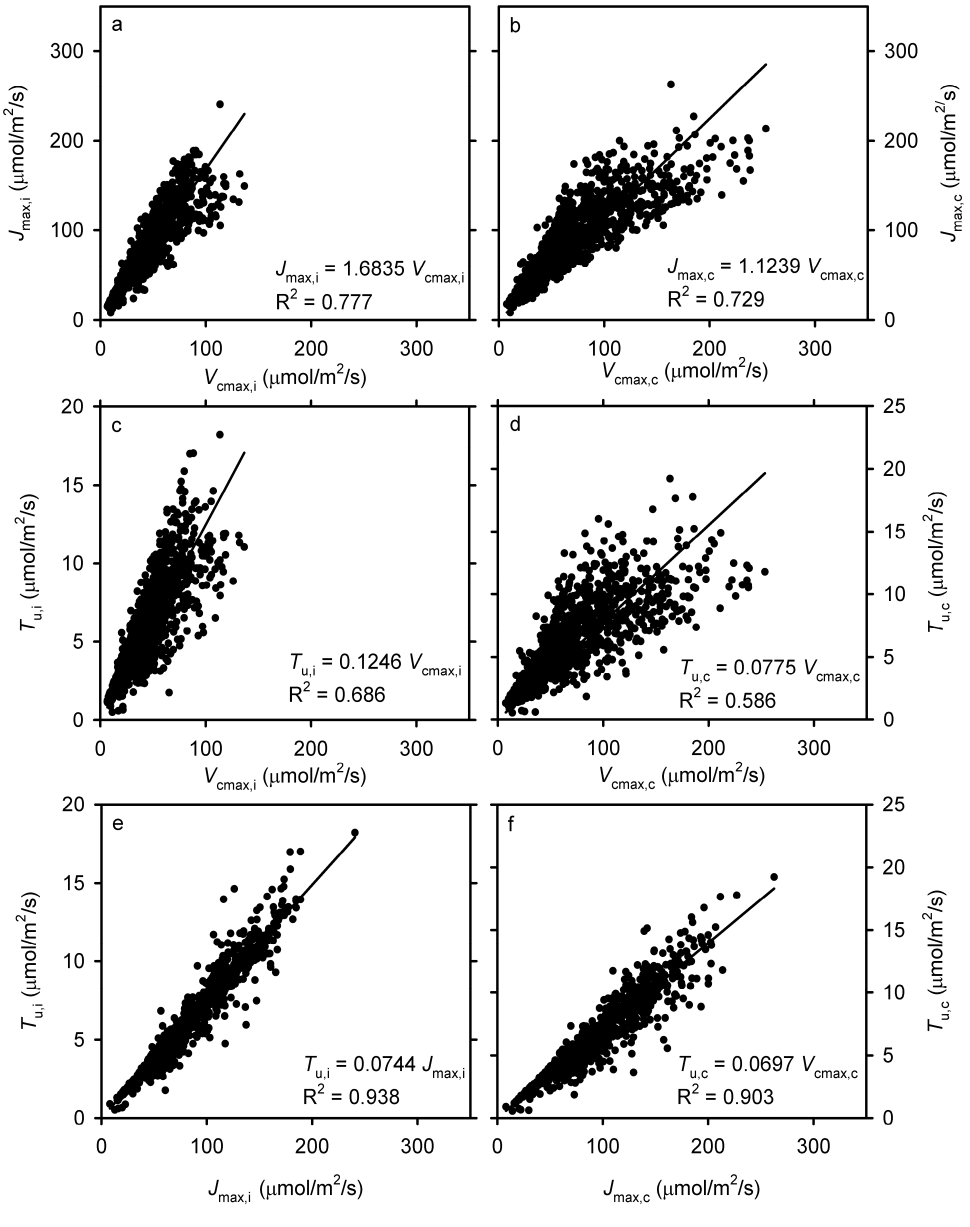

Figure 2.2. A comparison of the A/C_i-based parameter relationships with the A/C_c-based parameter relationships.

The A/C_i-based parameters are estimated by assuming infinite mesophyll conductance while the A/C_c-based parameters are estimated together with mesophyll conductance. a, c and e: the relationships among the A/C_i-based V_{cmax} ($V_{cmax,i}$), J_{max} ($J_{max,i}$) and T_u ($T_{u,i}$); b, d and f: the relationships among the A/C_c-based V_{cmax} ($V_{cmax,c}$), J_{max} ($J_{max,c}$) and T_u ($T_{u,c}$). Results are based on measured A/C_i curves.

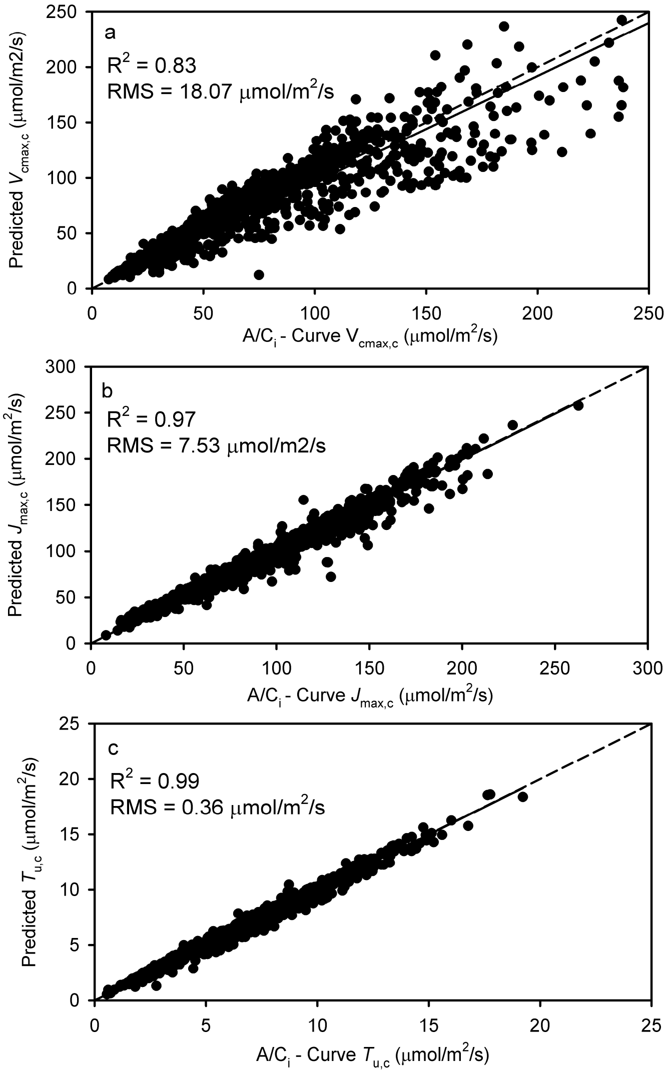

Figure 2.3. The goodness of fit for the conversion function[*], which calculates the A/C_c-based parameters from the A/C_i-based parameters and mesophyll conductance.

The A/C_i-based parameters are estimated by assuming infinite mesophyll conductance while the A/C_c-based parameters are estimated together with mesophyll conductance. The values calculated from the conversion function Equation 2.2 are in the y axis while the values estimated from curve fitting are in the x axis. Results are based on measured A/C_i curves.

---

[*] Refer to Equation 2.2.

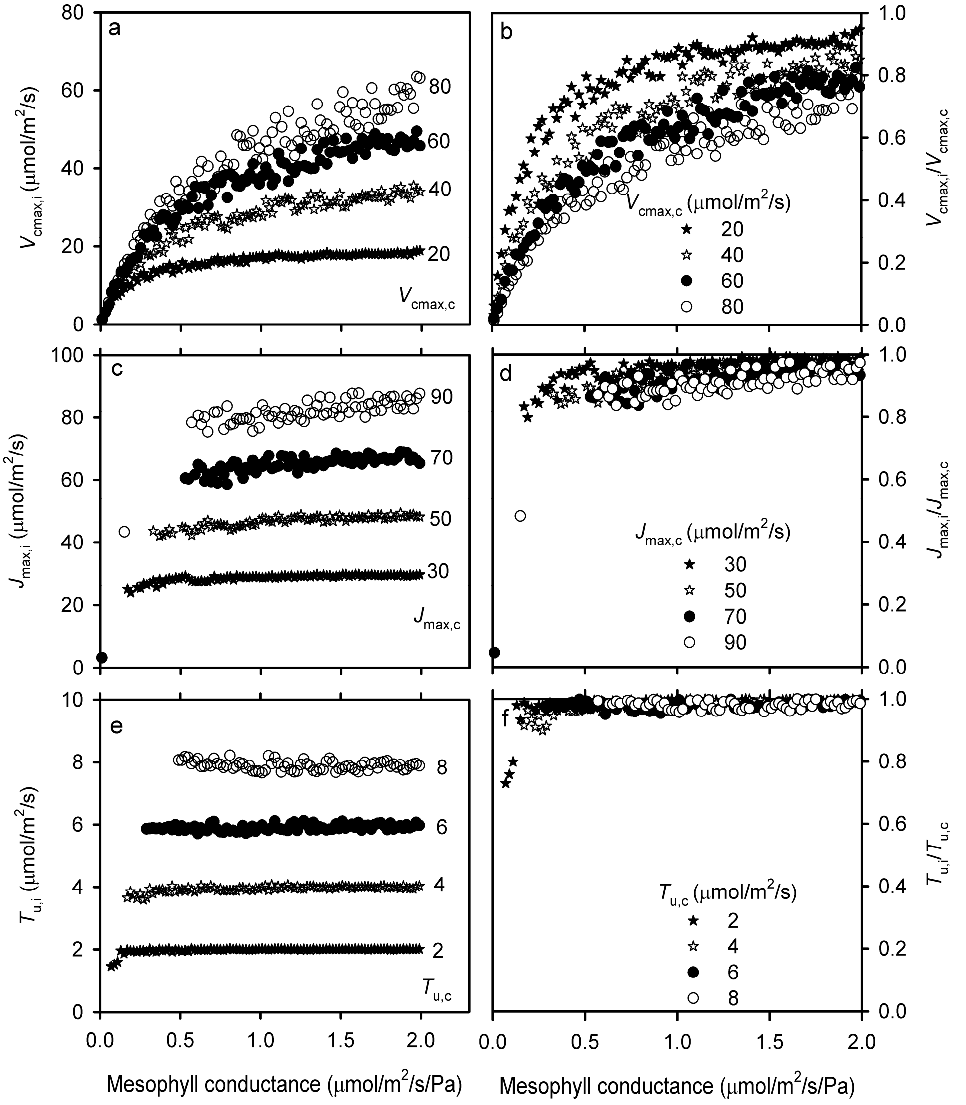

Figure 2.4. The relationships between the A/C_i-based parameters and mesophyll conductance for a given set of values of A/C_c-based parameters.

The A/C_i-based parameters are estimated by assuming infinite mesophyll conductance while the A/C_c-based parameters are estimated together with mesophyll conductance. a, c, and d: the A/C_i-based V_{cmax} ($V_{cmax,i}$), J_{max} ($J_{max,i}$) and T_u ($T_{u,i}$) as a function of mesophyll conductance for a given set of values of A/C_c-based V_{cmax} ($V_{cmax,c}$), J_{max} ($J_{max,c}$) and T_u ($T_{u,c}$), respectively; b, d, and f: the ratios of A/C_i-based to A/C_c-based parameters as a function of mesophyll conductance for a given set of values of A/C_c-based parameters. Results are based on simulated A/C_i curves.

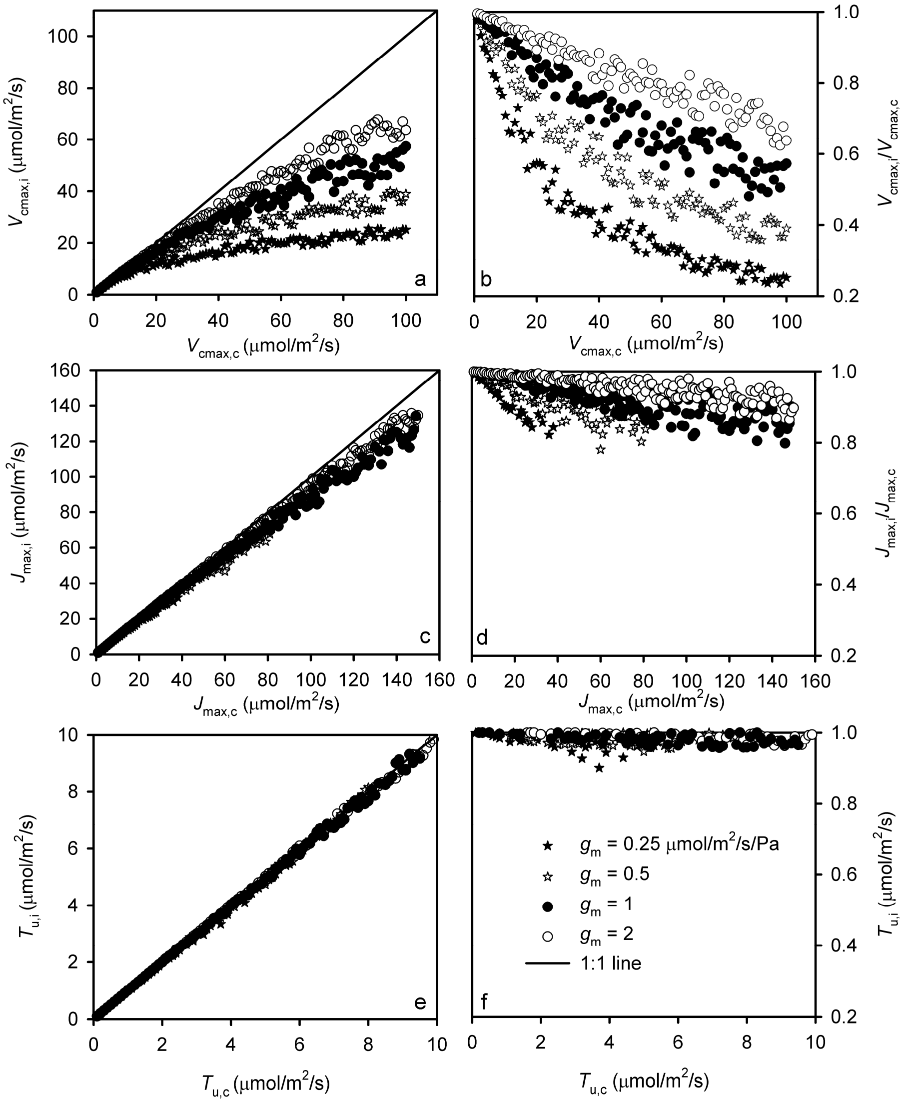

Figure 2.5. The relationships between the A/C_i-based and A/C_c-based parameters for a given set of values of mesophyll conductance.

The A/C_i-based parameters are estimated by assuming infinite mesophyll conductance while the A/C_c-based parameters are estimated together with mesophyll conductance. a, c, and d: the A/C_i-based V_{cmax} ($V_{\mathrm{cmax,i}}$), $J_{\max}$ ($J_{\mathrm{max,i}}$) and T_u ($T_{\mathrm{u,i}}$) as a function of A/C_c-based V_{cmax} ($V_{\mathrm{cmax,c}}$, a), $J_{\max}$ ($J_{\mathrm{max,c}}$, c) and T_u ($T_{\mathrm{u,c}}$, d), respectively, for a given set of values of mesophyll conductance; b, d, and f: the ratios of A/C_i-based to A/C_c-based parameters as a function of A/C_c-based parameters for a given set of values of mesophyll conductance. Results are based on simulated A/C_i curves.

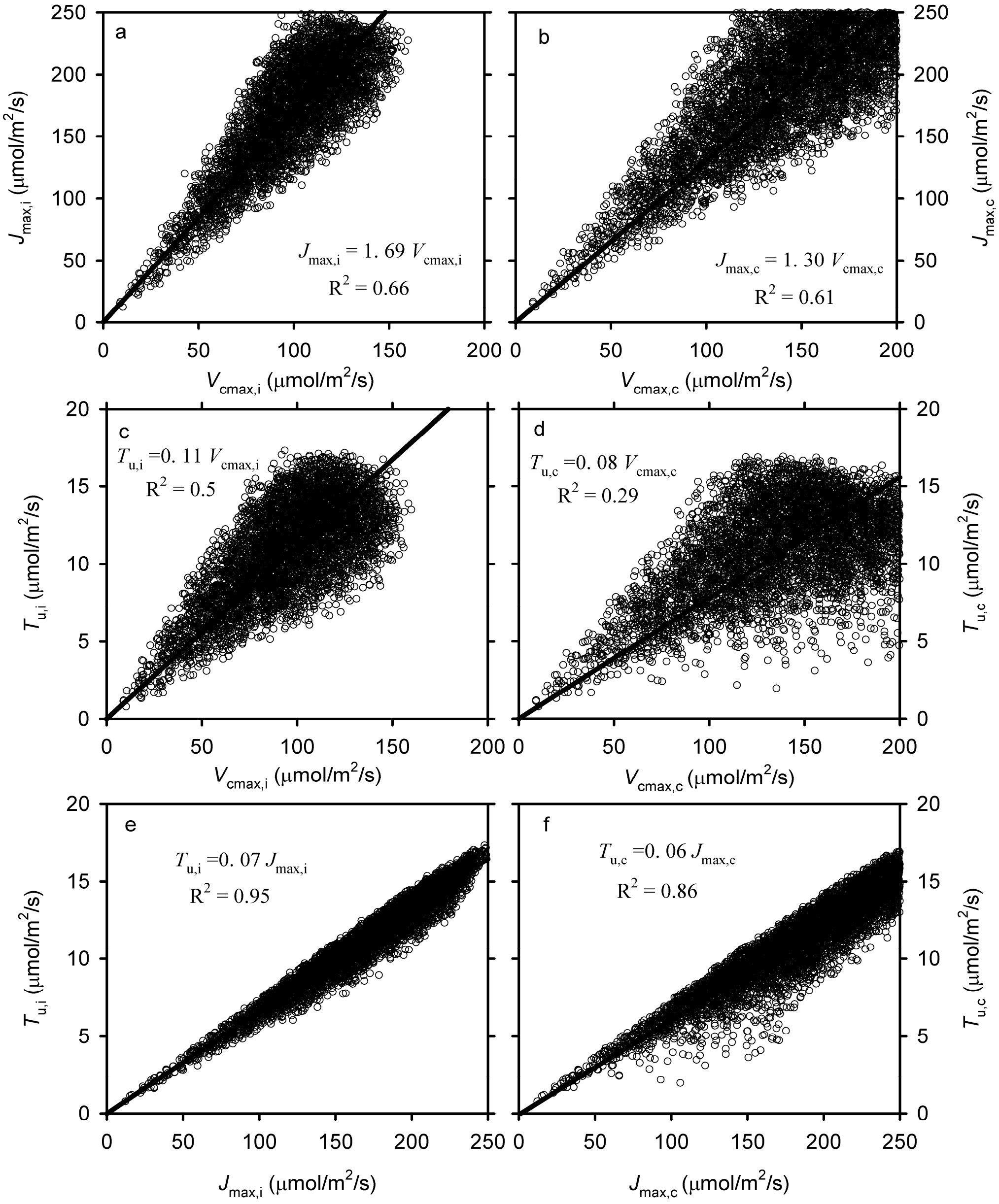

Figure 2.6. Same as Figure 2.2 but for simulated A/C_i curves.

Chapter 3: Representation of mesophyll diffusion of CO_2 in a climate model

3.1. ABSTRACT

Plant physiologists have long recognized that mesophyll conductance (g_m) strongly affects photosynthesis with an effect comparable to that of stomatal conductance. Yet, this term has been ignored in land surface models used for large-scale carbon and climate simulations. Here we present a simple but realistic parameterization of g_m based on the synthesis of new advances in plant physiological studies. In this formulation, g_m is calculated from its association with plant functional types and its dependence on environmental conditions. We implement this parameterization in the Community Land Model version 4a (CLM4a), a representative land component of climate models. We also recalibrate the key photosynthetic parameters V_{cmax}, J_{max}, and TPU to maintain the consistency between model structure and associated parameters. With the modified CLM4a, we investigate the impact of g_m on the global terrestrial gross primary production (GPP). Our simulations show that the inclusion of g_m slightly increases the estimated mean global annual GPP over the period of 1982-2004 by ~9 Pg C yr^{-1}. This increase in GPP is throughout the globe but particularly large in the tropics. We further found that omission of the mesophyll diffusion process can underestimate the potential of GPP stimulation to rising atmospheric CO_2. The trend of such discrepancy is about 27 Pg C y^{-1} per 1000 ppm, with the tropics playing the major role. This systematic trend is strongly influenced by climate variability. Our study suggests that it is crucial to represent g_m in modeling global terrestrial carbon cycles.

3.2. INTRODUCTION

Land surface models (LSMs) represent fundamental physical, chemical, and ecophysiological processes to study land-atmosphere interactions, ecosystem dynamics, and associated climate feedbacks (Sellers et al. 1997). Reliable predictions of future climate change as well as its impact on global carbon and hydrologic cycles require a realistic description of these processes in LSMs that are coupled to climate models. The current predictive capability of LSMs is hampered by large biases and uncertainties in their calculated carbon and water fluxes (Friedlingstein et al. 2006), a consequence of a number of model structural and parameter deficiencies (Bonan et al. 2011). To improve their realism and predictability, LSMs should be informed with new knowledge obtained from process-based experimental and observational studies.

Plant physiologists have long recognized that mesophyll conductance (g_m), also known as internal conductance, is an important limiting factor on photosynthesis comparable in effect to that of stomatal conductance (g_s) (e.g., Harley et al. 1992; Niinemets et al. 2009a; von Caemmerer and Evans 2010; Warren 2008; Flexas et al. 2008). Mesophyll conductance characterizes the process of CO_2 transfer from leaf intercellular air space through cell walls, membranes, cytosol to chloroplasts, the site of carboxylation. Hence, g_m and g_s jointly determine the actual CO_2 concentration available for carbon assimilation. Although g_s has otherwise been parameterized, g_m has yet to be accounted for in LSMs for carbon and climate simulations.

Without representation of the mesophyll diffusion process, LSMs implicitly assume an infinite value of g_m. This assumption is in gross contradiction to data reported in plant physiology literature. Measurements of hundreds of species around the world have consistently shown that g_m is finite and sufficiently small to result in a considerable drawdown of CO_2 from intercellular air space to chloroplasts (for a review, see Niinemets et al. 2009a). The g_m can cause a reduction of photosynthesis by up to 25% for crop species and up to 75% for natural vegetation (Terashima et al. 2006). Studies have also shown that this limitation on photosynthesis is more pronounced under water stress, with an effect comparable and additional to that of stomata and the maximum Rubisco carboxylation rate V_{cmax} (Keenan et al. 2010a,b; Egea et al. 2011). Niinemets et al. (2011) highlighted the role of g_m in predicting photosynthetic capacity under future CO_2 elevation. Therefore, direct physiological observations and concerns for future carbon projections argue for introducing g_m into large-scale LSMs.

A limited number of studies have attempted to represent g_m in canopy-level models. These studies assumed that g_m is either a fixed constant (Williams et al. 1996; Keenan et al. 2010a) or proportional to V_{cmax} (Le Roux et al. 2001) or to g_s (Cai et al. 2008). These treatments, although probably oversimplified (Flexas et al. 2008), have provided some insights into the effect of g_m on canopy photosynthesis at local scales. These local-scale modeling efforts have also lent support for representing g_m in large-scale carbon and climate models.

In this paper, we develop a simple but realistic parameterization to represent the g_m functioning in LSMs for climate simulations, building on the literature synthesis of advances in physiological studies and previous modeling efforts. It calculates g_m based on plant functional types (PFTs) and environmental variables. It attempts to be applicable broadly to different vegetation types, rather than to represent the behavior of particular ecosystems. We use the latest version of Community Land Model (CLM4a) (Bonan et al. 2011) as a representative land component of climate models to quantify the impact of g_m on land surface fluxes at the global scale with a focus on gross primary production (GPP). A legitimate concern for representing g_m in LSMs is that the current photosynthetic parameters in these models are estimated from leaf gas exchange measurements without explicit consideration of g_m (Gu et al. 2010; Ethier and Livingston 2004; Niinemets et al. 2009b). Bonan et al. (2011) and Chen et al. (2011) suggested that adjustment of V_{cmax} could compensate for model deficiencies in representing some key processes. To comply with the inclusion of g_m, we recalibrate key photosynthetic parameters in CLM4a, e.g., V_{cmax}, built on the quantitative findings in Chapter 2.

3.3. METHODS

3.3.1. The global mesophyll conductance model

Field measurements have shown that g_m varies with leaf structures and environmental conditions (Nobel 1977; Flexas et al. 2008; Warren 2008; Niinemets et al. 2009a). Leaf structures determine the maximum attainable g_m and external environmental forcings modify this maximum value. This consensus reflects a recent understanding that environmental stress factors (e.g., temperature and water) can induce rapid physiological changes (e.g. hardening of cell walls and aquaporin-mediated alteration of membrane permeability) that cause g_m to vary on time scales of minutes to hours (Chazen and Neumann 1994; Miyazawa et al. 2008). Accordingly, we model g_m as

$$g_m = g_{\max 0} \cdot f_l(x) \cdot f_T(T_l) \cdot f_w(\theta) \tag{3.1}$$

where $g_{\max 0}$ is the maximum g_m (i.e., that under non-stress conditions, here referring to the presence of ample soil water and a temperature of 25°C) of a leaf at the canopy top of a PFT; $f_l(x)$ represents the vertical variation of g_m as a function of cumulative leaf area index x from canopy top, driven by light gradient within the canopy; $f_T(T_l)$ and $f_w(\theta)$ are the response functions of g_m to leaf temperature T_l and to soil moisture θ, respectively. The present study makes no attempt to represent other environmental controls (e.g. salinity, O_3, nutrient availability, Flexas et al. 2008) on g_m because they are much less understood and seldom quantified in field studies.

The $g_{\max 0}$ varies significantly across plant species. A synthesis of measurements for ~100 plant species showed that this term is related to the leaf dry mass per unit area M_a through an empirical power law (Niinemets et al. 2009b)

$$g_{\max 0} = a \cdot M_{a0}^{\;b} \qquad (3.2)$$

where M_{a0} represents M_a at canopy top. The constants $a = 24.240338$ and $b = -0.6509$ (all parameter values are listed in Table 3.1) are two empirical parameters that have been determined by fitting the compiled data to Equation 3.2 ($R^2 = 0.79$, $P<0.001$, see Figure 2.1 in Niinemets et al. 2009b). Similar patterns were also reported by Flexas et al. (2008) and by Niinemets et al. (2009c) but with fewer species samples. Note the values of a and b depend on the units of data used for the nonlinear regression of Equation 3.2. Our study used μmol m^{-2} s^{-1} Pa^{-1} for $g_{\max0}$ and g_m, and g m^{-2} for M_{a0} and M_a. The coefficient b is negative, indicating $g_{\max0}$ decreases with M_{a0} across PFTs under non-stress conditions. The $g_{\max0}$ in Equation 3.2 is area-based while Niinemets et al. (2009b) used a mass-based unit. The area- and mass-based $g_{\max0}$ differ by a factor of M_{a0}. Accordingly, the value of b in our study is a notation on an area basis. In Equation 3.2, $g_{\max0}$ is represented as a leaf-trait associated with PFTs since it is determined by M_{a0}, which is the product of two important leaf-traits: leaf thickness and foliar mass density (Niinemets et al. 2009a).

Multiple steps are needed to derive an expression for $f_l(x)$, which describes the variation of g_m associated with the prevailing light regime within a plant canopy. The light intensity shapes mesophyll cell morphology, the number of mesophyll cell layers, and leaf thickness. These factors are components that determine $M_a(x)$, the leaf dry mass per area at cumulative leaf area index x (Niinemets 2007; Poorter et al. 2010). They also affect the total surface area of mesophyll cells exposed to intercellular air space per unit leaf area and hence g_m (Niinemets et al. 2009a; Nobel 2009). Consequently, g_m tends to change systematically from top to bottom of a canopy (Warren et al. 2007; Terashima et al. 2006; Hanba et al. 2002; Laisk et al. 2005; Han et al. 2010; Piel et al. 2002; Montpied et al. 2009) and scales well with $M_a(x)$ within canopy depth (Piel et al. 2002; Montpied et al. 2009). Therefore $M_a(x)$ is an important link between g_m and the prevailing light regime. Here the vertical variation of g_m is modeled

$$g_{\max}(x) = g_{\max 0} \cdot [M_a(x)/M_{a0}]^d \tag{3.3}$$

where $d = 0.8109$, an empirical parameter fitted from the data ($R^2 = 0.67$) in Montpied et al. (2009). Rearranging Equation 3.3, we have

$$f_I(x) = g_{\max}(x)/g_{\max 0} = [M_a(x)/M_{a0}]^d\ . \tag{3.4}$$

According to Niinemets (2007), $M_a(x)$ is related to the seasonally integrated photosynthetically active radiation $I(x)$ via

$$M_a(x) = M_{a0} \cdot [I(x)/I_0]^f \tag{3.5}$$

where I_0 is the value of $I(x)$ at canopy top; $f = 0.221897$, a parameter fitted ($R^2 = 0.57$) from Niinemets (2007). Applying the Beer's law,

$$I(x) = I_0 \cdot \exp(-k_I \cdot x) \tag{3.6}$$

where k_I = ~0.45, the seasonally averaged light extinction coefficient. Substituting Equation 3.6 and 3.5 to Equation 3.4, we obtain

$$f_I(x) = \exp(-k_I \cdot d \cdot f \cdot x) = \exp(-k_g \cdot x)\ . \tag{3.7}$$

Here, $k_g = k_I \cdot d \cdot f$ = 0.08971, a composite parameter derived from three empirical coefficients. Equation 3.7 shows that the vertical variation of g_m can be modeled as an exponentially decreasing function of cumulative leaf area index x from the top of canopy, characterized with a single decay coefficient k_g. The advantage of creating a single composite parameter k_g is that it facilitates the sensitivity testing with this parameter, which may guide process-based measurements. The joint control of M_{a0} and x on g_m is illustrated in Figure 3.1, showing that g_m decreases with larger M_{a0} and x, dominated by the PFT-specific M_{a0}.

It is important to clarify that the dependence of g_m on M_{a0} in Equation 3.2 is fundamentally different from the relationship between g_m and $M_a(x)$ in Equation 3.3 that is used to formulate $f_I(x)$. $M_a(x)$ is a composite leaf structural variable and is modified by prevailing light regimes within a plant canopy in ways that are fundamentally different from variations of the composite leaf trait M_{a0} across leaf forms of PFTs. As stated earlier, the light intensity affects $M_a(x)$ through its effects on mesophyll cell morphology, the number of mesophyll cell layers, and leaf thickness. In contrast, the variations of M_{a0} across leaf forms of PFTs reflect the changes in the compactness of mesophyll cells, the thickness of cell walls and foliar mass density. Detailed discussion on this issue is beyond the scope of this paper but can be found elsewhere (Niinemets et al. 2009a; Nobel 2009).

Several functions have been proposed to describe the temperature response of g_m (Bernacchi et al. 2002; Warren and Dreyer 2006; Yamori et al. 2006; Scafaro et al. 2011). Here the formulation of Bernacchi et al. (2002), which was based on detailed measurements, is used

$$f_T(T_l) = \exp[c - \Delta H_a/(R \cdot T_l)] / \{1 + \exp[(\Delta S \cdot T_l - \Delta H_d)/(R \cdot T_l)]\} \qquad (3.8)$$

where c = 20.0, a scaling constant; $\Delta H_a = 49.6\times10^3$ J mol^{-1}, the activation energy; $\Delta H_d = 437.4\times10^3$ J mol^{-1}, the deactivation energy; $\Delta S = 1.4\times10^3$ J mol^{-1} K^{-1}, an entropy term; and R = 8.314 J mol^{-1} K^{-1}, the universal gas constant. Here, Equation 3.8 is normalized to 25°C, hence f_T(25°C) = 1. It features an initial increase of g_m with T_l (10-35°C) and decline at high T_l, thus allowing simulations of high temperature inhibition.

Different forms of the water stress term have been applied to g_m in canopy models (Keenan et al. 2010a; Egea et al. 2011; Oliver et al. 2012). For convenience, we retain the original water stress function in CLM4 (Oleson et al. 2010), which has already been applied to V_{cmax} and stomatal conductance g_s (Bonan et al. 2011). In the CLM4a formulation,

$$f_w(\theta) = \sum_i^n f_{root,i} \cdot w_i(\theta) \qquad (3.9)$$

where n is the total number of soil layers; $f_{root,i}$ is the root fraction within soil layer i; $w_i(\theta)$ is the plant wilting factor, derived from the soil water content θ for each layer. The calculation of $f_{root,i}$ and $w_i(\theta)$ follows Oleson et al. (2010). The term $f_w(\theta)$ ranges from 1 (wet soil) to ~0 (dry soil), depending on the soil water potential of each layer, and root distribution of PFTs.

3.3.2. Implementation of the mesophyll conductance model in CLM4a

Equation 3.1 is applied to a single leaf and its associated parameters were derived from leaf-level measurements. We then integrate this equation to describe the canopy-mean g_m for the calculation of canopy-level photosynthesis. Many land models for climate simulations, including CLM4, divide the canopy into sunlit and shaded fractions (Dai et al. 2004). Thus the canopy-mean g_m is obtained by integrating its leaf-level values over the canopy depth for sunlit and shaded fractions separately:

$$\overline{g_{\max\_sun}} = g_{\max 0}\frac{\int_0^L \exp(-k_g \cdot x)\cdot f_{sun}(x)dx}{\int_0^L f_{sun}(x)dx} = g_{\max 0}\cdot\frac{k_b}{k_g+k_b}\cdot\frac{1-\exp[-(k_g+k_b)\cdot L]}{1-\exp(-k_b\cdot L)} \tag{3.10a}$$

$$\begin{aligned}\overline{g_{\max\_sha}} &= g_{\max 0}\frac{\int_0^L \exp(-k_g \cdot x)\cdot[1-f_{sun}(x)]dx}{\int_0^L [1-f_{sun}(x)]dx} \\ &= g_{\max 0}\cdot\frac{k_b}{k_g(k_g+k_b)}\cdot\frac{k_b-(k_g+k_b)\cdot\exp(-k_g\cdot L)+k_g\cdot\exp[-(k_g+k_b)\cdot L]}{\exp(-k_b\cdot L)-1+k_b\cdot L}\end{aligned} \tag{3.10b}$$

Here, L is the leaf area index; k_b is the direct beam extinction coefficient that is used to calculate $f_{sun}(x)$ and $f_{sha}(x)$, the fractions of sunlit and shaded leaves respectively. Note that k_I in Equation 3.6 and 3.7 differs from k_b in that k_I is a seasonal mean while k_b varies with solar zenith angle and thus the course of a day and throughout a year and hence is typically updated each time step in model simulations.

Mesophyll conductance links the CO_2 concentration at leaf chloroplast c_c and that at intercellular air space C_i with the net carbon assimilation rate A through

$$c_c = c_i - A_n / g_m \,. \tag{3.11}$$

Note that here c_c and c_i are in the unit of Pa because A and g_m are in the unit of μmol m^{-2} s^{-1} and μmol m^{-2} s^{-1} Pa^{-1}; elsewhere in the paper CO_2 concentrations are expressed in the unit of ppm. The CLM4a used a numerical scheme to solve for photosynthesis by iterating over c_i. In the g_m-enabled CLM4a, we iterate over c_c and A is calculated with the photosynthesis model from C_c. Sun et al. (2012a) found that the original numerical scheme used in CLM4a cannot ensure convergence for iteration and proposed a Newton-Raphson method to overcome the numerical problem. The numerical method of Sun et al. (2012a) (also Chapter 5) is used in this present study.

The term $g_{\mathrm{max}0}$ is obtained from M_{a0} which in turn is calculated from the inverse of the canopy-top specific leaf area SLA_0 (m^2 g^{-1} C), a parameter already specified in CLM4 (Figure 3.1). M_{a0} (g m^{-2}) in Equation 3.2 differs from 1/ SLA_0 (g C m^{-2}) by a factor of two because the former refers to total leaf dry mass while the latter includes only the carbon fraction. Our g_m treatment is applicable only to C_3 plants; the C_4 photosynthesis calculations are unchanged in the present study. This is because Equations 3.1-3.8 were obtained only from C_3 plants, while C_4 species measurements were sparse.

3.3.3. Recalibration of the photosynthetic parameters

The CLM4a model currently does not represent mesophyll conductance and its default photosynthetic parameters are “apparent” photosynthetic parameters. These apparent parameters must be recalibrated after the g_m model is introduced. As shown later, without proper recalibration, the simultaneous use of the apparent photosynthetic parameters and g_m model will erroneously reduce the estimated mean annual global GPP. To convert the apparent photosynthetic parameters in CLM4a to corresponding chloroplastic (or "true") photosynthetic parameters, we applied the nonlinear conversion function developed by Chapter 2:

$$y = x\exp\left(p\frac{x^v}{g_m^q + u}\right). \tag{3.12}$$

Here (x, y) represents the pairs of apparent and chloroplastic maximum carboxylation rate V_{cmax}, maximum electron transport rate $J_{\max}$, and triose phosphate utilization rate TPU; p, q, u, and v are empirical constants and differ among these pair (i.e., a, b, c, and d in Table 2.2). As demonstrated in Chapter 2, the conversion function Equation 3.12 works very well for V_{cmax} ($R^2 = 0.83$), $J_{\max}$ ($R^2 = 0.97$), and TPU ($R^2 = 0.99$).

The CLM4a accounts for the influence of day length $f(D)$ and nitrogen limitation $f(N)$ on V_{cmax} (adjusted to 25°C), i.e., $V_{\mathrm{cmax}} = V_{c\max}^0 \cdot f(N) \cdot f(D)$. Here $V_{c\max}^0$ is the value of $V_{c\max}$ when day length and nitrogen are not limiting. The same $f(N)$ and $f(D)$ are propagated to $J_{\max}$ and TPU (25°C) via their linear dependence on V_{cmax}. We performed the recalibration, i.e., Equation 3.12, on the non-limiting apparent parameters (PFT-specific) and then applied the factors of $f(N)$ and $f(D)$ to the corresponding chloroplastic values. In this way, we preserved the functional relationships among the chloroplastic photosynthetic parameters, which are different from those among the apparent photosynthetic parameters (Chapter 2). Finally, the conversions of photosynthetic parameters were all performed on values at canopy top so that the vertical profiles of photosynthetic parameters were not altered. In short, the canopy integration strategy of the g_m-enabled CLM4a is identical to that of the original CLM4a.

3.3.4. Model simulations

We carried out multiple simulations to clarify and quantify the effect of mesophyll conductance (Table 3.2): the CONTROL run, a control simulation with CLM4a which contains the improved formulations of leaf photosynthesis, radiative transfer and canopy scaling of (Bonan et al. 2011) but has no explicit representation of g_m; the INTERMEDIATE run, a simulation that incorporates the developed g_m scheme only but retains the original apparent photosynthetic parameters in CLM4a; and the MESOPHYLL run, a simulation with both explicit consideration of g_m and chloroplastic photosynthetic parameters. The INTERMEDIATE run serves as a middle step to illustrate the g_m effect. The simulations were driven by atmospheric forcings from 1948 to 2004 (Qian et al. 2006) as used by Bonan et al. (2011). All runs were conducted at a spatial resolution of 0.9×1.25 degree with the constant land cover for the year 2000. They are all driven by observed transient atmospheric CO_2 concentrations. Overall, our simulations follow the protocols of Bonan et al. (2011).

3.4. RESULTS

The CONTROL simulation with CLM4a (Bonan et al. 2011) estimates the global annual GPP to be ~130 Pg C yr^{-1} averaged over the period of 1982-2004 (Figure 3.2a, also Bonan et al. 2011). Here CLM4a is an improved model version of CLM4 (Oleson et al. 2010) and incorporates multiple revisions by Bonan et al. (2011), which hindcasts GPP that matches better with estimates from flux data. The INTERMEDIATE simulation that enables the g_m model in CLM4a but retains its original apparent photosynthetic parameters, show that global annual GPP is reduced by ~11 Pg C yr^{-1} (Figure 3.2b and d) as compared with CONTROL. This reduction is caused by two factors. Firstly, the mesophyll diffusion process draws down the CO_2 available for carbon assimilation. Secondly, the apparent photosynthetic parameters are smaller than they should be (as compared with the corresponding chloroplastic photosynthetic parameters, Chapter 2). We found that the GPP decrease is throughout the globe, but most prevalent in the tropics (up to 1000 gC m^{-2} yr^{-1}, Figure 3.2d). The comparison between CONTROL and INTERMEDIATE runs indicate that it is important to update the apparent photosynthetic parameters to the corresponding chloroplastic photosynthetic parameters in models that represent g_m explicitly; without doing so, the models would not be self-consistent.

The use of a g_m model together with chloroplastic photosynthetic parameters in the MESOPHYLL run leads to an increase of estimated average global annual GPP by ~9 Pg C yr^{-1} compared to CONTROL over the period from 1982 to 2004 (Figure 3.2c and e). Again, the tropics exhibit the largest increase, particularly in the Amazonian region, while the boreal and temperate ecosystems show slightly increased estimates of productivity.

To understand the controls on the difference in annual GPP between the MESOPHYLL and CONTROL runs, we analyzed the annual difference from 1948 to 2004. During this period, the atmospheric CO_2 increased from about 310 to 380ppm. Overall the difference in the simulated annual GPP (MESOPHYLL – CONTROL) grows from 1950 to 2004 (Figure 3.3a) and is strongly correlated with atmospheric CO_2 concentrations (R^2=0.85, Figure 3.3b). The trend is about 27 Pg C y^{-1} per 1000 ppm. However, the atmospheric CO_2 concentration is not the only factor that drives the difference between the MESOPHYLL and CONTROL run. Climate must also contribute as superimposed on the increasing trend is some noticeable interannual variability, which cannot be explained by variability of CO_2 concentration. In particular, an abrupt drop in the difference is found around 1997/1998 (Figure 3.3a) when CO_2 concentration was ~360ppm high (Figure 3.3b). This observed variability is likely a consequence of the influence of climate variation on g_m, which in turn exerts additional modification on the difference in the simulated CO_2 fertilization effect between the MESOPHYLL and CONTROL runs.

We break down this global analysis for different latitudinal bands of the globe (Figure 3.4). It reveals that the tropical region of 15°N to 15°S (Figure 3.4a and b) and the boreal region of 45 to 60°N (Figure 3.4g) dominate the global trend of the annual GPP difference between the MESOPHYLL and CONTROL runs. The tropical and boreal regions contribute a trend of roughly 6 and 7 Pg C Pg C y^{-1} per 1000 ppm, respectively. The trends in intermediate latitudinal bands (15 to 45°N, Figure 3.4c and e; and 15 to 45°S, Figure 3.4d and f) are much smaller. It is interesting to note that most A/C_i curves are measured in temperate regions. A/C_i curve measurement conditions probably occur more frequently within this climate zone than in tropical or boreal regions which have more extreme environments. Thus the application of the apparent photosynthetic parameters is more likely to produce valid results in the temperate regions than in tropical and boreal regions. This explains why the trends are stronger in tropical and boreal regions than in temperate zones.

Figure 3.5 compares the CO_2 drawdown (in terms of CO_2 partial pressure, Pa) from atmosphere (C_a) to leaf intercellular air space (denoted as $C_a - C_i$) and then to chloroplast ($C_i - C_c$) for different biomes. For all biomes, the probability density function (PDF) of $C_a - C_i$ exhibits similar distributions in both the CONTROL (Figure 3.5a-d) and MESOPHYLL simulations (Figure 3.5e-h). This similarity is due to the fact that the drawdown of $C_a - C_i$ is governed by stomatal conductance, which is calculated with the same stomatal conductance model independently from g_m. The CO_2 drawdown for tropical evergreen trees (Figure 3.5a and e) and grass (Figure 3.5d and h) peaks around 8~9 Pa, corresponding to a frequency of 15%. The PDFs for temperate (Figure 3.5b and f) and boreal forests (Figure 3.5c and g) show similar shapes but widen considerably relative to tropical evergreen trees and grass. This is a consequence of mixed leaf structures of multiple PFTs in temperate and boreal forests, e.g. needleleaf evergreen, broadleaf evergreen, and broadleaf deciduous trees, which have varying magnitudes of $C_a - C_i$ (Figure 3.6 and 3.7). The additional drawdown of $C_i - C_c$ is determined by g_m and exhibits different distribution patterns from $C_a - C_i$ (Figure 3.5i-l). The PDFs for $C_i - C_c$ show various shapes depending on biomes. Tropical evergreen trees have a unimodal distribution with a maximum probability occurring around 12-13 Pa; this maximum is larger than that of $C_a - C_i$. This suggests that g_m is of particular importance for tropical evergreen trees; it helps to explain the large sensitivity of GPP variation to g_m representation in the tropics (Figure 3.4a and b). The PDFs of temperate and boreal forests show multimodal shapes (Figure 3.5g-k), resulting again from a mixture of different leaf structures in the same climate zone (Figure 3.6 and 3.7). The difference between C_i and C_c is more converging for grass than for other biomes and has a smaller magnitude (Figure 3.5l), indicating a less critical role of g_m than stomatal conductance on grass species.

The diffusion and transport of CO_2 inside leaves is a complicated process, i.e., from gas-phase in leaf intercellular spaces to liquid phases in cell walls, cytosol, chloroplast stroma, plasmalemma, chloroplast envelop membranes and finally chloroplast stroma (Flexas et al. 2012), but is usually characterized by a single parameter g_m. Our modeling framework of g_m builds on the latest advances from field plant physiological studies, which consistently found that the variation of g_m depends on both leaf traits and environmental conditions. Although simplified, this model is effective to realistically represent the CO_2 diffusion process inside leaf. For example, the simulated bulk CO_2 drawdown from C_i to C_c at canopy level is consistent with leaf-level measurements (Warren 2008). Another evidence is the ratio of CO_2 concentration/partial pressure among different sites (Figure 3.8-3.10), e.g., the PDF of C_c / C_i peaks around 0.7 over tropical evergreen trees, which also agrees well with field observations (Warren 2008). These findings also suggest the convergence of CO_2 drawdown between leaf and canopy scale.

3.5. DISCUSSION

The dependence of g_m on environmental conditions is of particular importance, which may possibly explain the influence of climate variability, e.g., ENSO, on GPP sensitivity to CO_2. Mesophyll conductance not only responds rapidly to but also acclimates gradually to environment changes (Flexas et al. 2008; Niinemets et al. 2009a; Warren 2008). Here, the long-term acclimation of g_m is not considered since our simulations were carried out in a relatively short period; this effect may become critical as climate continues to warm and dry.

It is a common modeling practice to fine tune parameters strategically so that large-scale models can reconcile structural deficiencies and fit present day observations well. Here we show that parameter adjustment is not adequate for environmental conditions that may vary beyond the observational conditions to which model parameters have been optimized. Thus a reliable model that is capable of simulating the past and future climate should be process-oriented. Here we use a simple conversion function to build the link between the photosynthetic parameters in current global climate models and their true values as g_m is explicitly considered. This is a simplified strategy for our analyses to proceed. A more plausible way is to refit these parameters together with g_m from measurements of leaf gas exchange (as discussed in Chapter 2). The refitting process should cover as many species as possible in order to obtain reasonable parameters at PFT levels, which can be then applied to GCMs. The key photosynthetic parameters may also be calculated mechanistically, as demonstrated by Xu et al. (2012).

3.6. CONCLUSIONS

This study presents a mesophyll conductance modeling framework for global simulations. This g_m model is developed by synthesizing latest advances in plant physiological studies, which formulate the dependence of g_m on plant functional types and on environmental conditions. The detailed implementation of this g_m into CLM4a and procedures of parameter recalibration are documented. This study provides a benchmark to demonstrate the role of g_m in GPP simulations at global scales. In addition, with this process-oriented g_m modeling framework, we found that omission of the mesophyll diffusion process can underestimate the potential of GPP stimulation to rising atmospheric CO_2. The trend of such discrepancy is about 27 Pg C y^{-1} per 1000 ppm, with the tropics playing the major role. Our findings can be further refined as new understandings of g_m evolve in field studies and as fully coupled simulations are performed with nitrogen limitations and climate feedbacks considered.

3.7. ACKNOWLEDGEMENTS

This study was carried out at multiple institutions. The support for research at UT – Austin came from Department of Energy (DE-FG02-01ER63198). The support for research at ORNL came from U.S. Department of Energy, Office of Science, Biological and Environmental Research Program, Climate and Environmental Sciences Division. The ORNL's LDRD program also partially supported the research. ORNL is managed by UT-Battelle, LLC, for the U.S. Department of Energy under contract DE-AC05-00OR22725.

Table 3.1. Empirical constants used in the global mesophyll conductance (g_m) model.

Equation	Symbol	Value (25C)	Definition	Source
		calculation of g_{max0}		
Equation 3.1	a	24.240338	Empirical parameters	*Niinemets et al.*, 2009b
	b	-0.6509	Empirical parameters	
		vertical profile of g_m		
Equation 3.1, 3.4, 3.7	d	0.8109	Empirical parameters	*Montpied et al.*, 2009
Equation 3.5, 3.7	f	0.221897	Empirical parameters	*Niinemets*, 2007
Equation 3.6, 3.7	k_I	0.45	Seasonally averaged light extinction coefficient	
Equation 3.7	k_g	0.08971	$= k_I*d*f$	
		temperature response function of g_m		
Equation 3.8	c	20	a scaling constant	*Bernacchi et al.*, 2002
	ΔH_a	49.6×10^3 J mol^{-1}	the activation energy	
	ΔH_d	437.4×10^3 J mol^{-1}	the deactivation energy	
	ΔS	1.4×10^3 J mol^{-1} K^{-1}	an entropy term	
	R	8.314 J mol^{-1} K^{-1}	the universal gas constant	

Table 3.2. Summary of global model simulations.

Simulation	Description
CONTROL	Control simulations with the default CLM4a (Bonan et al. 2011)
INTERMEDIATE	Intermediate simulations that use CLM4a with the g_m model only but retains the original apparent photosynthetic parameters of CLM4a
MESOPHYLL	Fully updated simulations that use CLM4a with the g_m model and recalibration of photosynthetic parameters

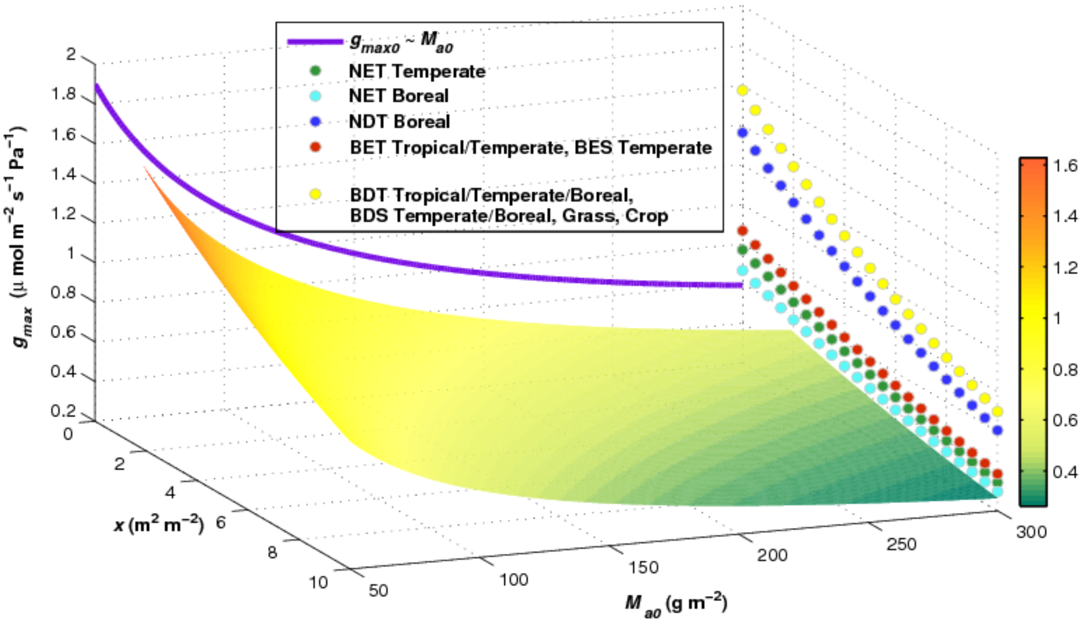

Figure 3.1. The mesophyll conductance model (scaled to the leaf temperature of 25°C and saturating soil moisture).

The 3D surface shows the maximum mesophyll conductance $g_{\max} = a \cdot M_{a0}{}^{b} \cdot \exp(-k_g \cdot x)$, (i.e., the product of Equation 3.2 and 3.7) as a function of canopy-top M_a (M_{a0}) and cumulative leaf area index (x). The purple curve in the $x = 0$ plane shows the relationship between $g_{\max 0}$ and M_{a0} (Equation 3.2). The dotted curves show the g_m profile within canopy (Equation 3.7) for the specified PFTs in CLM4a. The values of M_{a0} are PFT-specific, calculated from the canopy-top specific leaf area SLA_0 in CLM4a. For clarity, we display these dotted curves on the M_{a0}=300 (g m^{-2}) plane. Here, NET, NDT, BET, BDT, and BDS denote needleleaf evergreen tree, needleleaf deciduous tree, broadleaf evergreen tree, broadleaf deciduous tree, and broadleaf deciduous shrub, respectively.

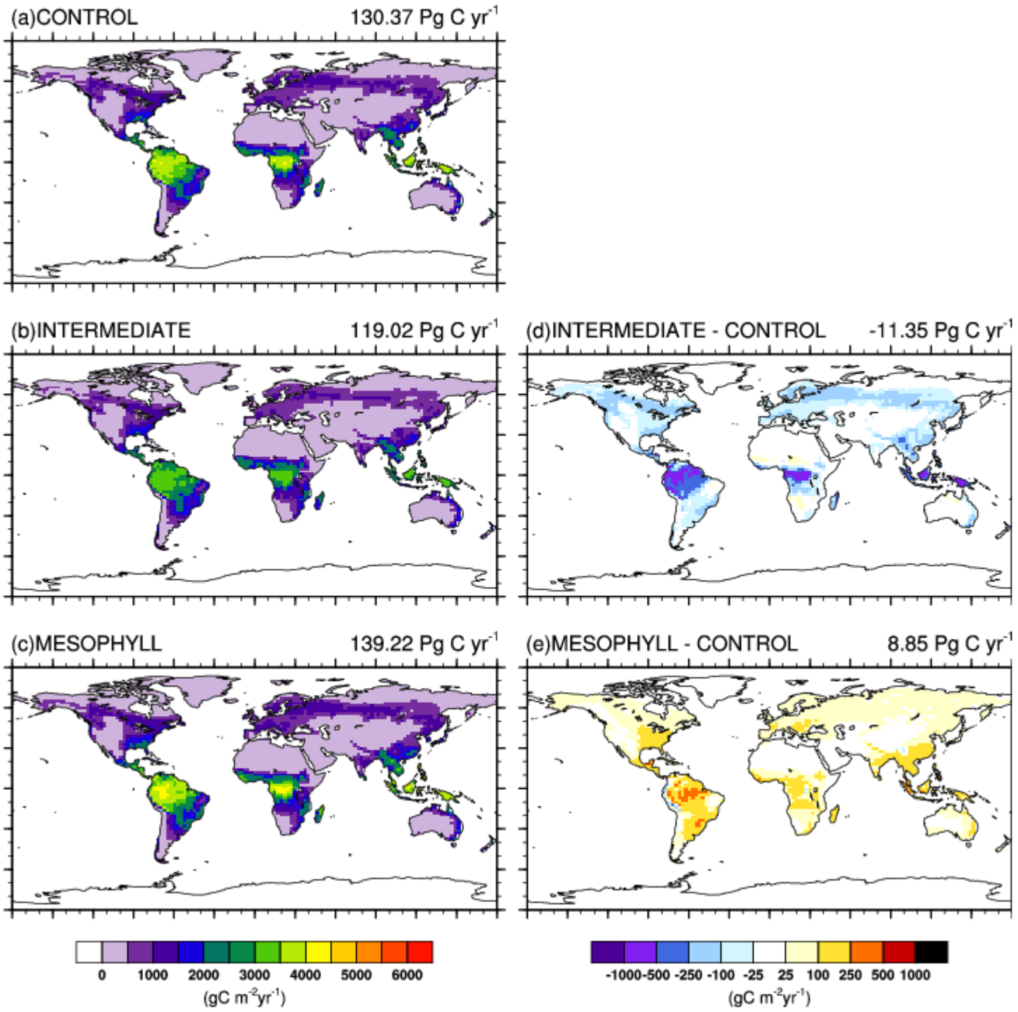

Figure 3.2. Mean annual GPP of the period 1982-2004 for the simulation of CONTROL, INTERMEDIATE, and MESOPHYLL as well as the differences among them.

Panel (a) CONTROL, the control simulation with CLM4a (Bonan et al. 2011); (b) INTERMEDIATE, the intermediate simulation with mesophyll conductance scheme only and the photosynthetic parameters are not recalibrated; (c) MESOPHYLL, the simulation with both mesophyll conductance model and recalibration of photosynthetic parameters to corresponding “chloroplastic” values; and (d)-(e) are the differences from the CONTROL simulation for the INTERMEDIATE and MESOPHYLL simulations, respectively. The unit for mean annual GPP in (a)-(e) is g C m^{-2} yr^{-1}. The value shown on the right-top of each panel is the estimated mean annual global GPP (Pg C yr^{-1}).

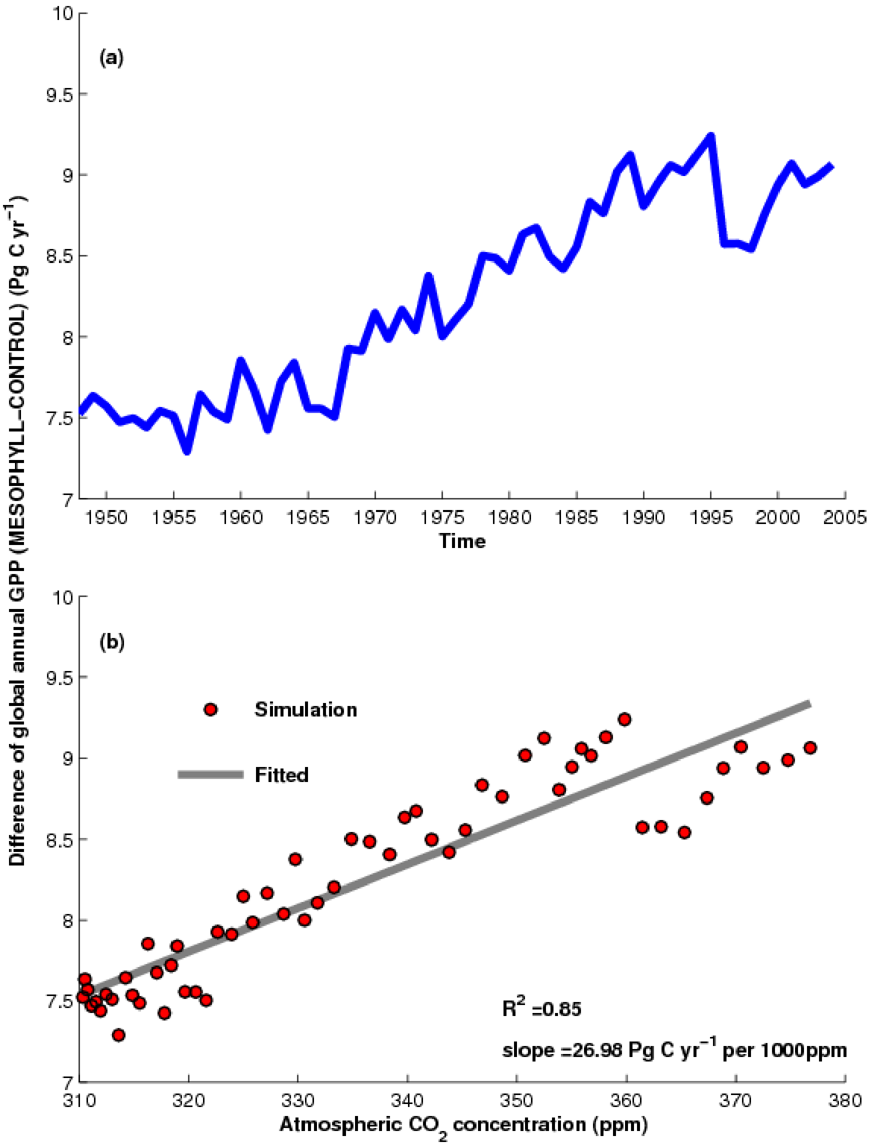

Figure 3.3. The difference of global annual GPP between the MESOPHYLL and CONTROL simulations from 1948 to 2004 and its dependence on corresponding atmospheric CO_2 concentration.

Panel (a) the time series of the difference of global annual GPP between the MESOPHYLL and CONTROL simulations from 1948 to 2004; and (b) the dependence of GPP difference on atmospheric CO_2 concentration.

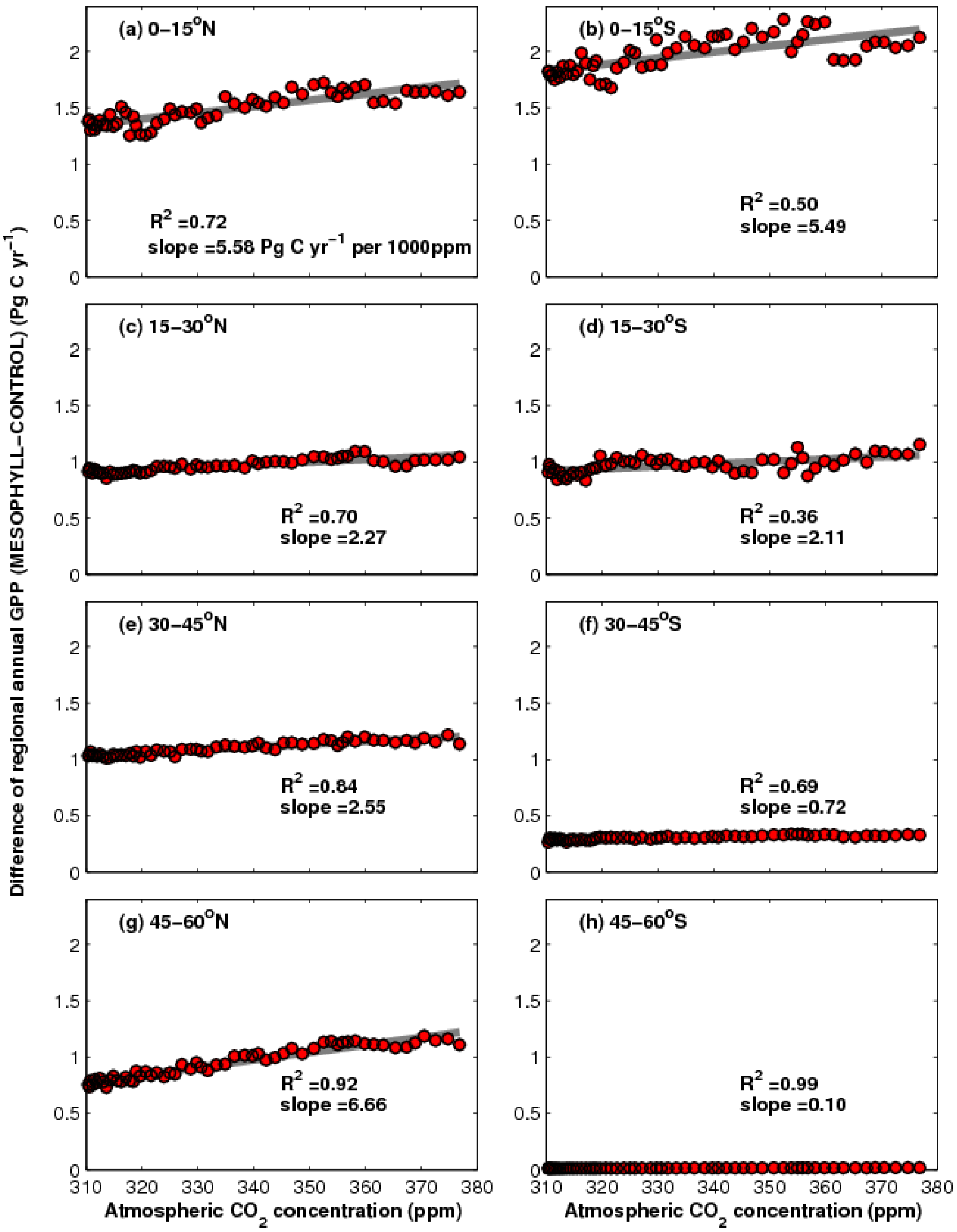

Figure 3.4. The difference in annual GPP between the MESOPHYLL and CONTROL simulations for each 15° latitudinal band of the globe as a function of atmospheric CO_2 concentrations from 1948 to 2004.

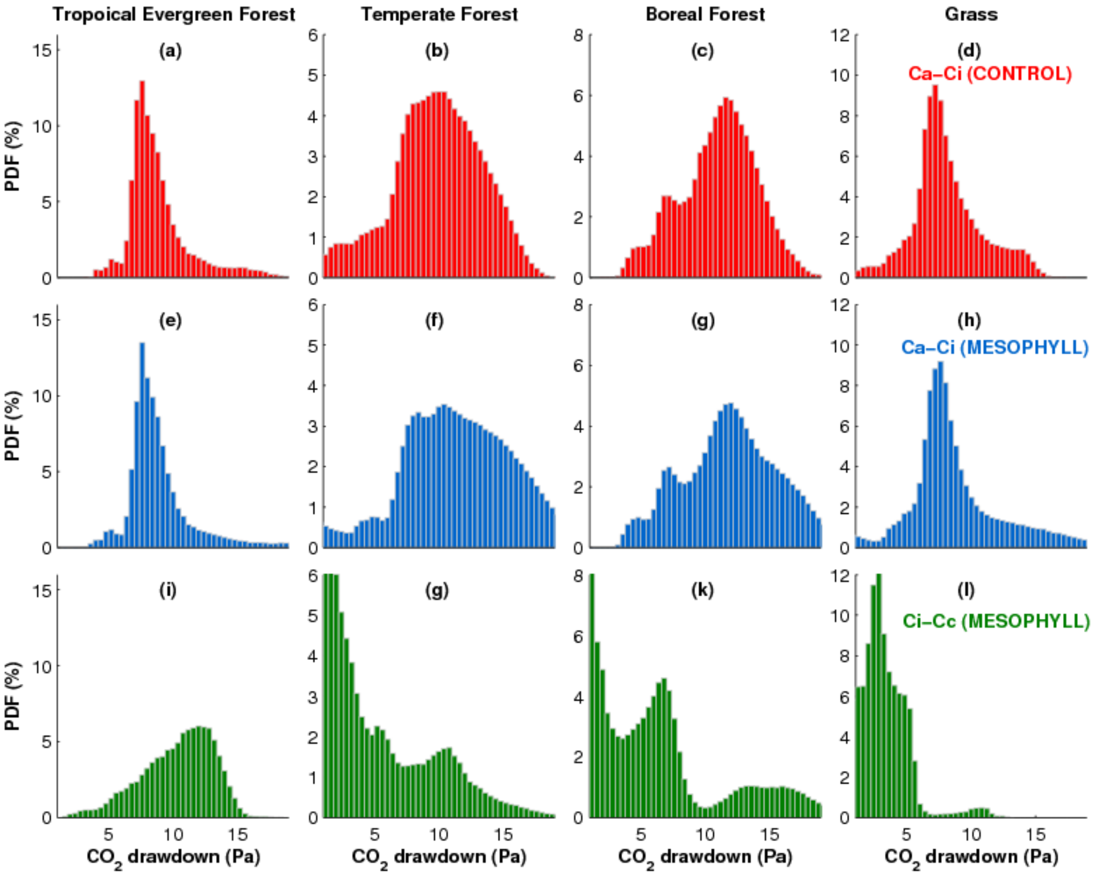

Figure 3.5. The probability density distribution function (PDF) of CO_2 drawdown for selected biomes, i.e., Tropical Evergreen Forest, Temperate Forest, Boreal Forest, and Grass.

The CO_2 drawdown here is defined in terms of partial pressure (Pa). Panels (a)-(d) show CO_2 drawdown from atmosphere (C_a) to leaf intercellular space (C_i), i.e., C_a - C_i, for the CONTROL simulation with CLM4a. (e)-(h) show the PDF of C_a - C_i for the full MESOPHYLL run; and (i)-(l) are for the CO_2 drawdown between intercellular space (C_i) and chloroplast (C_c), i.e., C_i - C_c. Each column represents a single biome. From leaf to right are Tropical Evergreen Forest, Temperate Forest, Boreal Forest, and Grass.

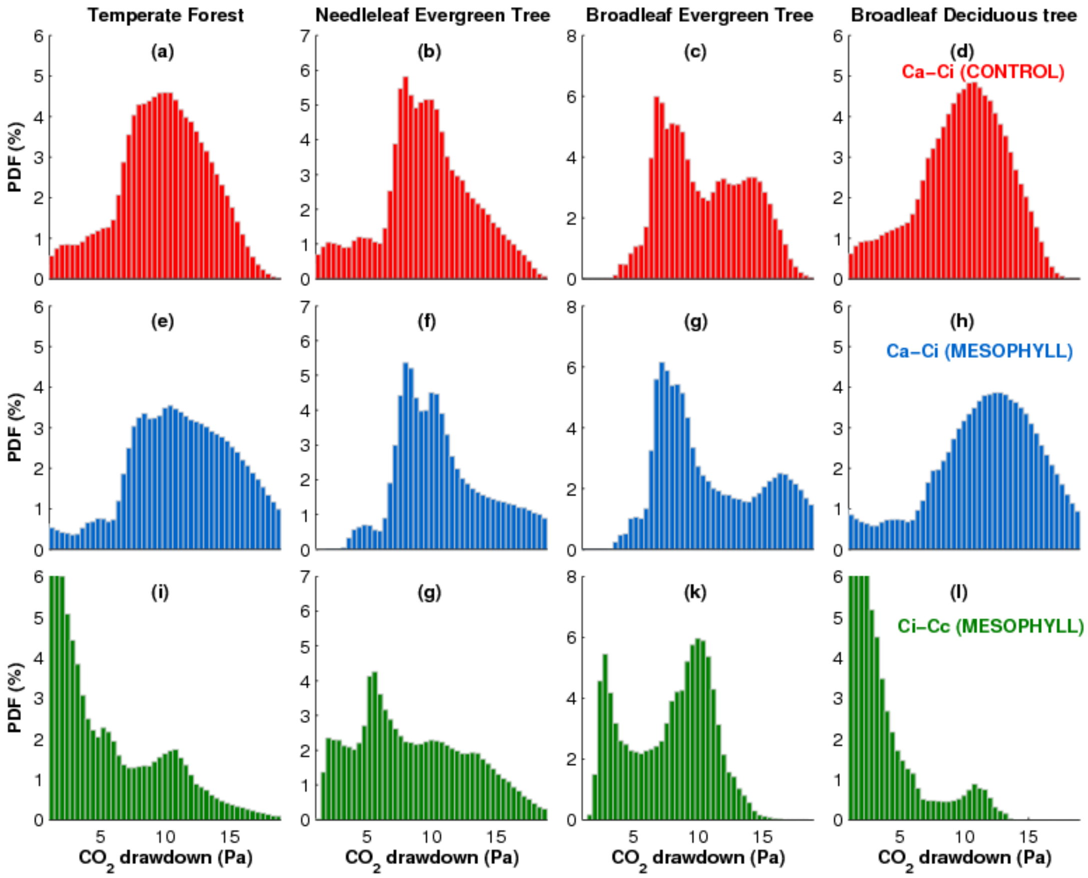

Figure 3.6. Same as Figure 3.5 except for the breakdown of the temperate forest.

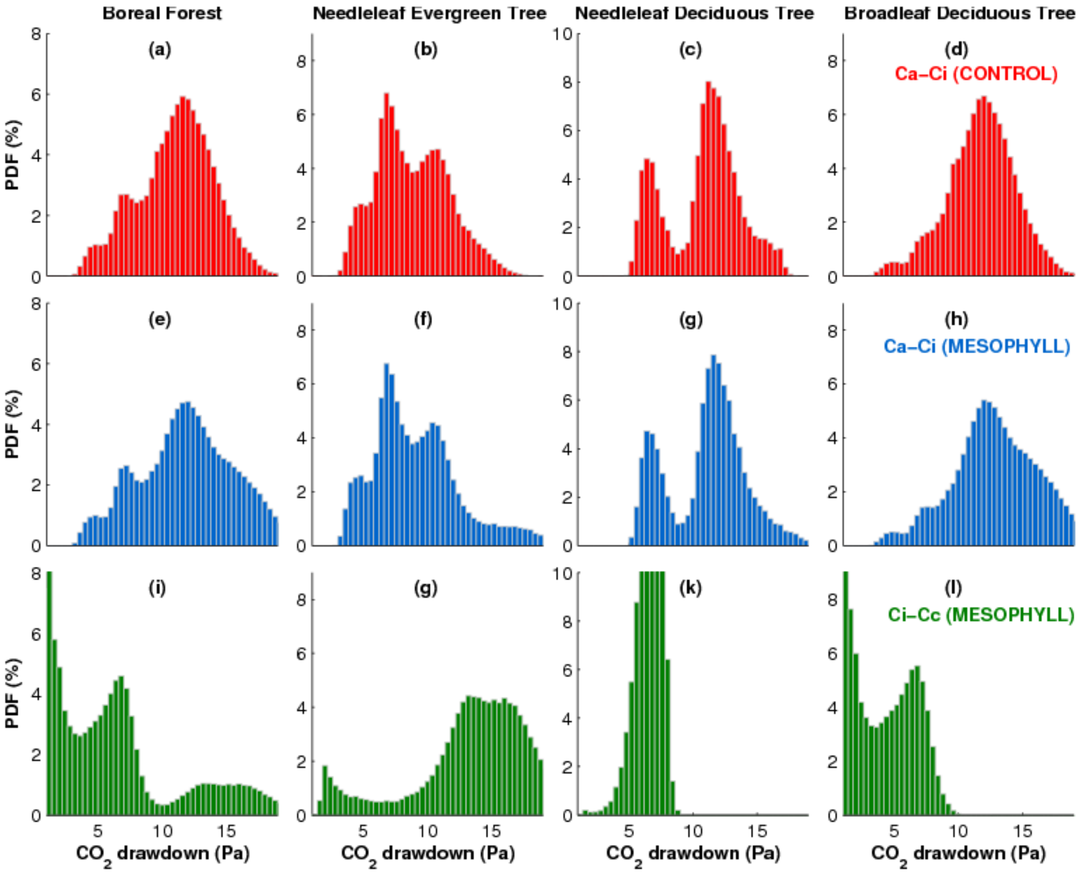

Figure 3.7. Same as Figure 3.5 except for the breakdown of the boreal forest.

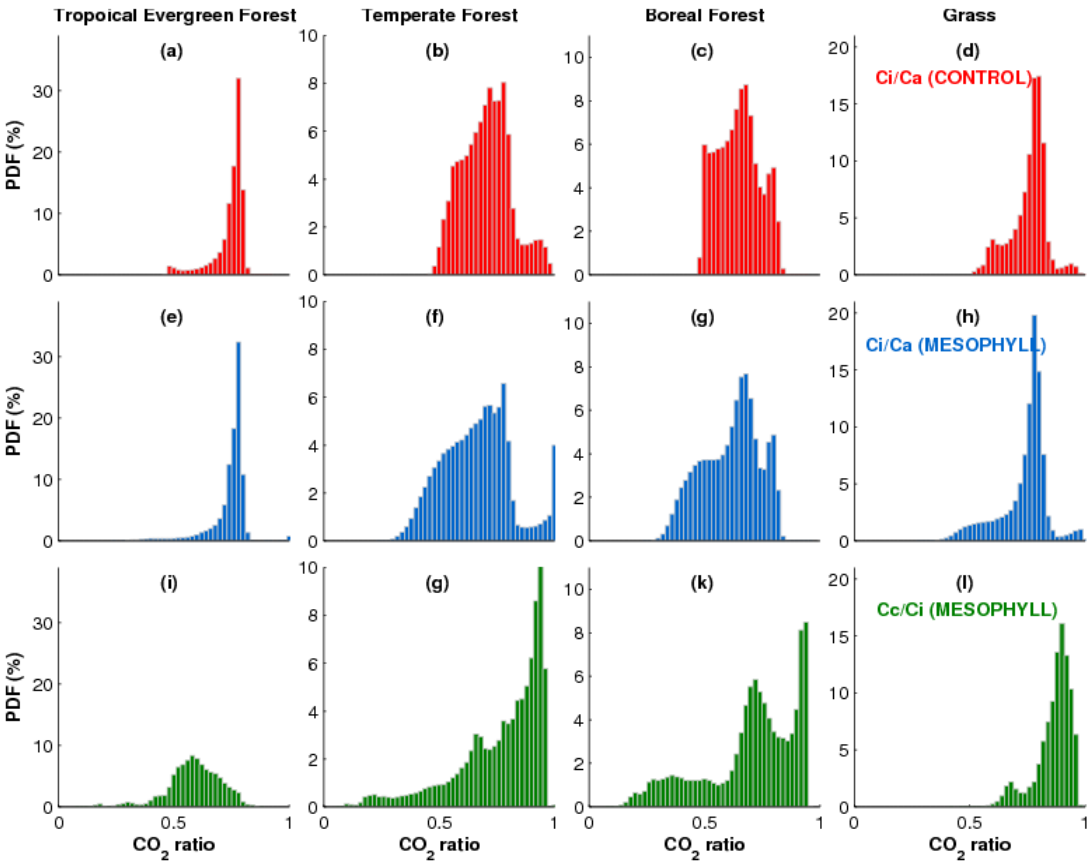

Figure 3.8. The PDFs of C_i / C_a ratio and C_c/ C_i ratio for selected biomes, i.e., Tropical Evergreen Forest, Temperate Forest, Boreal Forest, and Grass.

Panels (a)-(d) show the PDF of the C_i / C_a ratio for the CONTROL simulation with CLM4a. (e)-(h) show the PDF of the C_i / C_a ratio for the full MESOPHYLL run and (i)-(l) are for the C_c/ C_i ratio. Each column represents a single biome. From leaf to right are Tropical Evergreen Forest, Temperate Forest, Boreal Forest, and Grass.

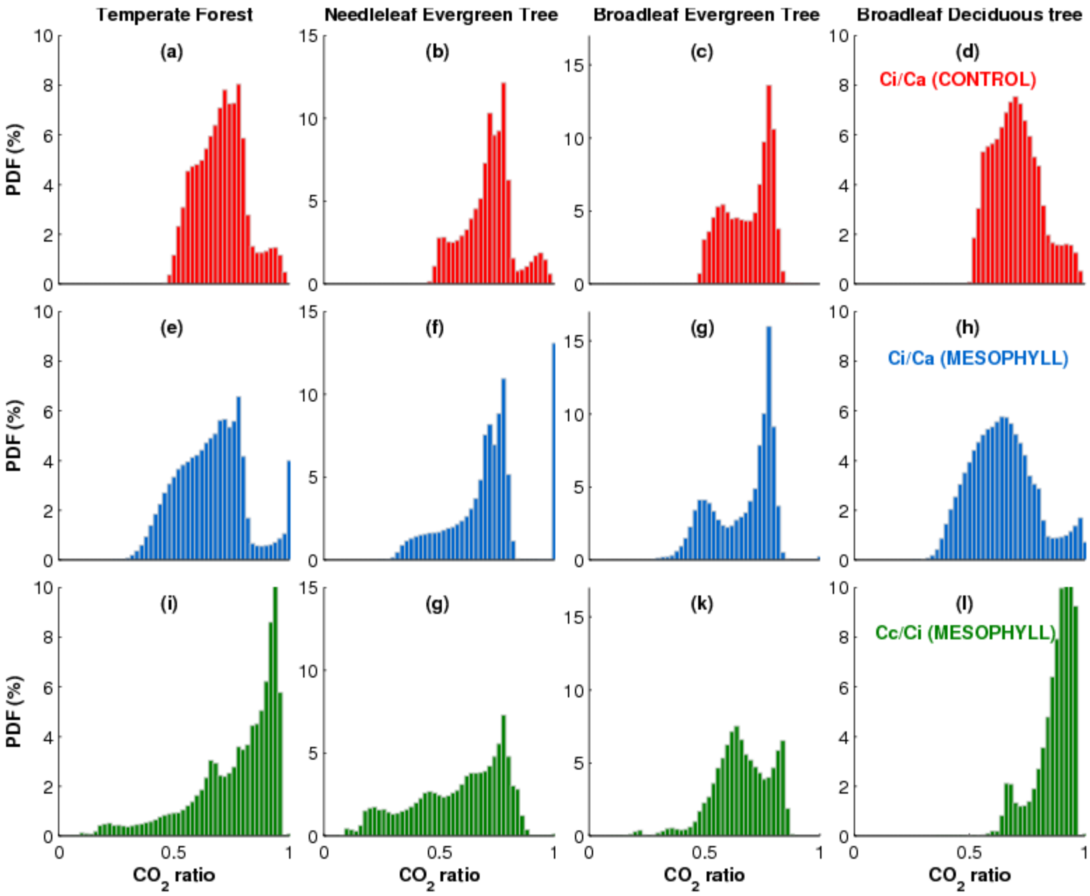

Figure 3.9. Same as Figure 3.8 except for the breakdown of the temperate forest.

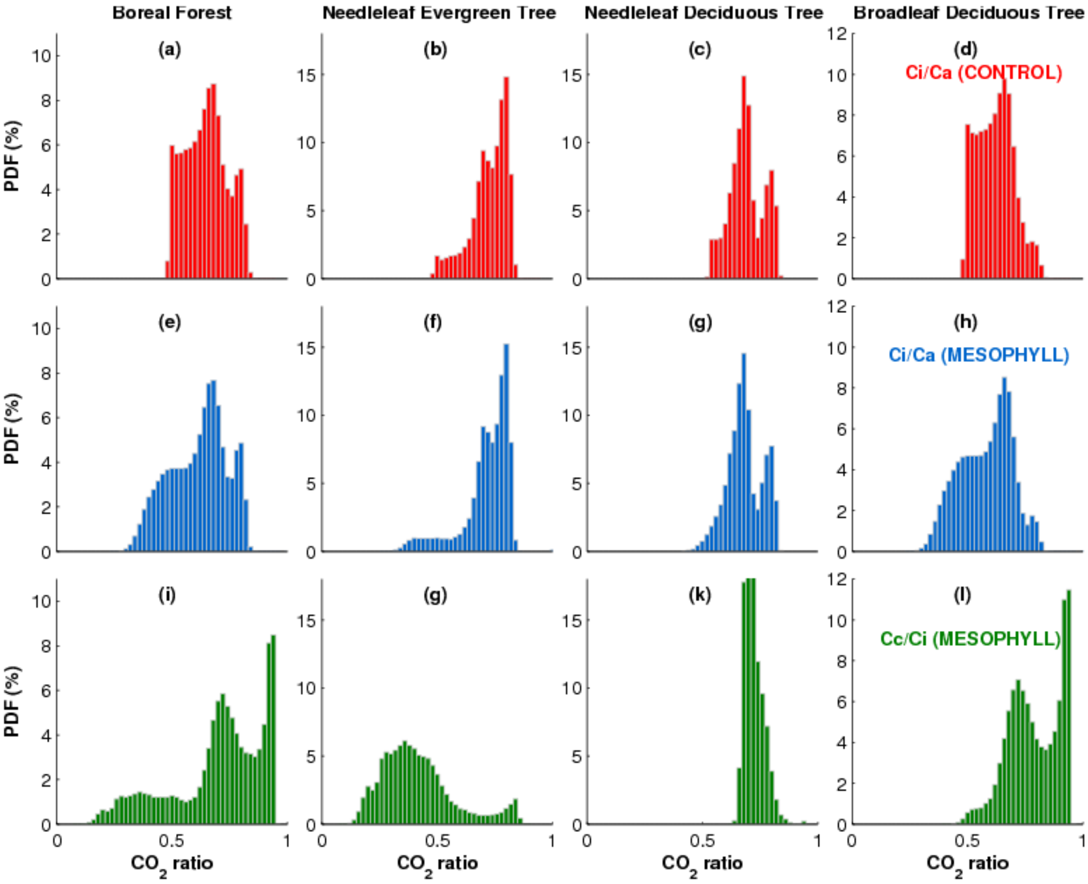

Figure 3.10. Same as Figure 3.8 except for the breakdown of the boreal forest.

Chapter 4: Model underestimation of terrestrial carbon assimilation from Pre-Industrial: Role of mesophyll resistance to CO_2 diffusion

4.1. ABSTRACT

CO_2 concentrations drop from substomatal cavities to chloroplasts due to the presence of substantial resistance to diffusion in mesophyll layers. Current global carbon cycle models ignore this drop. To compensate for over-predicted CO_2 availability at the site of photosynthesis, they use apparent photosynthetic parameters tuned to measurements obtained for narrowly controlled environmental conditions. These apparent parameters are smaller than the ones that quantify the true capacities of photosynthetic machinery. Here we show that these models underestimate the responsiveness of terrestrial biosphere to increased atmospheric CO_2 concentrations for natural environmental conditions. This underestimation occurs because tuned apparent parameters do not represent the underlying properties of limiting biochemical processes and they only work phenomenologically for narrow measurement conditions. From 1850 to 2004, the global gross primary production may be underestimated by a cumulative total of 113 to 148 Pg C, a magnitude equivalent to one full year's gross photosynthesis of the global terrestrial biosphere or to the entire global fossil CO_2 emissions from 1850 to the mid-1970s. The terrestrial biosphere may be more CO_2-limited and absorb more carbon with increased atmospheric CO_2 concentrations than previously thought.

4.2. INTRODUCTION

CO_2 diffuses from leaf intercellular air space to chloroplasts where carboxylation occurs. This diffusion is an important process limiting CO_2 availability for photosynthesis (Evans et al. 1986; Harley et al. 1992; Warren 2008; Niinemets et al. 2009a; Flexas et al. 2012; Sharkey 2012; Evans and von Caemmerer 2013). Along this diffusional pathway, the CO_2 passes through not only gases initially but also liquids and lipids, i.e., cell wall, plasmalemma, cytosol, chloroplast envelope and stroma. Compared with the gas phase-only diffusion across stomata, this internal diffusional pathway is shorter (Niinemets et al. 2011). However, CO_2 diffusion in liquids is several orders of magnitude slower than in gases and the diffusion in lipids is even slower than in liquids (Evans et al. 2009). Mesophyll conductance (g_m, also referred to as internal conductance), which characterizes this internal diffusional process of CO_2, has been measured on hundreds of species around the world (Flexas et al. 2008; Niinemets et al. 2009a,b). These studies conclude that mesophyll structures and stomata present a similar magnitude of resistance to CO_2 diffusion and thus are equally important in controlling CO_2 concentrations available at the site of photosynthesis. Leaf-level studies suggest that the drawdown of CO_2 from substomatal cavities to chloroplasts caused by mesophyll resistance to diffusion may reduce photosynthesis by 25-75% for different plant species (Terashima et al. 2006). Without explicit representation of g_m, models substantially over-predict CO_2 concentrations available at the chloroplasts. Consequently, photosynthesis may seriously be either overestimated or underestimated, depending on how the model parameters are tuned, the magnitude of g_m, and environmental conditions (Niinemets et al. 2009c).

Although the CO_2 diffusional process inside leaves is important for understanding photosynthetic responses to environmental changes, current large-scale terrestrial carbon cycle models do not represent mesophyll diffusion explicitly. It is not clear whether this lack of representation of mesophyll diffusion constitutes a major deficiency for large-scale models, particularly in their capacity to predicting terrestrial ecosystem responses to rising atmospheric CO_2 concentrations. A myriad of hierarchical processes affect terrestrial carbon cycling and not every important process can and should be directly represented in carbon cycle modeling frameworks. More process representations often mean additional parameters and if these parameters cannot be adequately estimated, new uncertainties may be introduced (Gulden et al. 2008). Only those processes that cannot be adequately compensated for by tuning parameterizations at higher levels should be represented directly in large-scale models.

Can large-scale carbon cycle models adequately cover the net effects of mesophyll diffusion without representing this important process explicitly? Current carbon cycle models generally employ some version of the biochemical model of Farquhar, von Caemmerer, and Berry (FvCB) for modeling photosynthesis (Farquhar et al. 1980). The FvCB model requires the CO_2 concentration (C_c) at the carboxylation site, i.e., at the chloroplast (Niinemets et al. 2009b). However, most modelers have, rather, applied the FvCB model to the CO_2 concentration inside the substomatal cavity (C_i) even though, as already mentioned, C_c is much smaller than C_i, owing to the presence of substantial mesophyll resistance to CO_2 diffusion. To be consistent with the direct application of the FvCB model to C_i, carbon cycle models also use photosynthetic parameters estimated with data fitting procedures that treat g_m as if it were infinitely large (i.e., the fitting ignores mesosphyll diffusion limitation). These parameters include the maximum carboxylation rate (V_{cmax}), maximum electron transport rate (J_{max}), and triose phosphate utilization rate (TPU), all estimated from leaf gas exchange measurements, commonly referred to as A/C_i curves (Long and Bernacchi 2003; Sharkey et al. 2007). Such parameter estimation procedures that ignore mesophyll diffusion limitation often have difficulty in fitting the curvature of A/C_i curves, with positive biases at some C_i ranges being compensated for by negative biases at other ranges (Ethier and Livingston 2004; Gu et al. 2010; Niinemets et al. 2009b). Because the parameter estimation procedures do not consider directly mesophyll diffusion limitation, photosynthetic parameters applied in current carbon cycle models are "apparent" parameters that are "optimized" for certain conditions.

These apparent photosynthetic parameters are smaller than the corresponding ones that quantify the chloroplastic capacities of photosynthetic machinery of the leaf, i.e., the chloroplastic photosynthetic parameters (Ethier and Livingston 2004; Niinemets et al. 2009b,c; Zeng et al. 2010). Like the apparent ones, the chloroplastic photosynthetic parameters can also be estimated from leaf gas exchange measurements but with procedures that infer g_m together (Ethier and Livingston 2004; Sharkey et al. 2007; Niinemets et al. 2009b,c; Zeng et al. 2010; Gu et al. 2010; Evans and von Caemmerer 2013). Smaller apparent photosynthetic parameters are a consequence of overestimation of CO_2 concentrations at the site of photosynthesis when g_m is assumed infinite. In other words, the parameter estimation procedures have to lower the apparent values of photosynthetic parameters in order to optimize, phenomenologically, against the observed A/C_i curves.

Is the use of such apparent photosynthetic parameters an adequate strategy for carbon cycle models to simulate terrestrial responses to increased atmospheric CO_2 concentrations? It is legitimate to ask this question because A/C_i curves are measured with strict environmental controls whereas carbon cycle models are applied over a wide range of unpredictable natural environmental conditions. To measure A/C_i curves, photosynthetically active radiation (PAR) is typically set at saturating levels (>1000 μmol m^{-2} s^{-1}) and temperatures and relative humidity at moderate values (e.g., summer growth temperatures with 60 to 80% relative humidity). This strict control of the A/C_i curve measurement conditions is not a weakness of the measurement itself but a necessity for obtaining data about key limiting biochemical processes of photosynthesis (Long and Bernacchi 2003; Sharkey et al. 2007). While the use of apparent photosynthetic parameters may not produce obvious problems within the conditions for which they are optimized, serious issues may arise if deviations from these optimized conditions occur because the apparent parameters do not represent the underlying properties of fundamental biochemical processes and are not expected to be universally valid. We thus hypothesize that the inherent structural defects of carbon cycle models that ignore mesophyll diffusion may not be adequately compensated for by the use of apparent photosynthetic parameters in simulating ecosystem responses to long-term changes in atmospheric CO_2 concentrations. We further hypothesize that these models will underestimate ecosystem responsiveness because photosynthesis is more sensitive to changes in CO_2 at lower than at higher CO_2 and because models that ignore mesophyll diffusion over-predict CO_2 concentrations at the site of photosynthesis.

We test these hypotheses by evaluating model-simulated responses of global annual gross primary production (GPP) to the increased atmospheric CO_2 concentrations since the Industrial Revolution. Our objective is to compare models that omit and include g_m.

4.3. METHODS

4.3.1. Global simulations of GPP

We developed a simple but realistic global g_m model based on a synthesis of data in the literature, and implemented this global g_m model into the Community Land Model 4a (CLM4a), a version updated from CLM4 with improvements in canopy processes by Bonan et al. (2011) (Chapter 3). To establish the correct correspondence between CLM4a with and without g_m, the original apparent photosynthetic parameters in CLM4a were converted to the corresponding chloroplastic photosynthetic parameters to be used with the global g_m model. This conversion was done with a globally-tested nonlinear function that has the apparent parameter and g_m as inputs (Chapter 2). Details about the g_m-enabled CLM4a are described in the (Chapter 3).

We ran CLM4a with and without g_m for the period from 1850 (the end of pre-industrial era) to 2004 with constant climate and from 1948 to 2004 with observed climate. The constant climate that drives the simulations from 1850 to 2004 is repeating meteorology of 1948-1972 (Bonan and Levis 2010; Piao et al. 2013). The observed climate that drives the 1948 to 2004 simulations is from Qian et al. (2006). The observed atmospheric CO_2 concentrations, which are used in all simulations, increases from about 285ppm in 1850 to 310 ppm in 1948 to 377 ppm in 2004.

4.3.2. Quantification the CO_2 responsiveness of GPP

We employed two approaches to comparing the CO_2 responsiveness of global GPP simulated by CLM4a with and without g_m. First, we used the beta factor (β), introduced by Charles David Keeling to quantify the 'degree of CO_2 fertilization' of terrestrial biosphere (Bacastow and Keeling 1973) and widely applied since. The beta factors of CLM4a with and without g_m (β_c and β_i, respectively) were compared through their ratio R:

$$R(C_a)=\frac{\beta_c(C_a)}{\beta_i(C_a)}=\frac{[GPP_c(C_a)-GPP_c(C_{a0})]GPP_i(C_{a0})}{[GPP_i(C_a)-GPP_i(C_{a0})]GPP_c(C_{a0})}, \qquad (4.1)$$

where GPP_c and GPP_i are the global annual GPP simulated by CLM4a with and without g_m, respectively; C_a is atmospheric CO_2 concentration and C_{a0} is some baseline value of C_a, here taken as the pre-industrial 285 ppm in 1850. The denominators of β_c and β_i share a common logarithmic term, which cancels in the expression of R. If carbon cycle models with and without g_m predict the GPP sensitivity to CO_2 equally well, then R should be close enough to 1. $R > 1$ indicates that a model without g_m underestimates the sensitivity as compared with one that explicitly considers g_m; $R < 1$ indicates the opposite.

Second, we calculated the unbiased cumulative difference (Δ) between GPP_c and GPP_i:

$$\Delta(t)=\int_{t_0}^{t}\left[GPP_c(t)-GPP_c(t_0)\right]dt-\int_{t_0}^{t}\left[GPP_i(t)-GPP_i(t_0)\right]dt\,, \tag{4.2}$$

here t_0 and t are the start (1850) and a given year, respectively. GPP_c and GPP_i are each offset by their corresponding initial values in the start year and thus $\Delta(1850)=0$, allowing a fair comparison between CLM4a with and without g_m.

4.3.3. Leaf-scale evaluation

To provide insights for the global pattern of CO2 responsiveness of GPP, we carried out a meta-analysis of leaf-scale gas exchanges measurements. We analyzed a global dataset (leafweb.ornl.gov) of over 1000 quality-assured A/C_i curves measured on over 100 C_3 species covering all major plant functional types of the world from herbaceous temperate plants to woody tropical species. We applied the FvCB model together with the obtained paired sets of apparent and chloroplastic photosynthetic parameters and associated g_m values to simulate the responses of net assimilation rates of single leaves to changes in ambient CO_2 concentrations under a combination of multiple levels of PAR and temperature. To further simplify the simulations, a constant ratio of intercellular to ambient CO_2 concentrations is assumed (C_i/C_a = 0.7) (Ehleringer and Cerling 1995), avoiding uncertainties that may be caused by the use of a stomatal conductance model. The leaf-scale simulations are run with PAR at 100, 200, 400, 800, and 1600 μmol m^{-2} s^{-1}, respectively and temperatures at10, 15, 20, 25, and 30°C, respectively and also with all measurement conditions of the original A/C_i curves from which the apparent and chloroplastic photosynthetic parameters and g_m are estimated. The average measurement conditions of the original A/C_i curves are 1255 ± 323 μmol m^{-2} s^{-1} for PAR and 26 ± 5°C for temperature. We calculated R from 285 to 1000ppm ambient CO_2 concentrations for each pair of apparent and chloroplastic parameters and for each combination of PAR and temperature. For reference, we also calculated R for each of the measurement conditions of the more than 1000 original A/C_i curves from which the apparent and chloroplastic photosynthetic parameters and g_m were estimated.

4.4. RESULTS AND DISCUSSION

For the 1850-2004 simulations forced with constant climate, R increases rapidly initially when atmospheric CO_2 concentrations are less than 300 ppm (earlier than 1910). It levels off at a value of about 1.073 (Figure 4.1a). For almost the whole simulation period, R is larger than 1 except for the first few years (before 1865 and $C_a < 287$ ppm) when R is unstable (R is not defined in 1850 at $C_{a0} = 285$ ppm). For the 1948-2004 simulations forced with observed climate, R is always larger than 1 and also generally larger than the corresponding R calculated for the constant climate simulations (Figure 4.1a). R calculated for the observed climate simulations varies considerably from year to year, in contrast to a very stable R calculated for the constant climate simulations for the same period. This contrast suggests that climate variability increases the sensitivity difference of GPP to CO_2 simulated by models with and without g_m. The R consistently larger than 1 for both the constant and observed climate simulations indicates that, compared to carbon cycle models with g_m, models without g_m underestimate the degree of CO_2 fertilization.

The unbiased cumulative difference Δ in GPP provides a measure for the underestimation of the degree of CO_2 fertilization by models without g_m. Δ grows exponentially from 1850 to 2004 and reaches to 113 Pg C ($1\text{Pg} = 1\times10^{15}$ gram) for the constant climate simulations and to about 148 Pg C for the observed climate simulations (Figure 4.1b). Similar to the difference in R between the constant and observed climate simulations (Figure 4.1a), Δ is also larger for the observed than for the constant climate simulations, suggesting that increased climate variability amplifies the magnitude of underestimation of the degree of CO_2 fertilization by models without g_m.

Why do carbon cycle models without explicit representation of mesophyll diffusion underestimate the degree of CO_2 fertilization? Why does climate variability amplify this underestimation? To answer these two questions, we analyzed a global dataset (leafweb.ornl.gov) of over 1000 quality-assured A/C_i curves measured on over 100 C_3 species covering all major plant functional types of the world from herbaceous temperate plants to woody tropical species.

Results from the leaf-scale analyses are summarized in Figure 4.2. Under non-saturating PAR levels (Figure 4.2a-c), the R, which is averaged across all A/C_i curves, is significantly larger than 1 across the full range of ambient CO_2 for all temperature levels examined. For a given PAR level, the averaged R tends to decrease with increased temperatures. For a given combination of PAR and temperature, the averaged R tends to increase with CO_2 and level off at high CO_2. Only under saturating light levels and high temperatures is the averaged R close to 1. When evaluated at the measurement conditions of original A/C_i curves, the averaged R is also close to 1. Thus the leaf-scale analyses show that only for conditions close to what the apparent photosynthetic parameters are optimized for, can models without g_m predict a degree of CO_2 fertilization similar to that by models with g_m. However, when PAR and temperatures deviate from the general measurement conditions of A/C_i curves, the use of apparent photosynthetic parameters is not adequate anymore and leads to underestimation of the degree of CO_2 fertilization by models without g_m.

The variations of R for different combinations of PAR and temperature shown in Figure 4.2 do not necessarily reflect how mesophyll diffusion affects the degree of CO_2

fertilization under different environmental conditions. They only demonstrate the consequences of not representing this process explicitly in models.

The terrestrial biosphere may be more CO_2-limited and more responsive to increased atmospheric CO_2 concentrations than global carbon cycle models have been suggesting. These models may have underestimated a cumulative 113 to 148 Pg C in global GPP since the Industrial Revolution. This magnitude of underestimation is equivalent to the total gross photosynthesis by the global terrestrial biosphere in one year (Beer et al. 2010; Welp et al. 2011) or to the entire global fossil CO_2 emissions from the Industrial Revolution to the mid-1970s (Boden et al. 2010). Applications of these models in coupled carbon-climate simulations will overestimate the growth of atmospheric CO_2 concentrations due to fossil fuel emissions. To adequately predict long-term effects of anthropogenic emissions and carbon-climate interactions, carbon cycle models should explicitly consider mesophyll resistance to CO_2 diffusion.

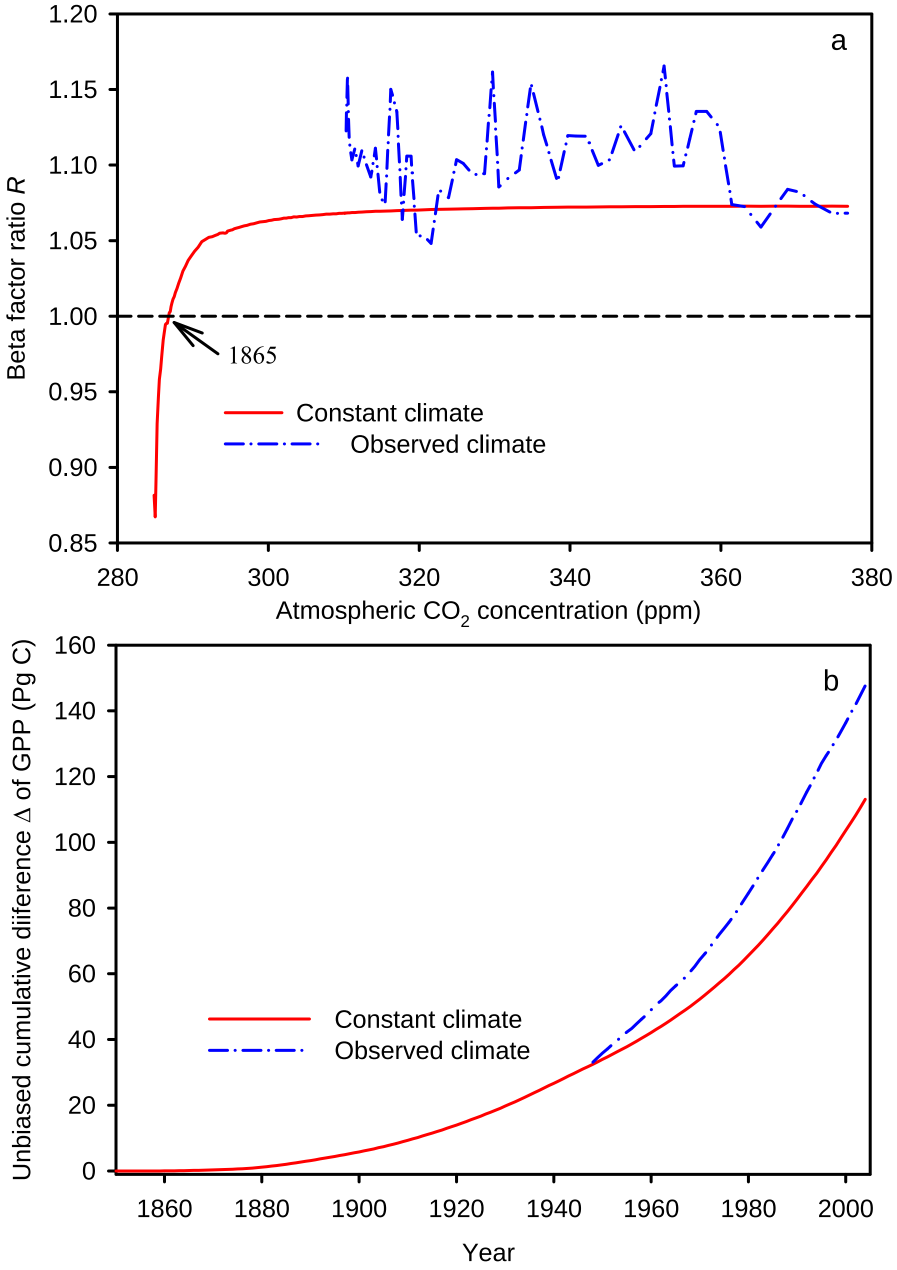

Figure 4.1. The beta factor ratio R[*](Panel a) and the unbiased cumulative difference Δ[†] (Panel b) of global annual gross primary production (GPP) calculated by CLM4a with and without mesophyll conductance as a function of atmospheric CO_2 concentrations (Panel a) and year (Panel b), respectively.

The baseline year is 1850 with an atmospheric CO_2 concentration of 285 ppm and is the same for both R and Δ and for both the constant and observed climate simulations. Since the observed climate is available only after 1948, Δ for the observed climate simulations is extended from 1948 to 1850 with results from the constant climate simulations of the same period, explaining the initial overlap in Δ for the constant and observed climate runs.

[*] Refer to Equation 4.1.

[†] Refer to Equation 4.2.

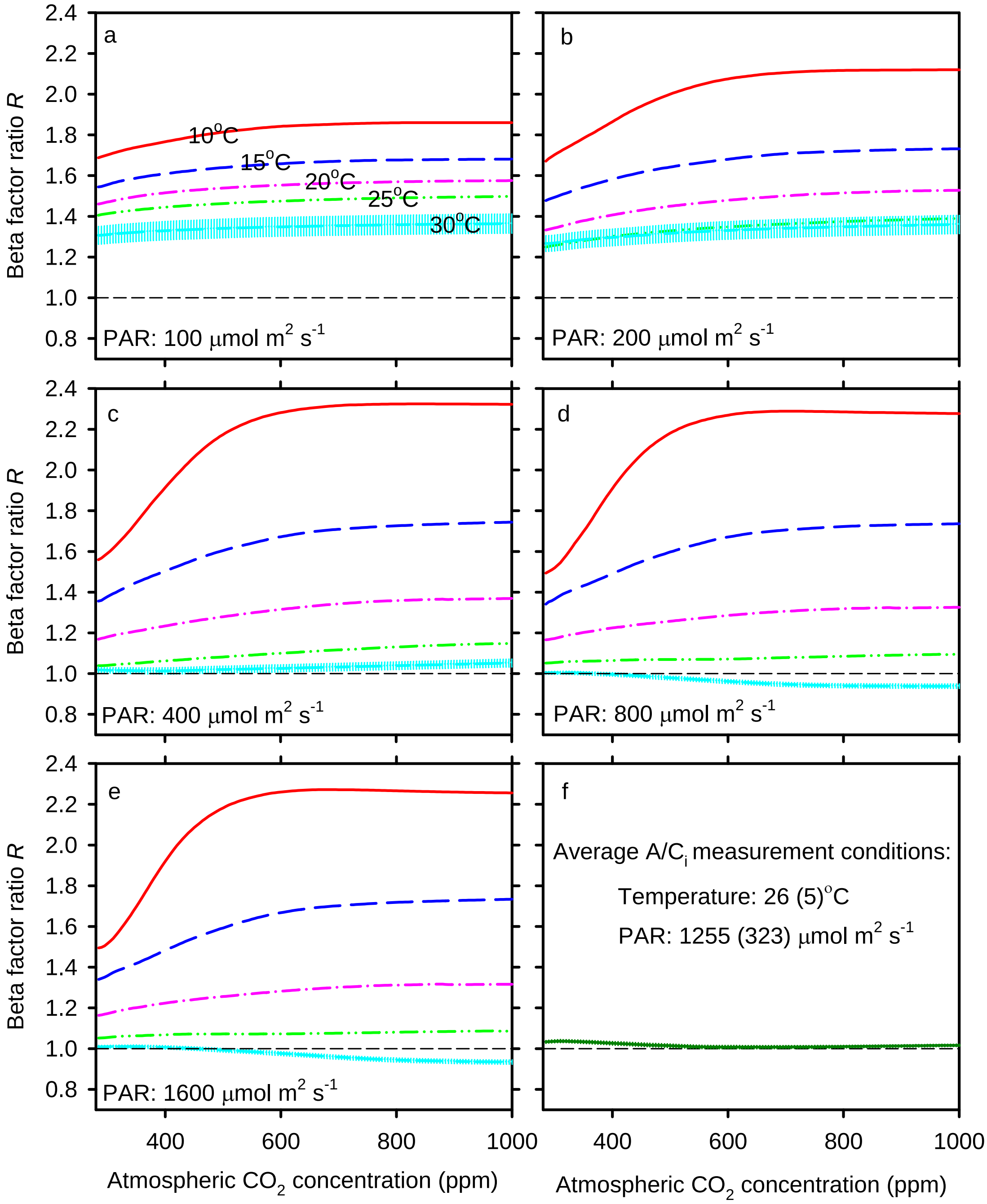

Figure 4.2. The beta factor ratio R of leaf net photosynthetic rate calculated by the FvCB model with and without extension of a mesophyll conductance as a function of ambient CO_2 concentrations.

The baseline ambient CO_2 concentration is 285 ppm. Each curve in each plot represents an average of over 1000 *R*-ratio curves. Calculations are done at 25 combinations of 5 levels of phtosynthetically active radiation (PAR): 100 (a), 200 (b), 400 (c), 800 (d) and 1600 μmol m^{-2} s^{-1} (e) and 5 levels of temperature (10, 15, 20, 25 and 30^{o}C). Calculations are also done at the original leaf gas exchange (A/C_i) measurement conditions which vary somewhat from measurement to measurement (f). The averaged PAR for the leaf gas exchange measurements is 1255 ± 323 μmol m^{-2} s^{-1} and the average temperature is 26 ± 5^{o}C. The 95% confidence interval is shown for the mean *R*-ratio curve at 30^{o}C (a-e) and at the measurement conditions (f, although barely seen due to a large volume of samples).

Chapter 5: A numerical issue in calculating the coupled carbon and water fluxes in a climate model[1]

5.1. ABSTRACT

The Community Land Model (CLM) uses a fixed-point iteration approach to solve the coupled photosynthesis and stomatal conductance model (A– g_s). Here we demonstrate that this approach does not converge in its iterative calculation of gross primary production (GPP) and transpiration in large portions of land surface, because the coupled A– g_s model does not always comply with a condition (the fixed-point theorem) required by the fixed-point approach for convergence. This iteration fails more frequently in some regions of the world than in others, leading to regionally varying uncertainty and global biases in the estimated carbon and water fluxes. Moreover, CLM applies an artificial constraint to the water vapor pressure of canopy air in its calculations of A– g_s, with an intention to prevent the 'numerical instability' arising from the fixed-point approach. Our results show that this constraint reduces but does not prevent the occurrence of non-convergence. Since this constraint is artificial, it can bias GPP and transpiration simulations. We then propose a Newton-Raphson iteration scheme to replace the fixed-point approach and show that this new approach can ensure convergence, does not require an artificial constraint on the atmospheric water vapor pressure, and is computationally efficient. On the other hand, the default fixed-point treatment in CLM leads to a ~2.7 Pg C yr^{-1} overestimation of GPP globally but with much higher regional biases (~27%). We thus suggest that the current fixed-point

---

[1] Substantial portions of this chapter were previously published in Sun, Y., L. Gu, and R. E. Dickinson, 2012a: A numerical issue in calculating the coupled carbon and water fluxes in a climate model. *J. Geophys. Res.*, **117**, D22103, doi:10.1029/2012JD018059. The References section contains full citations for all articles referenced here.

treatment in CLM be replaced with the Newton-Raphson approach and that the artificial constraint on the atmospheric water vapor pressure be removed.

5.2. INTRODUCTION

Climate models are now used to predict future oceanic and terrestrial carbon storage and hence how much will remain in the atmosphere and contribute to global warming (e.g., Dickinson 2012; Friedlingstein et al. 2006; Fung et al. 2005; Sarmiento et al. 2010). Carbon enters the terrestrial ecosystem through leaf stomata, which also transpire water extracted from soil. Therefore, a coupled photosynthesis and stomatal conductance (inverse of stomatal resistance) model is often used within a general land surface modeling framework to simulate terrestrial gross primary production (GPP) and transpiration at various time and spatial scales (Sellers et al. 1996; Dai et al. 2004; Bonan et al. 2011). GPP is the initial step of terrestrial carbon cycling (Beer et al. 2010; Zhao and Running 2010). It fuels the growth of plants, which in turn provide organic matter to soil (Dickinson 2012). Transpiration is a key component of evapotranspiration (ET) that by balancing absorbed solar radiation determines land surface temperature and other climate features (Dickinson et al. 2002). Thus a robust solution of the coupled photosynthesis (A) and stomatal conductance (g_s) process (denoted as $A – g_s$) is needed for accurate predictions of terrestrial carbon and water fluxes in climate models.

A widely used framework of the coupled process of the CO_2 and water vapor flow through the stomata was first implemented by Collatz et al. (1991), a variant version of which now is a component of the Community Land Model (CLM) (Oleson et al. 2010). This $A – g_s$ model encompasses a suite of nonlinear equations that in general must be solved iteratively, although under certain simplified conditions, analytical solutions are possible (Baldocchi 1994).

Various iteration methods are available for solving such nonlinear equations, with their own strengths and limitations for specific applications. Thus, it is of particular importance to choose an appropriate iteration scheme when it is applied for global simulations. We emphasize this point for a couple of reasons. First, in a global modeling framework, there are 10^3-10^6 land grids (depending on the simulation resolution), each of which can consist of mixed patches of various plant types that are forced by different environmental conditions. These vegetation and climatic conditions in turn strongly affect the behavior of the nonlinear equations involved and therefore the validity of their numerical treatment. Second, iterative calculations must be computationally inexpensive for global applications. However, we are not aware of any previous effort to examine these numerical issues in depth for the A– g_s model, although the coupling between carbon and water vapor fluxes is at the core of land surface modeling.

We have found that the iteration approach used in CLM to solve the A– g_s model (and likely other such models of similar heritage) does not converge, hence introduces errors to the modeled carbon and water fluxes. We examine why this non-convergence occurs and introduce a more robust iteration framework to remedy this numerical problem. This new approach is based on an in-depth analysis of the numerical behavior of the A– g_s model. We demonstrate that our new treatment corrects substantial biases in the GPP and transpiration simulated by the latest released version of CLM, i.e., CLM4 (Oleson et al. 2010).

5.3. THE NUMERICAL TREATMENT FOR THE COUPLED PHOTOSYNTHESIS-STOMATAL CONDUCTANCE MODEL IN CLM4 PRODUCES LARGE REGIONS OF NON-CONVERGENCES

5.3.1. Characteristics of iterative solutions for the coupled nonlinear equations in CLM4

The carbon and water fluxes must be determined together with the constraint of canopy energy conservation, because the key parameters for photosynthesis and evapotranspiration (ET) strongly depend on leaf temperature. Models use iterative approaches to directly solve for two unknowns: leaf temperature (T_v) and the CO_2 partial pressure inside the leaf intercellular space (c_i). Other variables are calculated as functions of these two unknowns either during the iterative procedure or after the two unknowns have been solved.

Consider two equations with the variables x and y to be determined, i.e., $f(x,y) = 0$ and $g(x,y) = 0$. In particular, f is the $A\text{–} g_s$ model with x as c_i, and g is the leaf temperature calculation with y as T_v. Currently in CLM4, these two equations are solved by nesting the $A\text{–} g_s$ model into the T_v calculation, where the outer loop solves $g(x,y) = 0$ for y assuming a fixed x, while the inner loop solves $f(x,y) = 0$ for x keeping y fixed. Furthermore, the two loops use different iteration schemes, i.e., the inner loop f uses a fixed-point (FP) iteration approach independent of the outer loop whereas the outer loop g uses a Newton-Raphson iteration inherited from the earlier Biosphere-Atmosphere Transfer Scheme (BATS), e.g., Equation 84 in Dickinson et al. (1993) or Equation 5.116 in Oleson et al. (2010). Here we focus on the inner loop only, since the fixed-point iteration can fail to attain a solution for the $A\text{–} g_s$ model and hence simulate carbon and water fluxes with questionable accuracy.

5.3.2. Formulations and numerical implementations of the A– g_s model in CLM4

The CLM4 uses a modified version of the Farquhar model (Farquhar et al. 1980; Collatz et al. 1991) to calculate photosynthesis for C_3 plants and the Collatz et al. (1992) model for C_4 plants. The photosynthesis A is expressed as a function of c_i as follows:

$$A(c_i) = \min\{w_c(c_i), w_j(c_i), w_e(c_i)\}, \tag{5.1}$$

where w_c is the Rubisco-limited carboxylation rate; w_j is the light- or RuBP regeneration-limited carboxylation rate; and w_e is the export-limited (C_3) or the CO_2-limited rate of carboxylation (C_4). For simplicity, w_c, w_j and w_e and thus A are all shown as functions of c_i only; but they actually depend on a suite of parameters and environmental variables as well. For example, w_c is determined by the maximum Rubisco carboxylation rate V_{cmax}, a key photosynthetic parameter that is limited by soil dryness β_t, where $0 \le \beta_t \le 1$ (see Equation 8.13 in Oleson et al. 2010). Detailed formulations of w_c, w_j and w_e are documented elsewhere (Oleson et al. 2010); here we only list key equations of direct relevance to our study.

The CLM4 applies the Ball-Berry model (Ball et al. 1987; Collatz et al. 1991) to calculate stomatal resistance r_s, which requires A as an input. Through incorporating CO_2 diffusion via leaf boundary layer, r_s is solved with the following quadratic equation (also Equation 8.27 in Oleson et al. 2010),

$$\left[\frac{m \cdot A \cdot P_{atm} \cdot e'_a}{c_s \cdot e_i} + b\right] \cdot r_s(A)^2 + \left[\frac{m \cdot A \cdot P_{atm} \cdot r_b}{c_s} + b \cdot r_b - 1\right] \cdot r_s(A) - r_b = 0. \tag{5.2}$$

Here, m is a plant functional type (PFT)-dependent parameter; P_{atm} the atmospheric pressure; c_s the CO_2 partial pressure at the leaf surface; b the minimum stomatal conductance; r_b the leaf boundary layer resistance; e_i the saturation vapor pressure inside the leaf; e'_a the constrained water vapor pressure of canopy air. We emphasize that CLM4 imposes an arbitrary lower limit on the parameter e'_a, which strongly affects the effectiveness of the fixed-point iteration (Section 5.4). In CLM4, e'_a is determined by

$$e'_a = \max(\min(e_a, e_i), \alpha \cdot e_i)\,, \tag{5.3}$$

where e_a is the actual water vapor pressure of canopy air; α(= 0.25 for C_3 or = 0.4 for C_4 plants) is an arbitrary coefficient for the constraint on water vapor pressure enforced by CLM4. The rationale for this constraint is to 'prevent numerical instability in the iterative stomatal resistance calculation' (pp. 172, Oleson et al. 2010). The lower limit is higher for C_4 plants 'because C_4 plants are not as sensitive to vapor pressure as C_3 plants' (pp. 172, Oleson et al. 2010). Later we examine the consequences of this artificial constraint for the calculated carbon and water fluxes when fixed-point iteration is used.

The diffusion of CO_2 through stomata forms the final independent equation needed to close the coupled A–g_s model:

$$c_i = c_s - 1.65 \cdot r_s(A) \cdot P_{atm} \cdot A(c_i)\,. \tag{5.4}$$

The set of Equations 5.1, 5.2, and 5.4 is iterated over the variable c_i given an initial guess, that is, $c_i = 0.7 \cdot c_a$ for C_3 or $c_i = 0.4 \cdot c_a$ for C_4, where c_a is the atmospheric CO_2 partial pressure (Oleson et al. 2010). This current procedure in CLM4 is a typical implementation of the fixed-point iteration (details to be given in Section 5.4). Its iteration of c_i proceeds three times, without checking whether a convergence is achieved.

5.3.3. Demonstration of the numerical problems in the calculated carbon and water fluxes with global simulations

Here we use global simulations to demonstrate that the fixed-point treatment for the A– g_s in the default CLM4 produces large regions of non-convergence of GPP and transpiration over the global land surface. This diagnosis strategy is simple: we increased the maximum number of iterations N from 3 to 20 with a one-step increment for each simulation while keeping the fixed-point configurations as default in CLM4 (denoted as FP_wC, Table 5.1). Simulations were performed from the year 1948 to 2004 in the offline mode driven by the atmospheric forcing data of Qian et al. (2006). The analyses were conducted for boreal summer, i.e., JJA (note this simulation and analysis protocol was also applied to the simulations with our proposed new iteration approach in Section 5.5). For clarity, only results for the year 1948 are described here; results for other years are similar.

Figure 5.1a shows clear differences in the JJA-mean GPP over North America and Eurasian between the default 3-step treatment and that with an additional iteration. This inter-step difference is pronounced in western United States, where a ~200 g C m^{-2} yr^{-1} (~20% if using the default 3-step simulation as reference, also see Table 5.2) difference in GPP is observed. Evidently, the fixed-point iteration suffers from widespread non-convergence since the difference between two adjacent iteration steps would be minimal if the iterative calculation had converged. Furthermore, this failure of convergence is not a matter of the maximum number of iteration steps N, because the difference in GPP between two consecutive steps does not attenuate with increasing number of iterations in general (Figure 5.1b-g and Table 5.2). Instead of convergence, a regular oscillation pattern exists in the modeled GPP with fixed-point iteration (Figure 5.1b-g). Similar patterns are also found in the simulated transpiration (results not shown).

As stated above, CLM4 imposes a prior constraint on the water vapor pressure of canopy air, which artificially modifies the environmental conditions and hence their impact on the A– g_s calculation. We designed another set of simulation experiments (denoted as FP_woC, Table 5.1) to investigate the effect of this constraint on iterative calculations of GPP and transpiration. In these simulations, the lower limit on e'_a was removed such that Equation 5.3 turns into $e'_a = \min(e_a, e_i)$, while all other formulations and the fixed-point approach remain unchanged from the default.

Figure 5.2 shows that the removal of the constraint on e'_a substantially degrades the convergence of simulated GPP and transpiration. Compared to Figure 5.1a, more regions show non-convergence of GPP, e.g., eastern Amazon, southern Africa, Australia, and a large portion of Eurasia (Figure 5.2b). In western US, the magnitude of disparity between the 3th and 4th iteration is larger than that with this constraint. A concomitant degradation is also found in canopy transpiration, because of its strong coupling with photosynthesis (Figure 5.2b).

These findings demonstrate that the fixed-point iteration approach employed by the CLM4 fails to solve the coupled $A - g_s$ model for substantial regions of the land surface on Earth.

5.4. WHY THE ITERATION APPROACH IN CLM4 FAILS: A MATHEMATICAL PERSPECTIVE

5.4.1. The theorem of fixed-point iteration

The fixed-point iteration is the simplest numerical approach to solve nonlinear equations. Any equation can be expressed in the fixed-point form as,

$$x = h(x). \tag{5.5}$$

The root of Equation 5.5 is commonly called the fixed point of the iterative function $h(x)$. This form is appealing because it allows a very straightforward iterative procedure:

$$x_{k+1} = h(x_k), k = 0, 1, 2, 3 \cdots, n. \tag{5.6}$$

Geometrically, the root of Equation 5.5 is the intersection between the diagonal line $y = x$ and the curve $y = h(x)$ in a Cartesian coordinate system. Although the fixed-point iteration is easy to apply, its success critically depends on the shape of $h(x)$. The fixed-point iteration does not converge if the absolute value of the derivative of $h(x)$ with respect to x is greater than one, i.e., $|h'(x)| > 1$, over the domain that is around the root of x. This is the well-known fixed-point theorem and its violation leads to failure of convergence (Burden and Faires 2011).

5.4.2. Numerical behaviors of the fixed-point solution to the *A*– g_s model

Equation 5.4 as implemented in CLM4 is a typical form of fixed-point iteration, where c_i is considered as the input *x* and the right-hand side represents the iterative function *h*:

$$h(x = c_i) = c_s - 1.65 \cdot r_s[A(c_i)] \cdot P_{atm} \cdot A(c_i)\,. \qquad (5.7)$$

Whether Equation 5.7 can be solved effectively in a global simulation using the fixed-point approach depends on its mathematical properties, as determined by calculating *A* and r_s from Equations 5.1-5.2, hence $h(c_i)$ from Equation 5.7 as a function of c_i, and examining the shape of the resulting $h(c_i)$ curve. This process is different from the iterative calculation of c_i in that it does not repeat the iterative loop. It is equivalent to examining how $h(x)$ changes with *x* in Equation 5.5. Only the photosynthesis model for C_3 plants is examined here since they are the dominant species in global vegetation types.

Figure 5.3 shows the geometrical shape of $h(c_i)$ and the effect of model parameters e'_a on the iterative calculation of c_i. A couple of common characteristics of $h(c_i)$ curves are seen. First, the $h(c_i)$ curve is flat when c_i is below the CO_2 compensation point Γ_*. This occurs because in CLM4, w_c and w_j and hence *A* are set to be zero if c_i is less than Γ_* (for details, see *Oleson et al.*, 2010). As a consequence, $h(c_i) = c_a$ (note both c_i and $h(c_i)$ are confined to the range of 0 to c_a) as shown in Figure 5.3a. Second, as c_i increases from Γ_*, $h(c_i)$ decreases initially with a very steep slope with $|h'(c_i)| > 1$; only as c_i further increases does the slope become gentler ($|h'(c_i)| < 1$). The specific geometry of the $h(c_i)$ curve depends on model parameters in Equations 5.1-5.2. As one parameter varies, the absolute value of the derivative of $h(c_i)$ can equal or exceed one and so violate the fixed-point theorem.

Here we show that the shape of $h(c_i)$ is very sensitive to the constrained water vapor pressure of canopy air e'_a and hence it is the most important parameter determining whether the fixed-point approach converges. As e'_a decreases, the fixed-point iteration switches from convergence to non-convergence. The transition boundary occurs at $h'(c_i) = -1$ with c_i at the root c_i* (Figure 5.3a). Figure 5.3a shows four typical convergence scenarios for fixed-point iteration given an identical initial guess $c_{i,1}$ (= $0.7 \cdot c_a$, i.e., the CLM4 setting for C_3 physiology; the subscript number represents the iteration step). Scenario I (Figure 5.3b) demonstrates the effectiveness of the fixed-point iteration when it converges: the solution c_i* is achieved within 3 iteration steps because $c_{i,\mathrm{k}}$ at all iteration steps fall in the region of the $h(c_i)$ curve where $|h'(c_i)| <1$. Scenario II (Figure 5.3c) also converges with the fixed-point approach, but it requires 10 steps to approach the root. This slower convergence rate is a consequence of a relatively large $|h'(c_i)|$ compared to that of Scenario I (i.e., closer to 1). Scenario III (Figure 5.3d) fails to converge at the root, because the iterative $c_{i,\mathrm{k}}$ periodically falls onto the zone with $|h'(c_i)| >1$, i.e., the initial guess of $c_{i,1}$ results in a value of $c_{i,2}$ that falls onto the "steep declining zone" of $h(c_i)$; then $c_{i,3}$ is a little bit larger than $c_{i,1}$ and leads to an $c_{i,4}$ on the same part of $h(c_i)$ as $c_{i,2}$. The c_i from the 3rd step onward oscillates between the values of $c_{i,3}$ and $c_{i,4}$. As a consequence, consecutive values of c_i fluctuate around the root but never approach it, regardless of the maximum iteration steps N. Scenario IV (Figure 5.3e) is similar to Scenario III, but with the magnitude of the oscillation of c_i larger than alternating between 0 and c_a. Since $c_{i,2}$ directly falls below Γ_* (thus A is set to be zero), and then $c_{i,3}$ equals to c_a yielding $c_{i,4}$ to be zero. Again, from this point, the iteration circles around but never reaches the root. These trajectories of c_i with iteration steps shown in Figure 5.3d and 3e illustrate the consequences of the violation of the fixed-point theorem.

Figure 5.4 shows that other parameters also affect the shape of $h(c_i)$ curves, but with a lesser degree of sensitivity by individually varying the maximum Rubisco carboxylation rate V_{cmax}, the absorbed photosynthetically active radiation ϕ, the composite Michaelis-Menten constant K_{co} = ($K_c \cdot (1 + O / K_o)$), and the CO_2 compensation point Γ_*, while keeping unchanged from boundary curve in Figure 5.3a for all other input variables and parameters. Figure 5.4a shows that a larger V_{cmax} and Figure 5.4c that a smaller K_{co} produce a steeper $h(c_i)$ curve and thus failure of the convergence of the fixed-point iteration. When ϕ is over 500 μmol photon m^{-2} s^{-1}, the geometry of $h(c_i)$ is not sensitive to its variation, and hence ϕ has less impact on convergence (Figure 5.4b). The Γ_* modifies the $h(c_i)$ shape in a different way (Figure 5.4d). It not only affects the steepness of the $h(c_i)$ curve, but also alters the width of the "flat zone" of the $h(c_i)$ curve. As Γ_* increases, the derivative $|h'(c_i)|$ increases and the curve moves rightward and gradually enters the zone with $|h'(c_i)|>1$, leading to the non-convergence of c_i.

To summarize, the nonlinear equation represented by the A– g_s model (C_3) does not always comply with the conditions required to ensure the convergence of the fixed-point iteration. The shape of the equation depends on the values of parameters and input environmental variables. In particular, the parameter e'_a matters most for the effectiveness of the fixed-point approach in finding the root of c_i, since c_i is sensitive to r_s (Equation 5.7), which in turn is quite sensitive to variations of e'_a. Furthermore, the e'_a has larger variations (strong diurnal cycle and seasonal variation) than other parameters involved, thus it contributes most to the numerical failure of fixed-point iteration in solving the A– g_s model.

5.4.3. The underlying causes for the spatial variation of the failure of fixed-point iteration in global simulations

Across the land of the globe, the failure of fixed-point iteration does not occur randomly (Figure 5.1 and 2). The mathematical investigation of the shape of $h(c_i)$ provides some insights to the physical causes of the non-convergence of the fixed-point approach in simulating carbon and water fluxes. It can be largely attributed to the joint effects of the relative humidity (RH) and air temperature in determining the water vapor pressure of canopy air e_a (Figure 5.5). We can see that the non-convergence regions in Figure 5.2, e.g., the western US, eastern Amazon, southern Africa, northern Australia, and Eurasia, have a low RH (generally below 50%), which in turn decreases e_a. Northern Africa has the lowest RH but does not show the non-convergence problem, because the associated high air temperature and thus high saturation water vapor pressure offset the effect of low e_a on e'_a and the convergence of iteration. In addition, the sparse vegetation leads to an extremely low productivity in this area. Apart from northern Africa, the spatial distribution of the non-convergence (Figure 5.2) has a good correspondence with that of RH (Figure 5.5). Thus it is primarily RH that determines why the fixed-point scheme works for some grids but not for others.

This high sensitivity of $h(c_i)$ to e'_a also explains why the application of the prior constraint can improve the convergence of the fixed-point approach (see the difference between Figure 5.1 and 5.2): by maintaining a higher water vapor pressure it reduces the steepness of the curve $h(c_i)$ (Figure 5.3) and makes the iteration more likely to satisfy the fixed-point theorem.

5.5. AN ALTERNATIVE ITERATION FRAMEWORK: THE NEWTON-RAPHSON APPROACH

The Newton-Raphson (NR) iteration scheme has been applied in climate models, for example, to calculate leaf temperature from energy balance equations (Oleson et al. 2010) as mentioned earlier and to treat the complicated cloud microphysics (Neale et al. 2010). Here we apply this strategy to solve the coupled $A-g_s$ model. The standard form of Newton-Raphson iteration is (Burden and Faires 2011)

$$x_{k+1} = x_k - j(x_k)/j'(x_k), k = 0, 1, 2, 3\cdots, n. \tag{5.8}$$

Again x_k and x_{k+1} are the iterated variable at the k^{th} and $k+1^{\text{th}}$ step; $j(x)$ is the iteration function to be zeroed; and $j'(x)$ is the derivative of $j(x)$ with respect to x. Starting with an initial guess, the Newton-Raphson scheme approximates $j(x)$ by its tangent line, the slope of which is $j'(x)$. The x-intercept of the tangent line is taken as the guess of the root for the next iteration step. The iteration converges if the difference between two successive steps, i.e., x_k and x_{k+1}, is smaller than a prescribed threshold that is close to zero. The converged point is the root of the nonlinear equation. Geometrically, the root of $j(x)$ is the intersection between $y = 0$ and $y = j(x)$. Unlike the fixed-point iteration, the derivative $|j'(x)|$ does not need to be less than 1 for the Newton-Raphson approach to achieve convergence.

To apply this new scheme to the coupled $A- g_s$ model, we reorganize Equation 5.7 to form the iteration function

$$j(x=c_i)=h(c_i)-c_i. \tag{5.9}$$

For global model simulations, calculation of $j'(x)$ can be computationally expensive; here we use a simple and typical numerical approximation (e.g., Burden and Faires 2011),

$$j'(x_k)=[j(x_k+j(x_k))-j(x_k)]/j(x_k). \tag{5.10}$$

The application of the Newton-Raphson scheme using this approximation proceeds as follows:

(a) Assign an initial guess of c_i;

(b) Calculate $A(c_i)$ from c_i according to the photosynthesis model Equation 5.1;

(c) Calculate $r_s(A)$ according to Equation 5.2 from the A;

(d) Calculate the function $j(c_i)$ from c_i, $A(c_i)$ and $r_s(A)$ according to Equation 5.9;

(e) Calculate an intermediate $A_1(c_i + j(c_i))$ according to the photosynthesis model Equation 5.1;

(f) Calculate an intermediate $r_{s1}(A_1)$ according to Equation 5.2;

(g) Calculate an intermediate $j_1(c_i+ j(c_i))$ from $c_i+ j(c_i)$, and estimated $A_1(c_i + j(c_i))$ and $r_{s1}(A_1)$ according to Equation 5.9;

(h) Obtain the approximate derivative $j'(c_i)$ according to Equation 5.10, where $j_1(c_i + j(c_i))$ and $j(c_i)$ correspond to the two terms in the numerator while the latter also serves as the denominator;

(i) Update c_i using Equation 5.8;

(j) Exit the iterative loop and determine the final A and r_s if the difference of c_i between two successive steps satisfies a given convergence criterion or if the current iteration step exceeds the specified maximum number N; otherwise, repeat (b) – (i).

The convergence criterion of c_i is set here to be 0.001 Pa and the upper limit of iteration is N = 20. As demonstrated later, the Newton-Raphson scheme we used here rarely reaches this upper limit.

In order to investigate the effectiveness of this new approach for the calculation of the $A\text{–}g_s$ model, we first explored the mathematical properties of $j(c_i)$ curves in a similar manner to $h(c_i)$: introducing variations to the $j(c_i)$ curve through systematically changing e'_a. Figure 5.6 demonstrates that this new approach has two benefits. First, for the two convergence scenarios illustrated for the fixed-point iteration (Figure 5.3b and c), the Newton-Raphson scheme has a much faster convergence rate, with its solution attained at the 2nd (Figure 5.6b) and 3rd (Figure 5.6c) iteration step for Scenario I and II, respectively. Second, this new scheme turns the non-convergence scenarios of fixed-point (Figure 5.3d and e) into convergence cases (Figure 5.6d and e) within 5 and 7 iteration steps, respectively. Evidently, the proposed new scheme is a more effective way for solving the nonlinear equations of the $A\text{–}g_s$ model, with both accuracy (or validity) and computational efficiency guaranteed. Its "validity" stems from the absence of a strict requirement for the derivative of $j(c_i)$. So the convergence does not depend on the model parameters. Its "efficiency" is a consequence of the mathematical properties of $j(c_i)$, i.e., the value for c_i at a following step always moves towards the root (Figure 5.6e). All comparisons here used the same initial guess as the fixed-point approach to eliminate the possible contribution from "a better initial guess".

5.6. THE EFFECTIVENESS OF THE NEWTON-RAPHSON ITERATION SCHEME FOR GLOBAL SIMULATIONS

We performed two sets of global simulations with a version of CLM4 that implements the new Newton-Raphson iteration approach: NR_wC, a simulation that keeps the constraint on e'_a present, and NR_woC that removes this constraint (Table 5.1). These experiments follow the same protocols as FP_wC. Again, the year 1948 is presented only for demonstrating the superiority of this new iteration scheme; the historical simulations show similar. Here we used the simulations at the 20th step as reference since the prescribed maximum number of iteration is 20.

We found that, with the artificial constraint, the simulated GPP is perfectly identical between the 19th and 20th steps (Figure 5.7a). In the western US, the convergence is almost achieved by the 6th step (Figure 5.7c). Further, after removing the constraint, the Newton-Raphson scheme can still ensure the convergence of GPP and transpiration. Figure 5.8 shows that with the removal of the constraint, the deviation of calculated GPP and transpiration from the reference attenuates with an increasing number of iterations. For example, GPP converges within 19 steps, while no visible disparities of transpiration from the reference are observed by the 15th step. Nevertheless the convergence speed is slower, compared to the simulations with the constraint. We found that setting an initial guess of c_i slightly larger than the CO_2 compensation point Γ_* can increase the convergence rate, thus improve the iteration efficiency. This is because the Newton-Raphson approach uses gradient for calculations at the following iteration step, and thus favors a larger derivative (or steeper slope) of the iteration function $j(c_i)$.

5.7. COMPARISON BETWEEN THE FIXED-POINT AND NEWTON-RAPHSON ITERATION APPROACHES

We estimated the biases in modeled GPP and transpiration arising from the use of the fixed-point iteration scheme and the associated artificial constraint on e'_a. This is achieved through comparing the default CLM4 simulation with the version of CLM4 that implements the Newton-Raphson scheme and discards the constraint. Figure 5.9 shows that across the globe the default numerical treatment predominantly overestimates GPP and transpiration although over Mexico and along the southern-central edge of the Sahara, GPP and transpiration tend to be underestimated. Globally, a positive bias of ~2.7 Pg C yr^{-1} in the simulated GPP is found. The western US has the most noticeable non-convergence problem, with 27% overestimation of GPP and 46% for transpiration (Table 5.2). Further, such overestimation can affect the energy portioning and hence bias the calculation of sensible heat flux (Table 5.2).

The new approach proposed in this study not only remedies the non-convergence problems, but also guarantees the computational efficiency for the convergent grids in the fixed-point framework. Figure 5.10a shows that the Newton-Raphson approach works equally well as the fixed-point scheme at the 3rd iteration step when the latter converges, a consequence of it sharing similar built-in mathematical features as the fixed-point scheme. However, the Newton-Raphson approach works under conditions that lead to failure of the fixed-point iteration (Figure 5.10b). Further, it is computationally more efficient than the fixed-point scheme. Figure 5.11 shows the fraction of non-convergent land grids as a function of iteration steps. It shows that ~40% of grids cannot converge regardless of the number of iteration steps if fixed-point approach is used and the artificial constraint on e'_a is removed. In contrast, over 90% of the global land grids by the 3rd step and almost all by 9th step can converge with the Newton-Raphson scheme, indicating its superiority.

5.8. DISCUSSION

Our results show that the fixed-point scheme with three iteration steps in the current CLM4 cannot guarantee convergence of the coupled A– g_s model. This approach fails more frequently in some regions of the world (e.g., the western US) than in others, leading to regionally varying uncertainty and global biases in estimated GPP and transpiration.

A mathematical examination reveals that the non-convergence arises because the behavior of the iterative function $h(x)$ in CLM4 cannot always satisfy a strict mathematical condition, i.e., the fixed-point theorem. In particular, the effectiveness of the fixed-point iteration is quite sensitive to e'_a, which modifies the shape or the derivative of $h(x)$ and therefore affects whether or not the fixed-point theorem is violated. The e'_a in turn is strongly affected by RH, thus increasing air dryness relative to saturation vapor pressure may shift the $h(x)$ of some grids from convergence to non-convergence. A number of previous studies have reported that more severe and frequent drought may occur in the future (Sitch et al. 2010; Solomon et al. 2009), which if so may lead to a spatial expansion of the failure of the fixed-point iteration in a changing climate and so add more bias to the existing uncertainties for model predictions. Hence, the default fixed-point treatment in CLM4 is not adequate for reliable simulations of carbon and water fluxes and may jeopardize the future projections of flux variables for regional or global applications.

The application of the prior constraint on e'_a can reduce but not eliminate the numerical problems caused by the fixed-point method. Essentially, this constraint sets an artificial lower limit to the atmospheric water vapor pressure deficit (VPD), one of the most important variables to which stomata respond, particularly under drought conditions (Gu et al. 2006). It is known that the current CLM performs poorly in simulating ecosystem responses to drought (Sakaguchi et al. 2011). This artificial constraint may have contributed to this poor performance. The application of this constraint stems from an attempt to fix the potential failure of the $A - g_s$ calculation, viewed as 'numerical instability' by Oleson et al. (2010). However, our analysis shows that this 'instability' is not inherent in the coupled $A - g_s$ model but rather is a consequence of applying the fixed-point method under conditions where the mathematical requirement for convergence is not satisfied. Hence, the constraint on water vapor can implicitly turn an originally non-convergent case into a convergent one by reducing the magnitude of $|h'(x)|$, leading to conditions that satisfy the fixed-point theorem (Figure 5.3 and 5.12). For example, non-convergent grids emerge in the Amazon, southern Africa, and Australia with absence of this constraint, as seen in the differences between Figure 5.1 and Figure 5.2. This "quick fix" of convergence may degrade the CLM performance under water stress, as it artificially modifies the air dryness. Hence, the bias arising from the non-convergence may be small under normal conditions, but may be exacerbated during drought periods.

This study is based on the latest released version of CLM4 (Oleson et al. 2010), but does not consider the revisions proposed by Bonan et al. (2011, 2012). To our knowledge, these unreleased updates did not change the iteration scheme and thus did not fix the numerical issue reported in our study. The non-convergence problem exists regardless of the new updates, since the fixed-point theorem is a strict mathematical restriction, which works only under certain conditions. Given the large variations of the parameters and forcing variables involved in the coupled carbon-water flux model and thus the geometry of the iterative function, the fixed-point approach is not sufficient for convergence for global or regional applications at any time scales.

Our study shows that the Newton-Raphson approach can ensure the convergence of the coupled $A\text{–}\ g_s$ model and thus produce numerically accurate estimates of GPP and transpiration, since the condition for the Newton-Raphson approach to converge is much more relaxed as compared to the fixed-point. Further, this new scheme performs well even if the prior constraint on the atmospheric vapor pressure is removed, indicating its effectiveness under drought conditions (Figure 5.8), which could result in more frequent occurrences of non-convergence if fixed-point approach is otherwise used. This scheme is computationally efficient for global simulations: at the points where the fixed-point method succeeds, the Newton-Raphson iteration converges at a similar or even faster rate due to their similar built-in features; for those where the fixed-point fails, the convergence with the Newton-Raphson can generally be achieved within 10 steps although longer iterations may be needed for few isolated grids.

The Farquhar photosynthesis model is a change point model, i.e., with discontinuity point at the transition of c_i among w_c , w_j and w_e (Gu et al. 2010 and Equation 5.1). This has the potential to cause failures of any iterative approach, as such usually requires the iterative function and its derivative to be continuous near the root (Burden and Faires 2011). However, the convergence would not be affected as long as the root is not close to the change point. In all our simulations, we did not encounter any discontinuity problems. Bonan et al. (2011) has included the “co-limitation” treatment to smooth the change point (see their Table B1), which if accounted for should make the proposed Newton-Raphson method more effective.

Would changing the initial guess for c_i be a “simpler and quicker fix” for the non-convergence issue than a new iteration scheme? This strategy is ineffective as long as c_i

falls on the “steep declining zone” of $h(x)$, where the violation of fixed-point theorem occurs. On the other hand, tuning the initial guess may speed up the convergence rate of Newton-Raphson iteration if the new initialization happens to be close to the root. Speeding up of convergence can still be achieved if one locates the initial guess to be in the steep portion of the Newton–Raphson iteration function (Figure 5.6; e.g., with c_i just above the CO_2 compensation point) as the Newton-Raphson approach uses gradient to determine the next iteration step. These effects, however, would not occur to fixed-point iteration if the new initial guess is also on the “steep declining” portion of $h(x)$, even if it is close to the root.

For this present study we have not changed the double loop structure in the current CLM4 for solving leaf temperature T_v and carbon fluxes. The computational efficiency of CLM4 could be improved if this nested loop were replaced by simultaneously solving T_v and c_i through the Newton-Raphson approach. However, the substantial modification of the current CLM4 coding structure that would be required is beyond the scope of this present study. It is necessary to point out that the failure of convergence in the CLM4 is not caused by its nested loop structure, but rather by its use of the fixed-point iteration approach, since this approach is restricted by a mathematical theorem.

The results shown in this study are based on the year 1948. However, the spatial distribution of the bias caused by the fixed-point iteration and the superiority of the Newton-Raphson approach are quite persistent, i.e., independent of the specific year chosen for the demonstration purpose.

Different iterative methods are available for solving nonlinear equations. Each method has its strength and weakness and no method is universally valid and efficient. Thus, when choosing an iterative method to solve a given nonlinear equation, the numerical behavior of this nonlinear equation must be carefully analyzed so that an optimal method is selected. The fixed-point iteration has also been applied in other research areas, e.g., eddy covariance flux corrections (Aubinet et al. 2012), since it is the easiest and most straightforward way to be implemented. It is also possible that other land surface models may have employed a similar strategy to solve the coupled carbon and water flux model, since they share the same heritage as CLM. Our study appears to be the first attempt to discuss the numerical caveats of the fixed-point iteration in the context of land surface modeling, which could remind modelers to check the specific implementation of processes that require iteration, not only for CLM team, but also for other land surface modeling communities.

5.9. CONCLUSIONS

The CLM4 uses a fixed-point iteration scheme with three iterative steps to solve the coupled carbon and water flux model. This approach cannot guarantee convergence in the iterative calculation for GPP and transpiration. It fails more frequently in some regions of the world (e.g., the western US) than in others, leading to regionally varying uncertainty and global biases in estimated GPP and transpiration. The arbitrary constraint applied by CLM4 to the atmospheric water vapor pressure prior to the numerical implementation can partially cover the iteration problems of the fixed-point method; however, this is artificial and can cause biased estimates of carbon and water fluxes. Mathematically, we show that environmental factors modify the shape of the fixed-point iterative function and hence determine whether the conditions required for convergence (i.e. the fixed-point theorem) are satisfied. Because of this strong limitation, the fixed-point iteration scheme should not be used to solve the coupled carbon-water flux model, given the importance of this coupled model in land surface modeling. We propose a

Newton-Raphson approach to replace the default fixed-point scheme. Our results show that the new approach can ensure convergence and is computationally efficient. Further it does not require the artificial constraint to the atmospheric water vapor pressure. We find that the default CLM4 treatment leads to a ~2.7 Pg C yr^{-1} overestimation of GPP globally, with regional bias being up to 27%. We thus suggest that the current fixed-point treatment in CLM4 be replaced with the Newton-Raphson approach and that the artificial constraint on the atmospheric water vapor pressure be removed.

5.10. ACKNOWLEDGEMENTS

This study was carried out at University of Texas – Austin with support from National Science Foundation (ATM-0921898) and Department of Energy (DE-FG02-01ER63198), and also at Oak Ridge National Laboratory (ORNL). ORNL is managed by UT-Battelle, LLC, for the U.S. Department of Energy under contract DE-AC05-00OR22725.

Table 5.1. Summary of model simulations.

Simulation	**Description**
FP_wC	fixed-point scheme with the constraint on e'_a [*]
FP_woC	fixed-point scheme without the constraint on e'_a
NR_wC	Newton-Raphson scheme with the constraint on e'_a
NR_woC	Newton-Raphson scheme without the constraint on e'_a

[*] The default CLM4 scheme.

Table 5.2. Iteratively calculated JJA-mean GPP, transpiration, and sensible heat fluxes averaged for western United States[*] and for eastern Amazon[†].

Simulation	**Iteration Step**	**Western US**			**Eastern Amazon**		
		GPP	**Trans-piration**	**Sensible Heat**	**GPP**	**Trans-piration**	**Sensible Heat**
FP_wC	N3	993	22	83	2142	58	55
	N4	787	17	86	2140	58	55
	N19	987	22	83	2140	58	55
	N20	790	17	86	2140	58	55
FP_woC	N3	757	15	87	2169	57	56
	N4	1034	22	83	2066	55	57
	N19	770	15	87	2160	57	56
	N20	1029	22	83	2058	54	57
NR_wC	N19	830	18	85	2140	58	55
	N20	830	18	85	2140	58	55
NR_woC	N19	778	15	87	2062	54	57
	N20	778	15	87	2062	54	57

GPP is in g C m^{-2} yr^{-1} while transpiration and sensible heat flux are in W m^{-2}. For the fixed-point experiments, the regional average for the 3rd, 4th, 19th, and 20th steps are shown to demonstrate that the non-convergence does not attenuate with increasing number of iteration steps; while convergence can be achieved at the 20th iteration step.

[*] The western United States is defined as the area: 30~50°N, 130~105°W.

[†] The eastern Amazon is defined as the area: 20S~EQ, 60~40W.

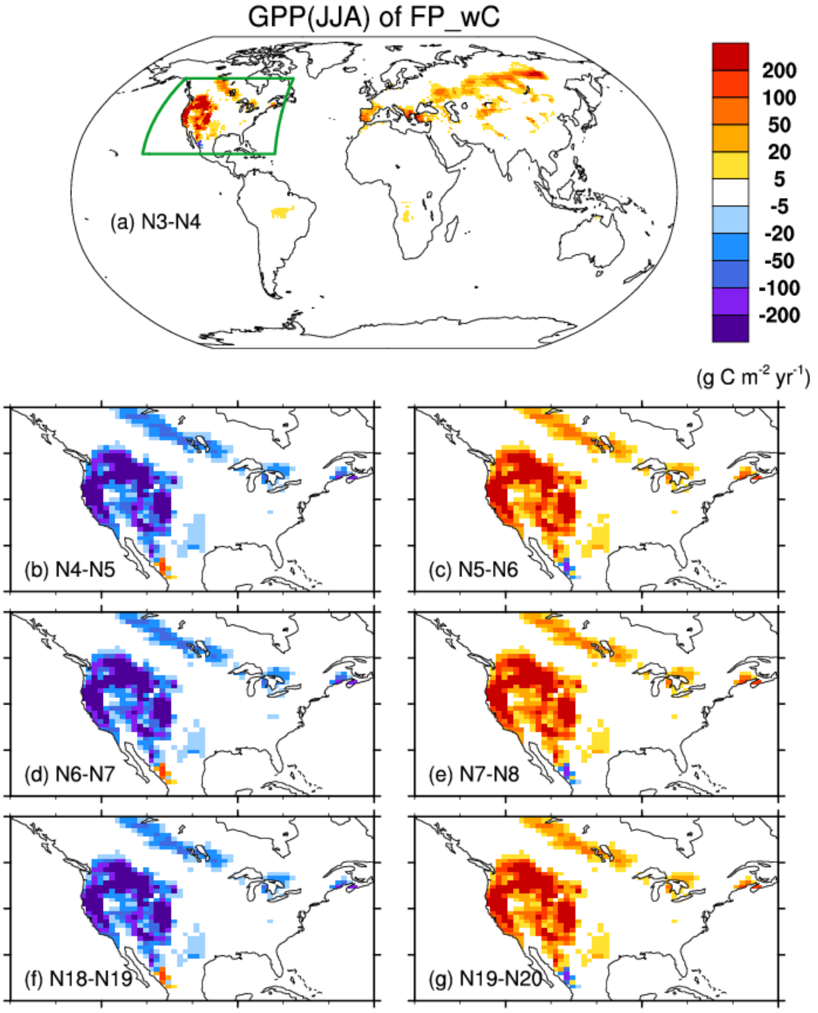

Figure 5.1. Differences of 1948 JJA-mean GPP between two successive iteration steps for the simulation experiment FP_wC.

Panels show the GPP (g C m^{-2} yr^{-1}) differences between two iteration steps: (a) 3rd and 4th, (b) 4th and 5th, (c) 5th and 6th, (d) 6th and 7th, (e) 7th and 8th, (f)18th and 19th, and (g) 19th and 20th iteration step, respectively (the iteration steps are denoted as N3, N4, ⋯, and N20). (b)-(g) are the subsets of the United States highlighted by the box region in (a). Here the year 1948 is chosen for demonstration of non-convergence arising from fixed-point approach, and is also used in the following relevant figures for consistency.

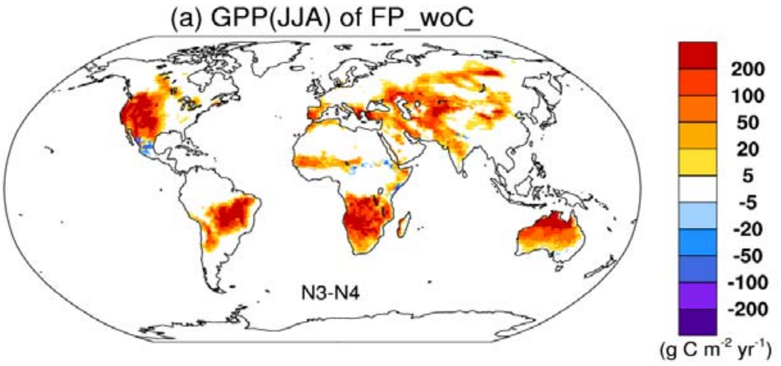
(a) GPP(JJA) of FP_woC

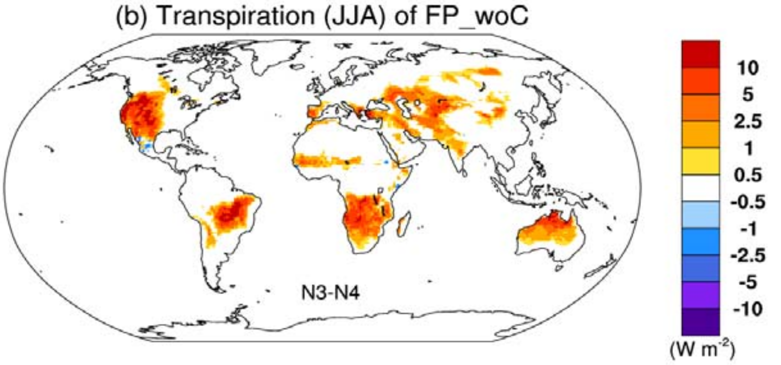
(b) Transpiration (JJA) of FP_woC

Figure 5.2. Differences of 1948 JJA-mean GPP and canopy transpiration between the 3rd and 4th iteration step for the simulation experiment FP_woC.

Panel (a) GPP (g C m^{-2} yr^{-1}) and (b) canopy transpiration (W m^{-2}). Panel (a) is similar to Figure 5.1a but for FP_woC.

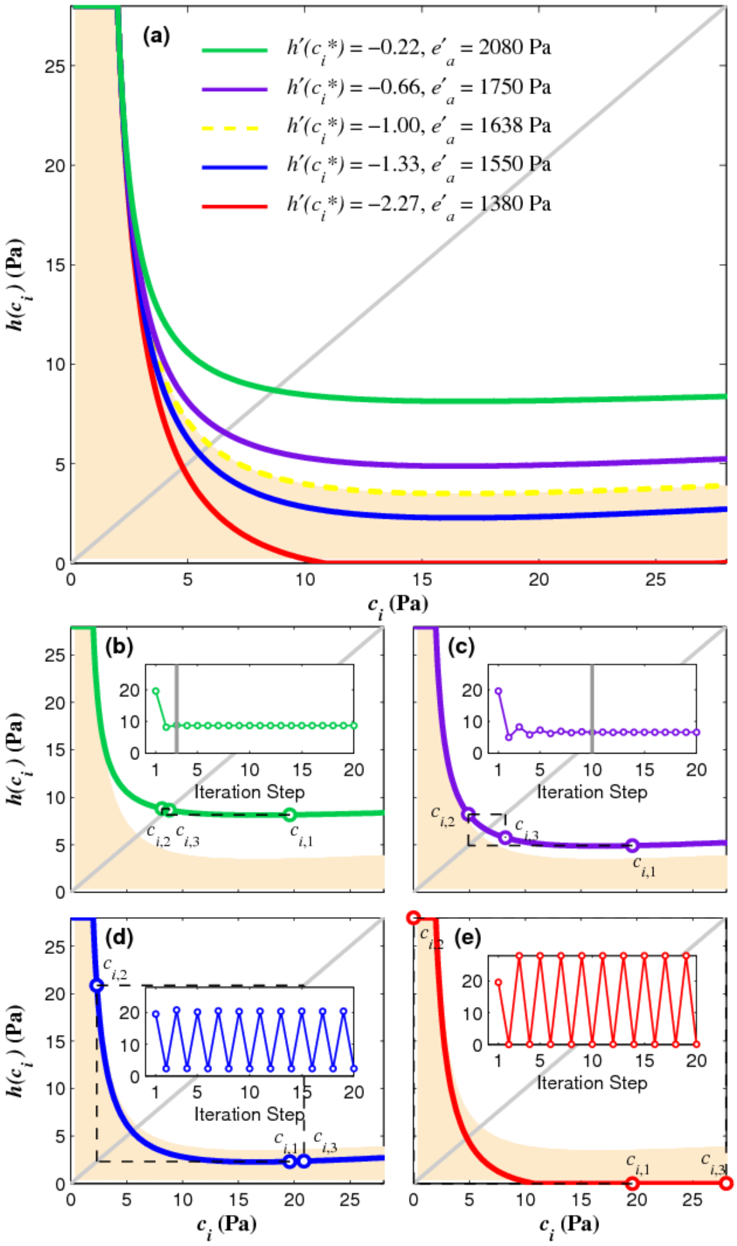

Figure 5.3. Typical convergence scenarios of the fixed-point iteration function $h(c_i)$[*] for the coupled photosynthesis-stomatal conductance model (C_3) as formulated in the Community Land Model version4 (CLM4).

These scenarios are demonstrated with representative values of model parameters and varying values of the constrained water vapor pressure of canopy air e'_a[†]. Both the *x*- and *y*-axis are confined to the range from 0 to the atmospheric CO_2 partial pressure c_a, thus the maximum values of c_i and $h(c_i)$ are c_a. (a) shows the impact of different values of e'_a on the shape of $h(c_i)$ and its derivative at the root, i.e., $h'(c_i*)$; (b)-(e) illustrate the iterative generation of c_i for different scenarios in (a), identified with curve colors: (b) c_i converges within 3 steps of iteration (solid green), (c) c_i converges but beyond 3 steps (solid purple), (d) is a non-convergence case with c_i alternating between two constant values in the range of 0 and c_a (solid blue), and (e) is also a non-convergence scenario similar to (d) but with c_i taking the exact value of 0 and c_a in alternation (solid red). The four scenarios corresponds to different values of e'_a and hence the derivative of $h(c_i)$. The dash yellow curve in (a) represents the boundary from convergence to non-convergence, occurring at the root $h'(c_i*) = -1$, the criterion of the fixed-point theorem. The area below this boundary is shaded, corresponding to the non-convergence region, where $h'(c_i*) < -1$. The iterative solution c_i* is the intersection of the $h(c_i)$ curve and the diagonal line $y = x$ (solid grey), i.e., the root of $h(c_i) = c_i$. The sequences of $c_{i,\mathrm{k}}$ (the subscripts k is the iteration step) are marked on the $h(c_i)$ curves, with black dash lines indicating the iteration loop. For clarity, only the first three $c_{i,\mathrm{k}}$ are shown. The initial guesses $c_{i,1}$ have the same value for all scenarios, i.e., $c_{i,1} = 0.7 \cdot c_a$. The insets in (b)-(e) show the c_i (Pa, the y axis) as a function of iteration step (from 1 to 20, the x axis) for each scenario. The vertical grey lines in the insets of (b) and (c) highlight the step at which the convergence is achieved, that is 3 steps for (b) and 10 steps for (c), respectively. Model parameters used to generate these curves are: the absorbed photosynthetically active radiation ϕ = 2000 μ mol photon m^{-2} s^{-1}, the maximum Rubisco carboxylation rate V_{cmax} = 40 μ mol m^{-2} s^{-1}, the CO_2 compensation point Γ_* = 2 Pa, the composite Michaelis-Menten constant K_{co} = 100 Pa ($K_{co} = K_c \cdot (1 + O / K_o)$), leaf boundary-layer resistance $r_b = 1.0 \times 10^{-6}$ s m^2 μ mol^{-1}, and the atmospheric CO_2 partial pressure c_a is 28 Pa.

[*] Refer to Equation 5.7.

[†] Refer to Equation 5.3.

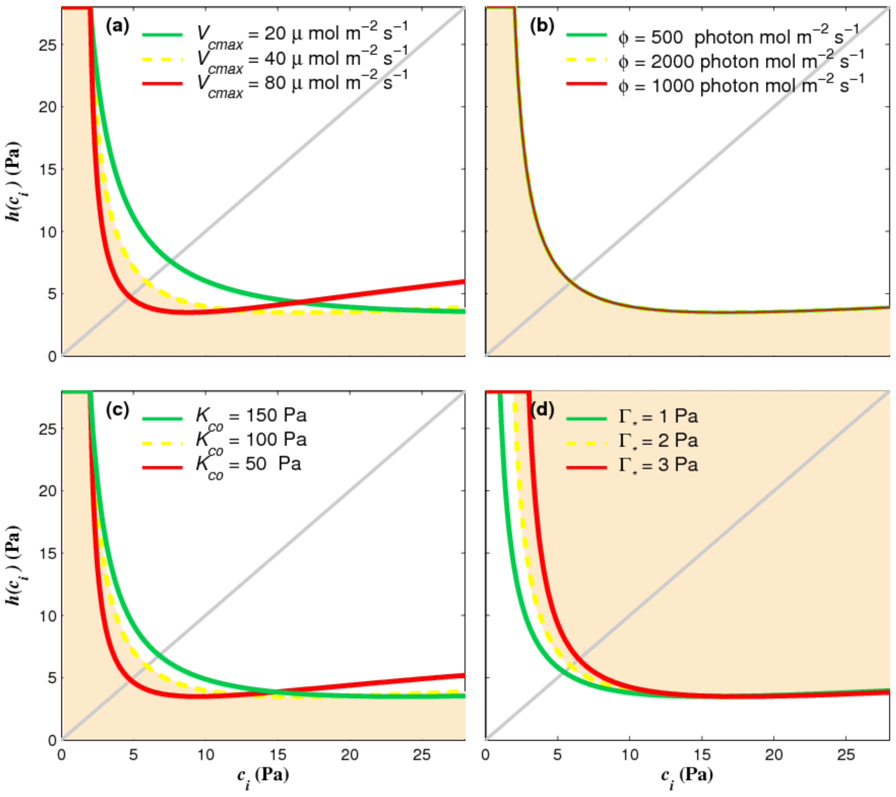

Figure 5.4. Sensitivity of the $h(c_i)$ shape to key parameters in the coupled photosynthesis-stomatal conductance model (C$_3$).

The parameters investigated are: (a) the maximum Rubisco carboxylation rate V_{cmax}, (b) the absorbed photosynthetically active radiation ϕ, (c) the composite Michaelis-Menten constant K_{co} (= $K_c \cdot (1 + O / K_o)$), and (d) the CO$_2$ compensation point Γ_*. The solid red and solid green curves represent non-convergence and convergence cases, respectively. The dash yellow curves represent the boundary between the convergence and non-convergence regions, identical to that in Figure 3a. The shaded area in each plot corresponds to the non-convergence region, which is below the yellow boundary in (a)-(c) but above it in (d). The solid grey line is the reference $y = x$. These $h(c_i)$ curves are produced by varying individual parameters in (a)-(d), with all the other parameters fixed at the same value as the boundary curve. Note that the relative distributions of convergence and non-convergence region are only meaningful to the particular parameter under consideration and are not comparable across plots (parameters) as they are entirely determined by how the concerned parameter affects the derivative of $h(c_i)$ with respect to c_i near the root when all other parameters are fixed. For example, when all other parameters are fixed, increasing Γ_* in (d) tends to steepen the slope of the iteration curve, which changes the fixed-point iteration from convergence to no-convergence and moves the iteration curve to the upper right corner in the h versus. c_i domain. In contrast, decreasing K_{co} (c) tends to have the same effect in terms of convergence but move the curve to the lower right corner.

(a) 2m Relative Humidity(JJA)

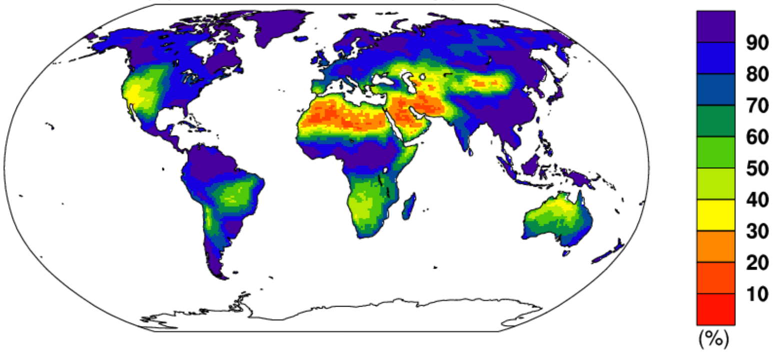

(b) 2m Air Temperature (JJA)

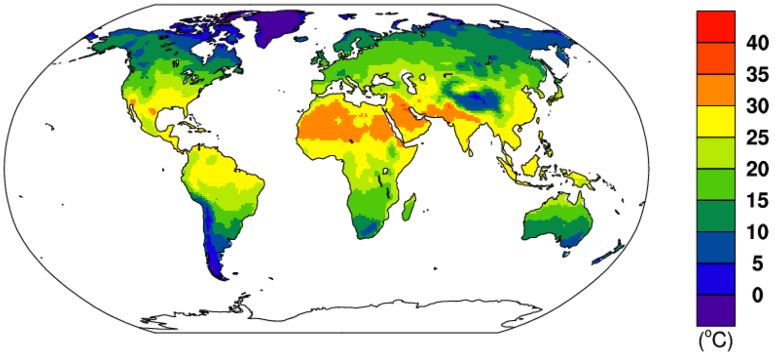

Figure 5.5. The JJA-mean (1948) relative humidity (RH) and 2-m air temperature. Panel (a) RH (%) and (b) air temperature (°C) at the height of 2m.

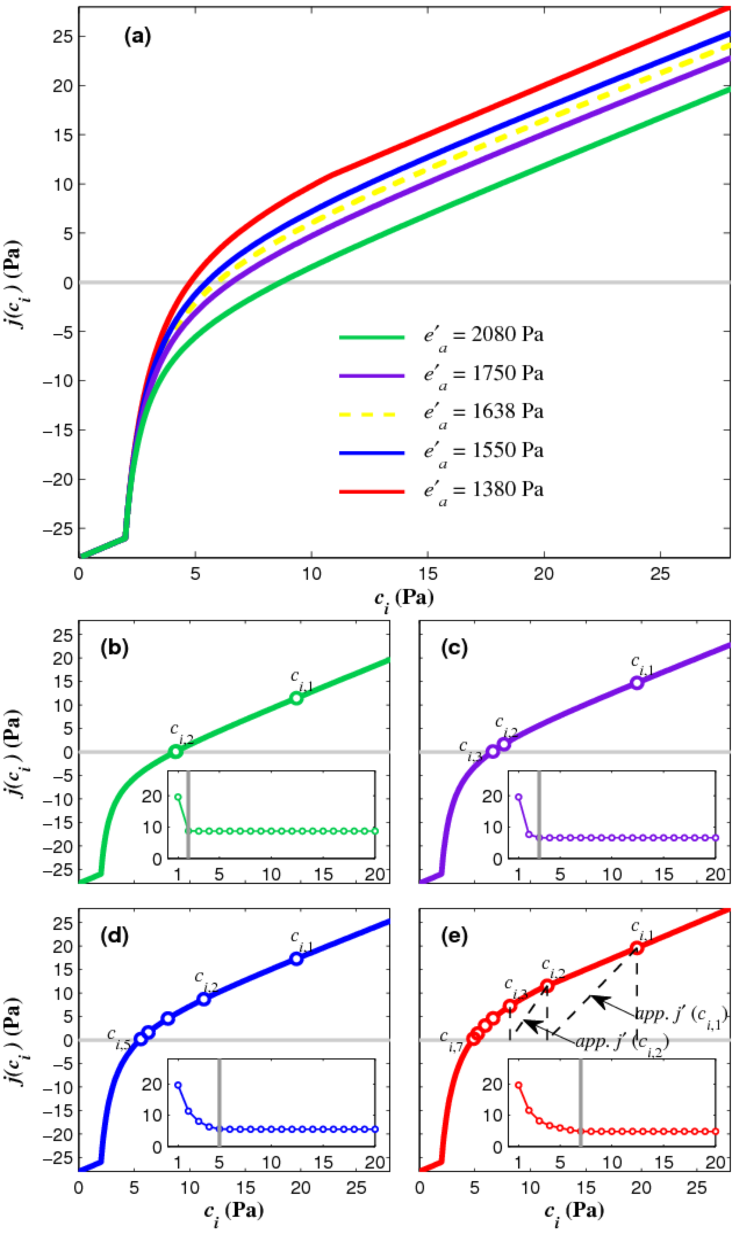

Figure 5.6. The mathematical properties of the Newton-Raphson iteration function $j(c_i)^*$ for the coupled photosynthesis-stomatal conductance model (C_3).

The curves displayed here correspond to those in Figure 5.3, using the same sets of model parameters. Here the roots of c_i are achieved for all scenarios through the Newton-Raphson approach, regardless of the derivative of the iteration function. The iterative solution c_i* is the intersection of the $j(c_i)$ curve and the reference line $y = 0$ (solid grey), i.e., the root of $j(c_i) = 0$. The sequences of $c_{i,\mathrm{k}}$ are marked on the $j(c_i)$ curve in (e), with black dash lines indicating the iteration processes and with the arrows pointing to the approximated derivative of $j(c_i)$ at $c_{i,1}$ and $c_{i,2}$. The insets show the calculated c_i (Pa, the y axis) at each iteration step (the x axis). The vertical grey lines in the insets of (b)-(e) highlight the step at which the convergence is achieved, that is 2 steps for (b), 3 steps for (c), 5 steps for (d), and 7 steps for (e), respectively.

---

[*] Refer to Equation 5.9.

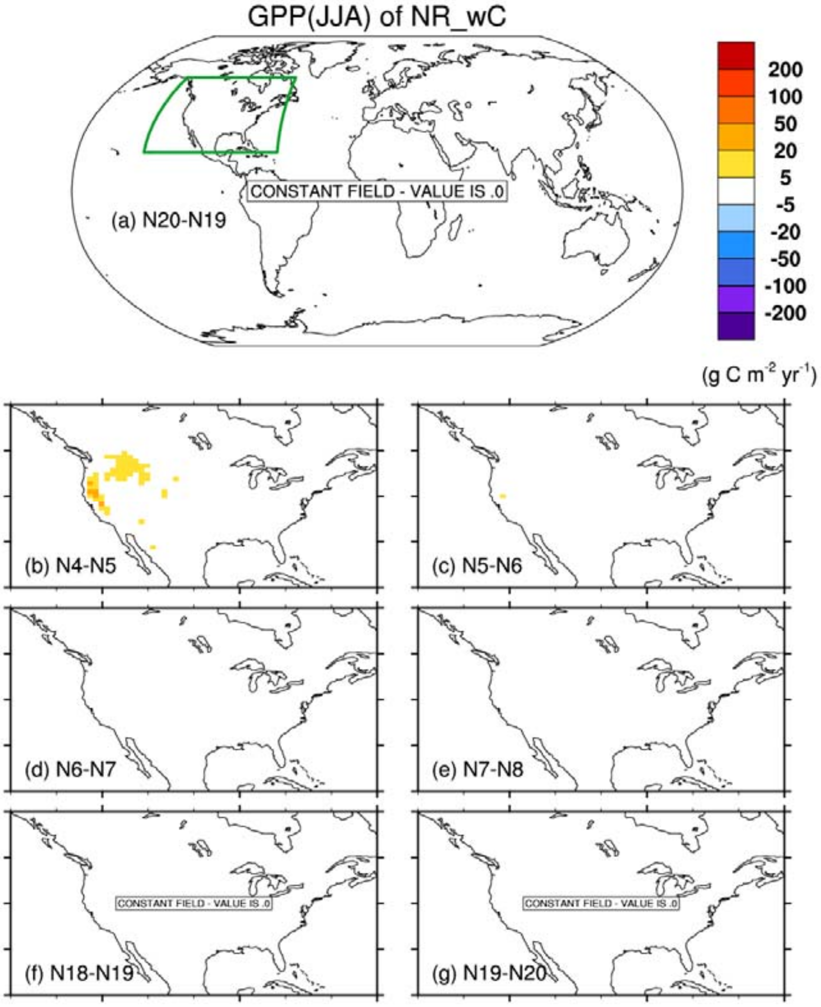

Figure 5.7. Differences of 1948 JJA-mean GPP between two successive iteration steps for the simulation experiment NR_wC.

Similar to Figure 5.1 with exception of (a), which shows the differences of JJA-mean GPP (g C m^{-2} yr^{-1}) between the 20th and 19th iteration step since N20 is the reference for the Newton-Raphson approach.

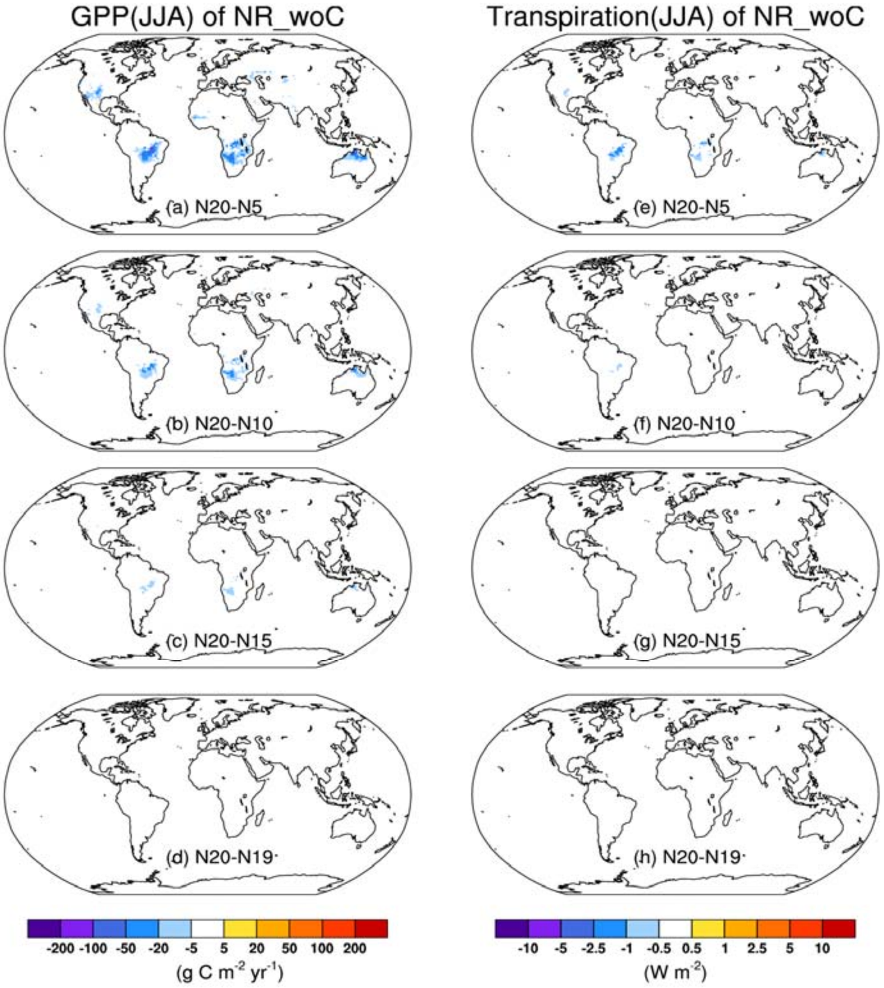

Figure 5.8. Differences of JJA-mean (1948) GPP and canopy transpiration between iteration steps for the simulation experiment NR_woC.

Panels (a)-(d) GPP (g C m^{-2} yr^{-1}) and (e)-(h) canopy transpiration (W m^{-2}) between the 20th and 5th, 10th, 15th, and 19th iteration step.

(a) GPP(JJA) bias

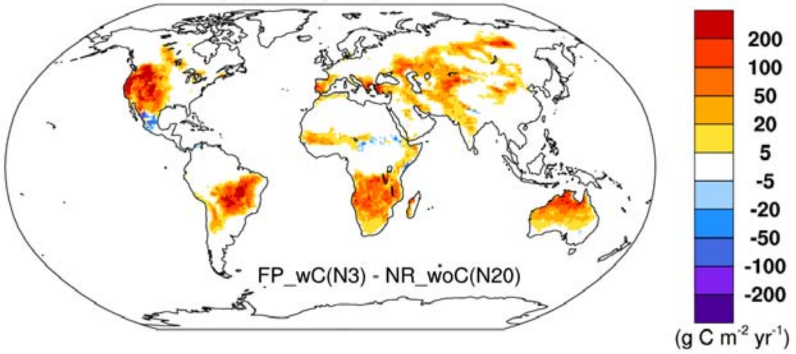

(b) Transpiration (JJA) bias

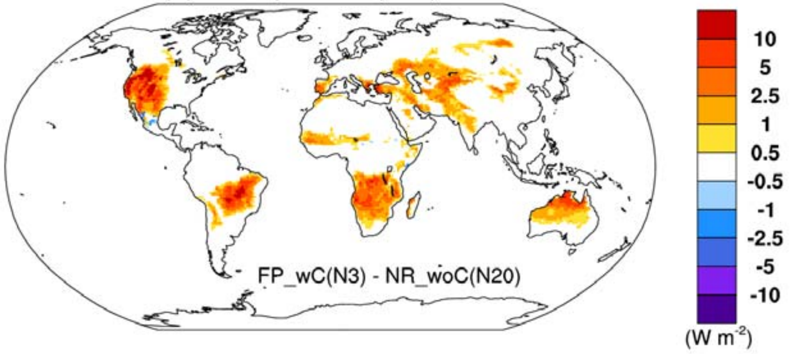

Figure 5.9. The bias of GPP and canopy transpiration in the default CLM4 FP_wC from the true estimates NR_woC.

Differences of JJA-mean (1948) (a) GPP (g C m^{-2} yr^{-1}) and (b) canopy transpiration (W m^{-2}) between the 3rd iteration step of FP_wC and the 20th step of NR_woC, indicating the bias of the default CLM4 FP_wC(N3) from the true estimates NR_woC(N20).

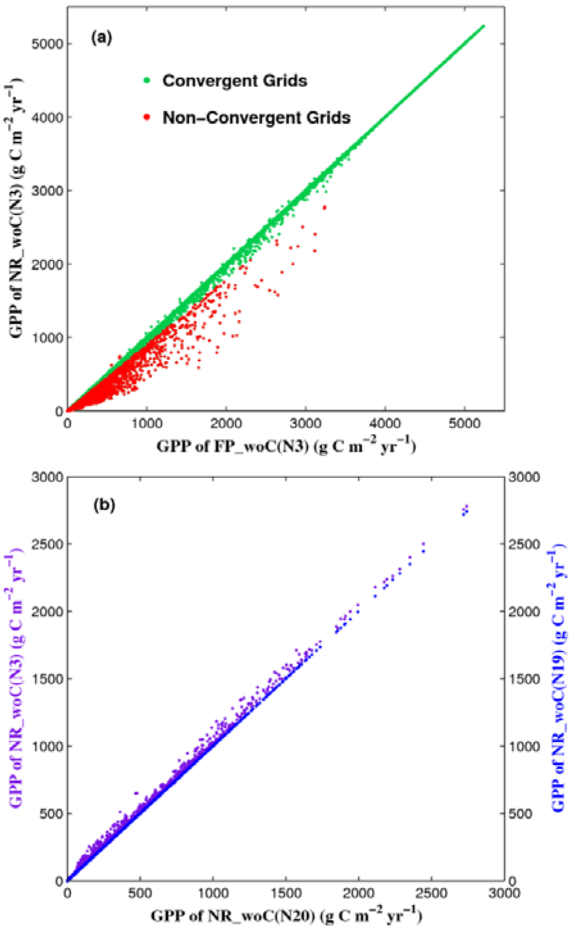

Figure 5.10. Evaluation of grid-scale GPP simulated by the fixed-point (FP) and by the Newton-Raphson (NR) iteration scheme at multiple iteration steps.

Panel (a) compares the GPP (g C m^{-2} yr^{-1}) simulation of NR_woC versus that of FP_woC. Both simulations are performed using the maximum iteration step N=3. Each dot represents a grid cell on land. All land grids across the globe are displayed here, excluding those in Antarctic. The green dots, which are located around the $y = x$ line, represent grids where both the NR and FP schemes achieve convergence at the 3rd step. The red dots, which deviate from the $y = x$ line, represent the non-convergence grids. (b) shows the GPP simulation of NR_woC with N=3 (purple, left ordinates) and with N=19 (blue, right ordinates) versus that with N=20 for all the non-convergence grids in (a). The blues dots form a $y = x$ line, indicating that the convergence of NR scheme can be achieved completely within 20 iteration steps. The purple dots are close to the $y = x$ line, suggesting that the Newton-Raphson iteration with N=3 can yield a GPP that closely approaches the true value, but more iterations are needed to ensure a full convergence.

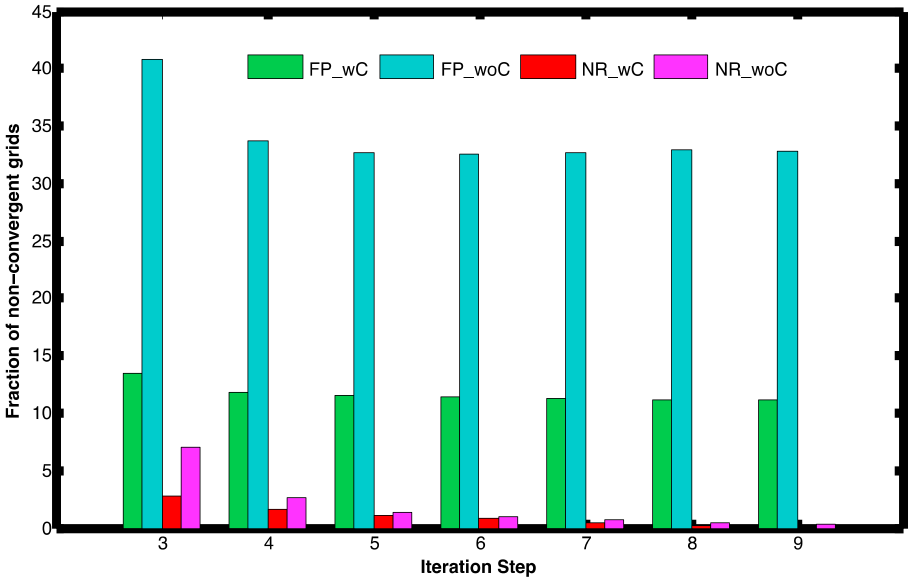

Figure 5.11. The fraction of non-convergent grids versus the iteration step for the simulation experiment FP_wC, FP_woC, NR_wC and NR_woC, respectively.

The fraction is calculated as the number of non-convergent grids relative to the total land grids (except Antarctic).

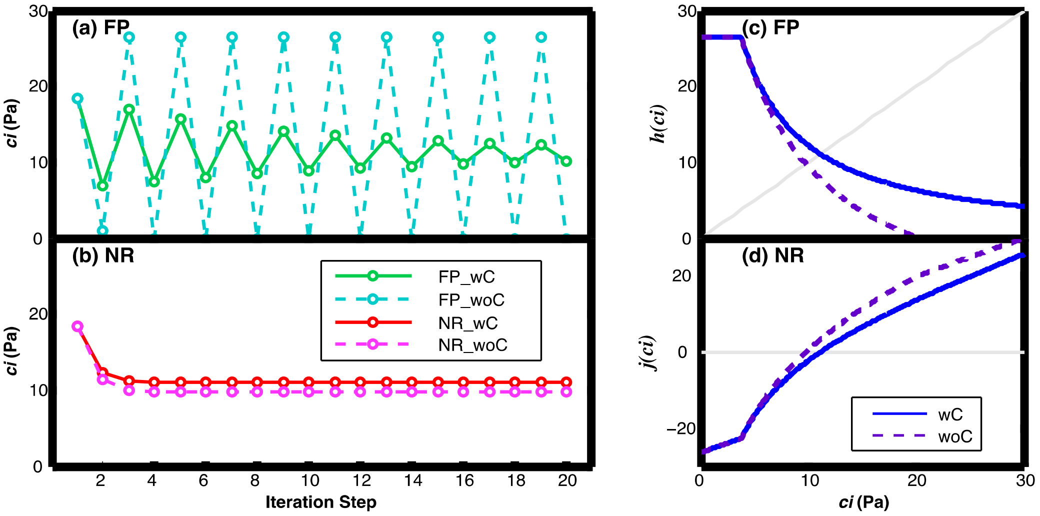

Figure 5.12. The iterative values of c_i as a function of iteration steps.

The values of c_i (Pa) as a function of iteration steps for (a) FP_wC (green solid) and FP_woC (cyan dash) and for (b) NR_wC (red solid) and NR_woC (pink dash). Here a PFT-level iteration of one grid in western US is selected as an example to demonstrate the effect of artificial constrain of e'_a on the convergence of c_i. (c) and (d) show the fixed-point function $h(c_i)$ and the newton-raphson function $j(c_i)$ versus the input of c_i with blue solid curves representing FP_wC (c) and NR_wC (d), and purple dash curves for FP_woC (c) and NR_woC(d). The grey lines are $y = x$ in (c) and $y = 0$ in (d). The shifts of the true c_i (the intersections of functional curves and the reference grey lines) indicate that artificial constrain of e'_a affect the final solution of c_i.

Chapter 6: Forest greenness after the massive 2008 Chinese ice storm: integrated effects of natural processes and human intervention[2]

6.1. ABSTRACT

About 10% of China's forests were impacted by a destructive ice storm (10 January to 6 February 2008) and subsequently subjected to poorly planned salvage logging in 2008. We used the remote-sensing products of Enhanced Vegetation Index (EVI) corroborated with information gathered from ground visits to examine the spatial patterns and temporal trajectories of greenness of these nearly 20 million hectares of forests. We found (1) the EVI of about 50% of the impacted forests returned to normal status (i.e., within the 95% confidence interval of the long-term mean) within five months, and about 80% within one year after the storm, (2) the higher the pre-storm EVI (relative to the long-term mean), the slower the rebound of post-storm EVI, and (3) the rebound of greenness was slowest in forests that were moderately impacted by the ice storm only (i.e. before the occurrences of logging), resulting in a nonlinear relationship between Greenness Rebound Time (GRT) and ice storm Impact Severity (IS). Ground visits suggested a hypothesis that the regional-wide rebound in greenness was a consequence of resprouting of physically damaged trees and growth of understory plants including shrub, herbaceous and epiphytic species. These processes were facilitated by the rapid increase in temperature and ample moisture after the ice storm. Gap-phase dynamics could be responsible for the obtained counterintuitive relationship between IS and GRT. However, a more parsimonious explanation appears to be biased salvage logging, which may have selectively targeted lightly to moderately impacted forests for

---

[2] Substantial portions of this chapter were previously published in Sun, Y., L. Gu, R. E. Dickinson, and B. Zhou, 2012b: Forest greenness after the massive 2008 Chinese ice storm: integrated effects of natural processes and human intervention. *Environ. Res. Lett.*, **7**, 035702, doi:10.1088/1748-9326/7/3/035702. The References section contains full citations for all articles referenced here.

economic and accessibility reasons and thus adversely affected the GRT of these forests. Although a pure natural disturbance may result in different forest greenness patterns than reported here, we suggest that remote sensing-based dynamic analyses of greenness can play a major role in evaluating disturbance theories and in developing testable hypotheses to guide ground-based studies of the integrated effects of large extreme events and human intervention on forest ecosystems.

6.2. INTRODUCTION

Forests currently offset a substantial portion of anthropogenic carbon emissions (Pan et al. 2011). The sustainability of this carbon sink is strongly affected by the frequency and intensity of Large Extreme Events (LEEs) (Turner and Dale 1998; Frolking et al. 2009) and hinges upon how quickly impacted forests can regain their photosynthetic capacity (e.g., Amiro et al. 2010). At present, our understanding of ecophysiological processes controlling the post-LEE regaining of forest photosynthetic capacity is very limited, which contributes to the large uncertainties in the estimated components and net exchanges of terrestrial carbon cycles at various scales (Liu et al. 2011; Running 2008). Although there may have been considerable advances in the studies of successions of forest structures after large disturbances (e.g., Dale et al. 2005), these advances have yet to be transformed into understanding the functional ‘succession’ of forest photosynthetic capacity. In particular, ecological succession reforms landscapes and ecosystems at different time scales in response to LEE (Bonan 2008b), which is difficult to quantify for the purpose of estimating photosynthetic capacities of disturbed forests. Also, humans often take immediate actions to minimize economic loss after a sizable area of forests has been impacted by natural forces (e.g., salvage logging, Donato et al. 2006; Foster et al. 1997; Lindenmayer et al. 2004). As a consequence, ecophysiological processes, ecological successions and intervening anthropogenic activities may jointly control the post-LEE regaining of forest photosynthetic capacity. Hence, knowledge of these joint controls is needed to develop realistic representations of LEEs and associated societal responses in ecosystem and earth system models (Running 2008).

It is difficult to conduct controlled experiments on LEEs because of their unpredictability and broad spatial and temporal scales. Yet a common feature of LEEs is their spatially heterogeneous impact which could be caused by either initially heterogeneous landscapes or heterogeneous disturbance forces or both (Turner 2010). Spatial heterogeneity can also be caused by intervening human activities which may selectively target the impacted landscapes for various reasons including economics, accessibility and conservation. This spatial heterogeneity provides a natural laboratory for studying the post-LEE photosynthetic rebuilding process and its controlling factors (e.g., Amiro et al. 2010; Pickett 1989).

Remote sensing is an effective tool for assessing the spatial heterogeneity of the impact of LEEs on forests (Frolking et al. 2009; Mildrexler et al. 2009). Satellite greenness indices such as the Normalized Difference Vegetation Index (NDVI) (Goetz et al. 2006) and the Enhanced Vegetation Index (EVI) (Huete et al. 2006) have been used routinely to monitor photosynthetic activities at large scales. These indices measure the vigor of the green elements (actively photosynthesizing), i.e., the greenness, of the vegetation and provide a proxy for canopy biophysical/biochemical variables, e.g., leaf chlorophyll content, leaf area, canopy cover, and structure. Generally, a greener or higher vegetation index corresponds to higher canopy photosynthetic capacity (Huete et al. 2011). A challenge is how to use remote sensing to fill our current knowledge gaps about natural and anthropogenic factors controlling the post-LEE photosynthetic rebuilding process as remote sensing itself does not provide direct information about underlying ecological, biological and societal mechanisms. One approach is to employ satellite data to identify spatial and temporal patterns of post-LEE forest greenness and then use the identified patterns to evaluate existing disturbance theories or develop testable hypotheses to guide ground-based studies. A rare opportunity to assess this approach was provided by a massive ice storm that occurred in 2008 in China (Zhou et al. 2011b).

Ice storms are common in East Asia (Zhou et al. 2011b) and in North America (Changnon 2003). Individual ice storms can cause losses of over millions of dollars and their devastating impact often dominates news headlines in winters. Yet climatological and ecological studies pay relatively less attention to these winter storms compared to extreme events that occur in warm periods of a year. Like hurricanes and tornados (e.g., Chambers et al. 2007; Lindroth et al. 2009), ice storms exert their impact on forests mainly through physical forces.

The 2008 ice storm struck southern and central China from 10 January to 6 February 2008 (Zhou et al. 2011b), a region of prominence for China's terrestrial carbon storage (Piao et al. 2009). Record-breaking ice thickness, ranging from 60 to 160 mm, coated 12% of China's territory (Figure 6.1). Direct economic losses were estimated to exceed $20 billion (Zhou et al. 2011b). Forests suffered massive physical destruction and to a lesser degree, physiological damage. The area of impacted forests with at least 10% standing volume loss was estimated to be about 20 million hectares, equivalent to 10% of China's total forest cover. Also, the lost standing volume of the impacted area was 3% of the overall forest volume of the country (Zhou et al. 2011b). Impacts on forests were diverse across the storm region (Zhou et al. 2011b,a; Shao et al. 2011). Damage to individual trees included crown decapitation, stem breakage / splitting, branch snapping, bending, and uprooting. Some species experienced physiological damage, typically showing cambium browning (Zhou et al. 2011b). At stand levels, damage ranged from loss of foliage to whole-stand destruction. The initial storm impact also led to some secondary impacts such as increased soil erosion, landslides, fires, and insect infestation (Zhou et al. 2011b). Poorly planned salvage logging was observed during our visits to the region shortly after the storm ended. In this study, we take advantage of the spatial heterogeneity in the ice storm impact on China’s forests to address the following questions: How do the degrees of ice storm impact, pre-storm vegetation growth status, and salvage logging jointly affect the spatial and temporal patterns of satellite-derived forest greenness? Can current disturbance theories explain the satellite-derived patterns which represent the integrated effects of natural processes and human intervention?

6.3. DATASETS

6.3.1. Satellite observations

We needed a measure to quantify the Impact Severity (IS) of the ice storm itself on forests (without the effect of subsequent disturbance caused by salvage logging). The IS of a LEE on forests can be defined in numerous ways with ground-based information, e.g. percentage of trees (basal area / volume) damaged, the amount of coarse woody debris produced, reduction in photosynthetic capacity, and changes in species composition and ecosystem biogeochemical processes (Foster et al. 1997; Frolking et al. 2009). These measures require carefully planned, intensive investigation with extensive ground-survey plots carried out shortly after the LEE is over but before regrowth or salvage logging takes place. This, however, was not possible for the 2008 Chinese ice storm. The impacted area was too large and the time window allowed to complete these massive tasks was too short for adequate ground-based investigation. The ground-based measures also require pre-storm vegetation information for reference, which was also not available. Therefore we defined IS in terms of immediate change in post-storm forest greenness because it is routinely measured with remotely sensed vegetation indices.

Our study used the Enhanced Vegetation Index (EVI) (Huete et al. 2006) products (MOD13A1) of the Moderate Resolution Imaging Spectroradiometer (MODIS) covering the period from January 2001 to December 2010. The EVI products have a spatial resolution of 500m and a temporal resolution of 16 days (16-day composites). We screened EVI values according to the associated quality flags to remove the pixels contaminated by clouds or aerosols (Xu et al. 2011). This study concerned only forests; therefore, we applied the International Geosphere Biosphere Programme (IGBP) land-cover classification scheme to extract the forested pixels from the MODIS land-cover type products (MCD12Q1) (Friedl et al. 2002) with a 500m spatial resolution. To minimize the effects of possible disturbance events occurred before 2008 on land cover, we used the land-cover data at the year 2007 to identify forested areas.

The use of satellite-derived forest greenness indices such as EVI and the Normalized Difference Vegetation Index (NDVI) to define the IS of a LEE has shortcomings. These indices tend to saturate at high leaf area indices, an issue of particular concern for regions with dense vegetation such as tropical rainforests (e.g., Brantley et al. 2011). Even though the southern and central China is mostly occupied by young and secondary growth forests (Zhou et al. 2011b) and is not known to have very dense vegetation, we decided to use EVI instead of NDVI because it is less likely to saturate with respect to leaf area index and more robust to different atmospheric conditions and different soil types (Huete et al. 2002). This characteristic is important to studying the ice storm impact.

6.3.2. The domain of storm-impacted region and its forest types

The ice storm region (Figure 6.1) was delineated according to the number of freezing days (FDs) during the ice storm period (from 10 January to 6 February 2008). Chen and Sun (2010) determined the spatial distribution of FDs by calculating FDs at 186 weather stations and then gridding the calculated FDs by applying an inverse distance weighting interpolation method. A FD was defined as a day when the daily mean temperature was below 1°C with precipitation accumulation (National Climate Center 2008). An estimated area of 1.19×10^6 km^2 (12.4% of China’s territory) experienced at least one FD. We overlaid the FD map with the land-cover map and extracted forested pixels with at least one FD.

We also examined daily mean surface temperature and precipitation records in 2008 at three weather stations. These stations, which traversed the storm region, were located in Changsha (28°12’N, 112°58’E, Hunan province), Guiyang (26°25’N, 106°44’E, Guizhou province), and Quzhou (28°58’N, 118°52’E, Zhejiang province), respectively.

The ice storm region is bounded roughly by the Yangtze River in the north, the East China Mountains along the coast, the Nanling/Wumeng Mountains in the south, and the Hengduan Mountains in the west (Figure 6.1). This is a large swathe of land with topography conducive to the formation of ice storm (Zhou et al. 2011b). The climate of the region is subtropical and monsoonal with hot and humid summer and cool but short winter. The classification of MODIS plant functional types identifies the forests of the ice storm region as mostly deciduous broadleaf forests (~60%) with smaller portions of evergreen needleleaf and and evergreen broadleaf forests (~20% each type). However, later we will present evidence that forest types did not affect the relationships among key variables of interest to this study. Both naturally regenerated forests and plantations exist in the region. Popular species for plantations include the native species of *Pinus massoniana* (Lamb.), *Cunninghamia lanceolata* (Lamb.), and *Phyllostachys heterocycla* var. *pubescens* and exotic species *Pinus elliottii* Engelm, *Pinus taeda* L. and *Eucalyptus* spp. The species of natural forests are extremely diverse as this region is one of the biodiversity hotspots in China (Liu et al. 2003; Tang et al. 2006).

6.3.3. Ground visits

Ground visits were part of large efforts to investigate the socioeconomic-ecological impact of the ice storm (Zhou et al. 2011b). Between April and November 2008, two of my collaborators (Drs. Lianhong Gu and Benzhi Zhou), together with their collaborators, visited the counties of Yongxing, Zixing, and Guiyang in Hunan province, the Nanling Natural Reserve in Guangdong province, the Dagangshan Mountain and the Qianyanzhou Ecological Research Station in Jiangxi province, and the Jianglangshan Natural Reserve in Zhejiang province. Through these visits, we assessed the impact of the ice storm on forests, the post-storm vegetation growth, and the activities of villagers in damaged forests. The objective of these visits was on the extent of the ice storm impact and thus the information collected was largely qualitative except at the ecological research stations in the Nanling Natural Reserve and the Jianglangshan Natural Reserve where quantitative measurements were made and continued thereafter. We observed widespread resprouting of decapitated, uprooted or otherwise damaged trees. Understory, herbaceous and epiphytic growth under destroyed or open canopies was pervasive and lush green covered the ground as early as in April.

6.4. METHODS

6.4.1. The standardized detrended vegetation index (SDVI)

We quantified the IS of forest pixels by transforming EVI into a Standardized Detrended Vegetation Index (SDVI), hence removing long-term trends and seasonal variations from the original 16-day composite data and allowing the resulting SDVI to be compared across time and across pixels for disturbance effects.

We first performed linear detrending to remove the long-term trend in the quality-checked EVI time series. This step was necessary because forests in the storm region were mostly young secondary regrowth forests and plantations (Zhou et al. 2011b) and because climate in past decades may have experienced systematic changes with consequences on long-term forest primary productions (Zhao and Running 2010). The detrending was done independently for each MODIS 16-day composite period according to the following equation:

$$DVI_{ij} = VI_{ij} - (b_{0j} + b_{1j} \times t_{ij}), \qquad (6.1)$$

where DVI_{ij} refers to the detrended EVI of the calendar year i (2001-2010) at the 16-day period j (Day Of Year, DOY 001 - 353); VI_{ij} the EVI of this period; t_{ij} the time of the current period since the starting period of the time series (DOY 001, 2001); b_{0j} and b_{1j} two regression coefficients for period j.

The detrended EVI still cannot be used directly in the analysis because even in normal years this index would differ from pixel to pixel and vary seasonally to interannually as the original EVI does. To detect and quantify the impact of a disturbance on forests in a heterogeneous region, some standardization procedures must be adopted so that normal variations in time within a pixel and across pixels are removed and only signals caused by the disturbance are retained. We therefore standardized the detrended

EVI with respect to its long-term mean and variance in each 16-day period of each year according to the following equation (Chen and Sun 2010; Xu et al. 2011):

$$SDVI_{ij} = \frac{(DVI_{ij} - mDVI_j)}{\sigma DVI_j}, \tag{6.2}$$

where $SDVI_{ij}$ refers to the Standardized Detrended Vegetation Index (SDVI) of the calendar year i at the 16-day period j; $mDVI_j$ and σDVI_j represent the multi-year mean and standard deviation of the detrended EVI for the 16-day period j, respectively. $mDVI_j$ and σDVI_j were computed with data from the 16-day period j of all years as follows:

$$mDVI_j = \frac{\mathbf{1}}{\mathbf{10}} \sum_{i=2001}^{2010} DVI_{ij}, \tag{6.3}$$

$$\sigma DVI_j = \sqrt{\frac{\mathbf{1}}{\mathbf{9}} \sum_{i=2001}^{2010} (DVI_{ij} - mDVI_j)^2}. \tag{6.4}$$

The standardization removed the normal seasonal variation of ecosystem physiology in response to regular progression in climate and eliminated pre-existing spatial differences in vegetation states. Statistical tests and cross-examinations described later confirmed the robustness of our detrending and standardization procedures. Approaches for detecting disturbances with multiple remote sensing data streams have been developed in previous studies (Mildrexler et al. 2009). Our approach is employed here because similar approaches have been proven to be effective in previous studies (Goetz et al. 2006; Chen and Sun 2010; Xu et al. 2011) and because we were interested in an index that is correlated with forest photosynthetic capacity (Goetz et al. 2006; Huete et al. 2006).

6.4.2. The 95% confidence interval

The IS was objectively determined with SDVI, following the framework shown in Figure 6.2. To establish an objective criterion for detecting impacted pixels and for determining IS and Greenness Rebound Time (GRT), we computed the 95% confidence interval (CI) for the long-term mean SDVI using the time series from January 2001 to December 2010. The 95% CI was then used as a benchmark for quantifying the ice storm impact (Figure 6.2). The use of a 95% CI was statistically necessary because EVI varies both seasonally and annually even under normal conditions and these normal variations must be removed in order to evaluate the true disturbance signal. Although it is not a biologically-based criterion, its use is justifiable as this study is concerned with neither the total area of forests impacted nor the total biomass lost and only relative measures are of relevance to our objective.

6.4.3. Impact severity (IS) and greenness rebound time (GRT)

To facilitate the detection of impacted pixels and determination of ice storm impact severity and greenness rebound time, we fitted a sigmoid function to the post-storm SDVI time series in each pixel (Figure 6.2). The sigmoid function and its variants have been previously used in phenological analyses of vegetation index (Fisher et al. 2006; Zhang et al. 2003) and land surface fluxes (Gu et al. 2003b, 2009). It has the following form:

$$V(t) = y_0 + \frac{a}{1 + \exp(-\frac{t - t_0}{b})}, \tag{6.5}$$

where $V(t)$ is the modeled SDVI at time t; y_0, t_0, a, b are function parameters to be estimated. The post-storm SDVI time series started with the 4th EVI composite period of 2008 (DOY 049) and ended with the last composite period of 2010 (DOY 353). The first three MODIS composite periods in 2008 coincided with the long-lasting ice storm and were excluded from the fitting to avoid heavy cloud contamination and snow/ice-covered grounds. To ensure that the sigmoid function was well constrained during the crucial phase of post-storm vegetation photosynthetic recovery, we considered only those pixels with at least three quality-ensured points during the first nine MODIS composite periods in the post-storm SDVI time series. The empirical parameters in the sigmoid function were estimated with an optimization algorithm described elsewhere (Gu et al. 2010).

The detection of impacted pixels and the determination of ice storm impact severity and greenness rebound time were based on the optimized sigmoid function. We calculated the reduction of SDVI from its long-term mean (zero) on 1 March 2008 with the optimized function and used the obtained value as an index of IS to measure the direct effect of the ice storm. Dates before 1 March were close to the beginning of the time window used in the fitting, and the value of the optimized sigmoid function might not be reliably constrained. From 1 March onwards (three weeks after the storm ended), temperatures across the region rose rapidly and vegetation regrowth started. Warmer temperature may also allow salvage logging to proceed. Therefore, the SDVI value on 1 March should be free from the effects of regorwth and salvage logging and thus reflect the direct impact of the ice storm only. Thus we use it as an appropriate index of ice storm impact severity.We considered a pixel impacted by the ice storm if its IS value was outside the 95% CI of the long-term mean SDVI (Figure 6.2).

To provide a measure of how quickly the greenness of an impacted pixel rebounded, we calculated the time when the optimized sigmoid curve crossed the lower threshold of the 95% CI. The greenness of a given impacted pixel was considered restored to its long-term mean when the fitted sigmoid curve crossed the lower threshold of the 95% CI. The rebound time, i.e., GRT, was then defined as the number of days between the ending date of the ice storm (6 February 2008) and the date when the greenness was restored. GRT should reflect the integrated effects of natural processes as well as salvage logging if occurred, while IS should measure the direct impact of the ice storm physical forces only.

Furthermore, we determined the mean SDVI for the previous main growing season (May to October 2007). The 2007 Mean growing season SDVI could be considered as a measure for the pre-storm vegetation growth status relative to the long-term mean and thus be used to investigate how pre-storm vegetation growth status might interact with the storm to determine the impact.

The post-storm spatial and temporal patterns of forest greenness were analyzed in terms of the quantifiable variables of IS, GRT and pre-storm growing season SDVI. The use of a 95% CI in the analysis was not a biological mandate but a statistical necessity. EVI varies both seasonally and annually even under normal conditions and these normal variations must be considered in order to tease out the true disturbance signal. Using a different threshold may affect the determination of the total area of forests impacted or the total biomass lost, neither of which is the focus of this study. For our objective, only relative measures of disturbance impact are of importance and the criterion of a 95% CI satisfies our needs. Nevertheless we understand any spatial and temporal patterns identified with this criterion will be of statistical nature in general and their ecological implications will have to be examined within this context.

6.4.4. Validity of methods

The validity of the methods used was examined in multiple ways. The determination of a 95% CI usually assumes that the data are sampled independently from a normal distribution; we therefore conducted the Jarque-Bera (JB) test (Jarque and Bera 1987) to check the normality of the long-term SDVI time series to ensure the validity of the calculated 95% CI for each pixel. We found that the null hypothesis (the sample came from a normal distribution) could not be rejected for ~85% of the total quality-assured forest pixels at the 5% significance level. The JB test affirmed the effectiveness of the employed standardization and detrending procedures for producing temporally uncorrelated time series of SDVI. We compared the impact severity – greenness rebound time relationships based on the pixels that the null hypothesis was not rejected with those based on all impacted pixels and found the results to be similar.

A second test with respect to the calculation of 95% CI concerned the possible scenario that the occurrence of an extreme event in a short period might cast a strong bias in the data. We computed the corresponding 95% CI by excluding the ice storm period. Again, similar patterns on impact severity versus rebound time were found. Additionally, we tested an exponential function $SDVI = y_0 + a(1 - \exp(-b(t - t_0)))$ in the fitting and found that the results were similar to those obtained from the sigmoid function.

We further investigated whether the response of SDVI to disturbance had a residual seasonal dependence even after standardization was performed, e.g the dormant season SDVI might be less sensitive to disturbance impact than the growing season SDVI. We compared the impact severity – greenness rebound relationships obtained with and without inclusion of the data from winter periods and again found the results to be similar.

Finally, we checked whether the phenological differences between evergreen and deciduous forests might have confounded the obtained results. Our concern was that the inter-annual variability of spring green-up of deciduous forests may be larger than that of evergreen forests. Independent analyses were thus conducted for evergreen and deciduous forests. We found that the results for the two contrasting forest types were similar to each other and also consistent with those when all forest pixels were pooled.

To conclude, all statistical tests and cross-examinations confirmed the validity of our approach and the robustness of our findings. We therefore presented the results with all impacted forest pixels included so that the sample size was as large as possible.

6.5. RESULTS

The spatial distribution of forest pixels with IS below the 95% CI and thus identified as impacted by the ice storm is given in Figure 6.3. The locations were mostly mountainous regions where ice storm damages to forests were reported in ground-based studies (Zhou et al. 2011b,a; Shao et al. 2011) and also observed in our ground visits. These pixels tended to cluster and be more highly impacted in the mountains of Wuyishan, Jinggangshan, Lushan, and Wugongshan. Nevertheless, IS varied widely across space, with different degrees of impact occurring in close proximity. The probability density function (PDF) for the spatial variation of IS was a skewed unimodal distribution with a long tail towards high IS (Figure 6.4), indicating factors determining the degree of the ice storm impact may not be completely random and the ice storm caused extreme reduction in the relative values of EVI of some pixels.

The GRT also showed large variations occurring on a small scale (Figure 6.3b). Similar to that of IS, the PDF of GRT was also a skewed unimodal distribution with a long tail towards protracted restoration of greenness (Figure 6.4b). It had a peak around mid-May 2008 (GRT ~100 days). About 50% of the impacted pixels had the greenness restored to within the 95% CI of their long-term mean by early-July 2008 (GRT ~150 days), and about 80% within approximately one year after the storm (Figure 6.4b).

The IS, pre-storm growing season SDVI and GRT formed a tight relationship in the 3D space (Figure 6.5a). A local regression model (LOESS) fit the 3D scatter plot well (Figure 6.5b). Both the 3D plot and its cut-through views (Figure 6.5c and d) indicated that the three variables varied highly nonlinearly with each other. Higher pre-storm growing season SDVI tended to correspond to longer GRT for a given IS (Figure 6.5d).

Given the close resemblance between the IS and GRT PDF distributions (Figure 6.4), one might anticipate that GRT would be a monotonic function of IS, i.e., the more severely a pixel was impacted by the ice storm, the longer it would take for greenness to rebound. The observed relationship, however, showed that the maximum GRT occurred at an intermediate level of IS (Figure 6.5a and c). For lightly to moderately impacted forests, GRT indeed increased with IS. This is in contrast with moderately to severely impacted forests for which GRT shortened with increasing IS (Figure 6.5a and c).

6.6. DISCUSSION: POTENTIAL NATURAL AND ANTHROPOGENIC CAUSES OF OBSERVED PATTERNS

Overall, the post-storm greenness rebounded quickly even though the physical damage caused by the ice storm to the forests was massive. This fast rebound was likely a consequence of combination of abiotic and biotic factors. Shortly after the storm ended, temperatures in the region rose rapidly and precipitation was ample throughout the year (Figure 6.6). These favorable environmental conditions may have facilitated regional-wide regrowth of vegetation as seen in similar studies of other disturbances elsewhere (Law et al. 2002). Also the newly available nutrients released from dead biomass after disturbance may have stimulated vegetation regrowth (e.g., Franklin et al. 1987). Site visits between April and November 2008 by the authors revealed fairly thick growth of understory shrub / herbaceous / epiphytic plants taking advantage of an improved forest floor light environment under broken canopies. This response is a benefit of high species diversity in the storm region, one of the main biodiversity hotspots in China (Liu et al. 2003). Furthermore, tree species in the impacted region appear to have exceptional resprouting capacities (Nanami et al. 2004), an important life history strategy for persistence and quick recovery in tropical and subtropical forests (Poorter et al. 2010). Indeed, widespread resprouting of physically damaged trees was observed throughout the region (Figure 6.7). Although forest greenness rebounded rapidly, forest structure and some ecosystem functions, e.g., living biomass volume and carbon balance, may take decades or even longer time to recover (e.g., Amiro et al. 2010).

It is possible that anomalously high pre-storm growth relative to the long-term mean may have resulted in more post-storm necromass production, leading to increased fuels for fires (Zhou et al. 2011b); or, thicker biomass debris at better growth sites in 2007 relative to the long-term mean may have covered the ground and adversely affected post-storm understory growth in response to rapidly rising temperatures (Figure 6.6).

The exact causes of the satellite-derived patterns in forest greenness are difficult to ascertain because there is limited ground information on vegetation before and after the storm. However, it is interesting to compare these observed patterns with predictions of existing ecological disturbance theories. The insurance hypothesis suggests that higher species diversity can reduce the realized impact of a disturbance (Tilman 1996; Hughes et al. 2007). Ecologists also believe uncommon or rare species can play a pivotal role in the response of ecosystems to disturbances (Lyons et al. 2005; Duffy 2009) and that higher functioning and more stable ecosystem services over time are maintained by more diverse plant communities (Isbell et al. 2011; Allan et al. 2011). The region impacted by the ice storm is known for its high species diversity and our post-storm ground visits observed thriving shrub / herbaceous / epiphytic species under damaged canopies. Thus it is reasonable to suggest that species that normally do not dominate forest structures may have played a major role in the satellite-derived rapid rebound of forest greenness after the 2008 Chinese ice storm. If so, then our study appears to support the insurance hypothesis and the uncommon species hypothesis, suggesting that these hypotheses, which have been developed primarily from studies at scales much smaller than the massive ice storm, may transcend scales. The existing disturbance theories can be broadened by explicitly considering diversity in the life-history strategy of species as our ground visits suggested that resprouting of physically damaged trees may be also important for the rapid rebound of forest greenness. Dr. Xu Wang of the Chinese Academy of Forestry conducted a survey at the Nanling Natural Reserve (Figures 6.3 and 6.7) and found that all dominant tree species resprouted (Wang 2012). These species included *R. simsii* Planch., *E. muricata* Dunn., *R. kwangtungensis* Merr., *L. chinensis* Oliv., *R. latoucheae* Franch., *I. chinensis* Sims., *M. kwangtungensis* Yang., *D. oldhamii* Dosenth., *D. macropodium* Miq., *C. Hui* chun., *C. fordii* Hance., *C. eyrei* Tutch., *C. Carlesii*, *C. fargesii* Franch., *S. sinensis* Hemsl., *C. glauca* Oerest., *E. sylvestris* Poir., *C. lamontii* Hance., *G. japonica* Miq., *H. cochinchinensis* Lour., *M. oldhamoo* Maxim. The rate of resprouting ranged from 40 to 100% (Wang 2012).

It is challenging to explain the occurrence of longest GRT at some intermediate IS (Figure 6.5). According to the theory of gap-phase dynamics (Franklin et al. 1987; Osborne 2000), greater canopy gaps may be created in more disturbed forests, allowing more light and nutrients available to r-selected species for opportunist growth. As a result, more severely impacted forests had faster restoration of greenness. However, this cannot explain why GRT initially increased from lightly to moderately impacted forests. It is possible that relatively mild impact may have prevented the gap effect from being realized, a phenomenon that has been reported in previous studies (Hubbell 1999). If so, the temporal patterns of greenness of lightly to moderately impacted forests may largely reflect the changes of overstory canopies. The secondary hazards that occurred after the initial storm impact (Zhou et al. 2011b) could also contribute to the GRT – IS relationship if they took place more frequently in intermediately impacted forests. However we do not have information to confirm or refute this hypothesis.

The observed nonlinear pattern between the impact severity and greenness rebound time bears a striking similarity to the Intermediate Disturbance Hypothesis (IDH, Connell 1978). IDH states that highest species diversity is achieved at an intermediate level of disturbance, since extremely high level of disturbance (or frequent disturbances) are likely to lead to extinction of all species while very low disturbance (or infrequent disturbances) allow the most competitive species dominate, which also results in a low species richness. Can IDH explains the correspondence between the intermediate IS and longest GRT? Given the similar geometrical shape of IDH and the nonlinear IS-GRT pattern (Figure 6.5), it seems natural to build some causal relationship between them. In our case, IS might be a comparable measure to disturbance frequency or intensity that are used in IDH. If so, an intermediate IS would correspond to the maximal species diversity, which in turn would lead to fastest forest rebound, given the positive relationships between biodiversity and recovery rate as discussed before. This is in contradiction to what we found in Figure 6.5. The IDH has been questioned by recent studies (e.g., Fox 2012; Violle et al. 2010), and our study provides some additional evidence for such arguments. Our analysis is based on a single event and is not placed in a historical context of assessment of disturbance frequencies. Thus, IDH is probably not an appropriate mechanism for explaining the nonlinear IS-GRT pattern.

An alternative and more parsimonious explanation is that salvage logging after the ice storm preferentially targeted lightly to moderately impacted forests. Previous studies have shown that salvage logging can be detrimental to post-disturbance vegetation regrowth (Lindenmayer et al. 2004; Donato et al. 2006). Substantial salvage logging occurred after the ice storm. In 2008, the State Forestry Administration of China received requests for increasing logging quota from provinces affected by the ice storm and approved an average increase of 65% in logging quota (Figure 6.8). Our field visits observed salvage logging activities that were apparently carried out hastily with limited planning as they took place shortly after the storm ended. Previous studies have shown that salvage logging can increase mortality of seedlings and saplings that have survived the initial disturbance, create new disturbance to soil and microhabitat, and remove nutrients from dead trees that would otherwise be available for new growth (Lindenmayer et al. 2004; Donato et al. 2006; Thompson et al. 2007). Salvage logging may also undermine resprouting and damage forest floor vegetation that would otherwise flourish in an improved post-disturbance light environment and so contribute substantially to total photosynthesis at the site until the canopy is closed (Peterson and Pickett 1991; Roberts 2004; Lasso et al. 2009; Poorter et al. 2010).

Forests in the 2008 ice storm region were under the jurisdiction of the Natural Forest Conservation Program and the Grain to Green Program (Figure 6.1), which are major top-down national policies designed to restore and preserve ecosystem services (Liu et al. 2008). However, these programs had no provision regarding what human intervention was appropriate following natural disturbances. The scale of salvage logging within the ice storm region can be inferred from the changes of the 2008 logging quota approved by the State Forestry Administration of China for provinces to conduct salvage logging of forests impacted by the ice storm. Across the region, the logging quota jumped by 65% in 2008 (Figure 6.8). Salvage logging activities were observed in every county we visited. These activities appeared to be not well organized (Figure 6.9) and may have occurred even before the logging quota requests were filed. There was no direct information on how badly the logged forests were damaged by the ice storm. However some indirect evidence could be found from trees left at logging sites. Oleoresin tapping on pines (e.g. *Pinus massoniana* Lambert) is a common practice in the storm region (Zhou et al. 2011b). This technique creates a weak spot on tapped stems. Under heavy load of ice, pines whose stems had been excessively tapped for oleoresin tended to break right at the bark chipping spot. At logging sites, we often found standing pines with barks badly cut for oleoresin tapping, an indication that the damage caused by the ice storm was probably not very severe and salvage logging may not be justifiable (Figure 6.9b).

Salvage logging might have occurred preferentially in lightly to moderately impacted forests for several reasons even though we only had indirect evidence of this bias (Figure 6.9). Extensive stem breakage/splitting at various heights of severely impacted forests lowered the market value of their harvested timber relative to that of lightly to moderately impacted forests and so their appeal for logging. Also, the lightly to moderately impacted forests may have been more accessible for logging than those severely impacted, which tended to be located at higher elevations or on mountain tops (Zhou et al. 2011a; Shao et al. 2011). Note that the observed relationships (Figure 6.5) could not be explained by replanting of trees in severely impacted forests because the relationship emerged months to a year after the storm ended and regional-wide replanting could not be accomplished in such a short time. Without the intervening effect of salvage logging, the obtained nonlinear GRT-IS relationship may be quite different.

These findings and explanations need to be further validated through ground observations, e.g., eddy covariance measurements and chronosequences techniques (e.g., Amiro et al. 2010). They may be also region-specific (i.e. they may not be applicable to pure natural disturbances, which are difficult to find in places such as southern China). The carbon balance pre- and post-storm may be a more important way to reflect forest recovery than greenness. For carbon balance, spatial scaling is an important issue (Liu et al. 2011) and would require more work than conducted here. Some theoretical or empirical ecological models (Lindroth et al. 2009; Chambers et al. 2007) have been used to study storms; these models may be used to study the ice storm although they will need to explicitly consider human factors.

6.7. CONCLUSIONS

The rapid rebound of forest greenness after the massive 2008 ice storm in southern and central China will help the region's forests regain their carbon sink potential. The spatial and temporal patterns of forest greenness after the storm could be explained in the context of natural processes including species diversity, life-history strategy of trees, and gap-phase dynamics as well as human intervention, i.e., salvage logging, although further ground-based studies are needed to pinpoint the exact causes. Major findings from this study reflect the integrated effects of natural processes and human intervention and thus may not be applicable to pure natural disturbances. Nevertheless, the methodology developed may be equally effective to other destructive natural disturbances such as hurricanes, tornadoes and fires. Although remote sensing does not provide direct information about mechanisms controlling the impact dynamics of large extreme events, it can be used to construct the pre- and post-event spatial and temporal patterns of vegetation conditions, which can then be applied to test extant disturbance theories or develop new hypotheses to guide ground-based studies. To represent disturbance impact realistically, carbon cycle models may have to explicitly consider species that under normal conditions may not contribute much to forest primary production but are nevertheless important to the post-storm rebuilding of photosynthetic capacity. These models may also have to employ mechanisms (e.g. rapid mobilization of carbon reserves) to enable roles of life-history strategies of species (e.g. resprouting) in simulating post-disturbance vegetation dynamics. Potential human intervention must also be considered in these models. A close collaboration between the remote sensing community, experimental and theoretical ecologists, social scientists, and large-scale modelers is needed to advance the study of large extreme events and associated human intervention.

6.8. ACKNOWLEDGEMENTS

We thank Drs. V. H. Dale, P. J. Hanson, I. Fung, S. W. Running, G. Shao, M. Zhao and two anonymous reviewers for insightful comments, J. Chen for assistance in the freeze maps, C. Ai for help with logging quota, X. Wang for compiling meteorological data, and the Qianjiangyuan Forest Ecosystem Research Station for support of field work. The study was conducted at University of Texas, Austin and Oak Ridge National Laboratory (ORNL) with initial travel support from NASA Grant NNG09HP12I and subsequent support on research from NSF Grant ATM-0921898 and from U.S. Department of Energy (DOE), Office of Science. ORNL is managed by UT-Battelle, LLC, for the U.S. DOE under contract DE-AC05-00OR22725.

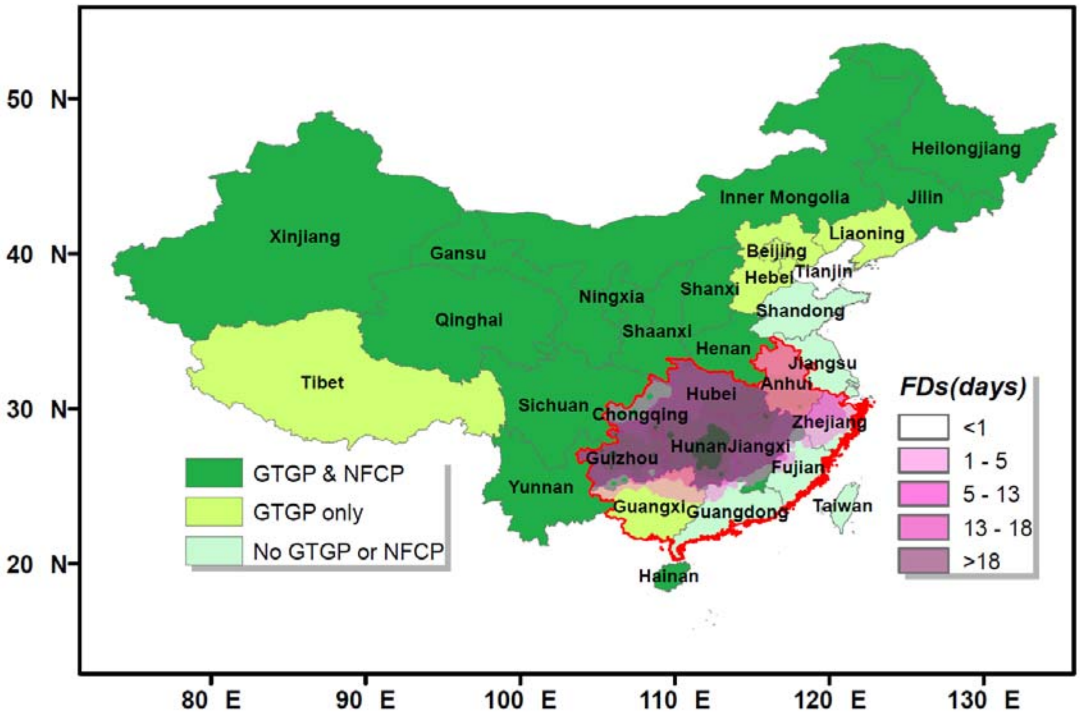

Figure 6.1. Spatial distribution of the number of freezing days (FDs) during the 2008 Chinese ice with the Natural Forest Conservation Program (NFCP) and the Grain to Green Program (GTGP) of China as the background.

The duration of the ice storm is from 10 January to 6 February 2008 (Chen and Sun 2010). The NFCP and GTGP map is reproduced from Liu et al. (2008). Red line delineates the domain of this study.

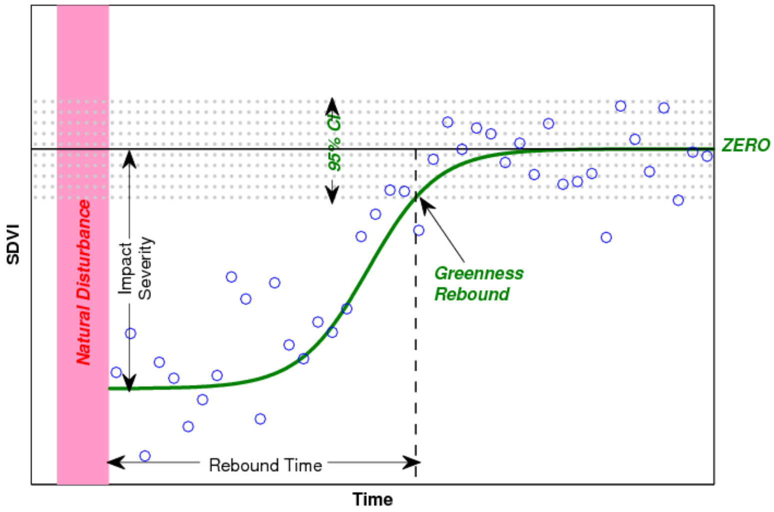

Figure 6.2. Objective determination of the impact severity (IS) and greenness rebound time (GRT).

The long-term time series of Standardized Detrended Vegetation Index (SDVI) of pre- and post-disturbance is used to establish its inter-annual variability - the 95% confidence interval (CI), which serves as a benchmark for both detecting the impacted pixels and determining their IS and GRT. A sigmoid function[*] is fit to the post-disturbance SDVI time series. The IS is measured by the reduction of SDVI from its long-term mean (zero), calculated with the optimized function at a time right after the disturbance. An impacted pixel has an IS value outside the 95% CI, and its greenness rebounds when the optimized curve crosses the CI lower threshold.

[*] Refer to Equation 6.5.

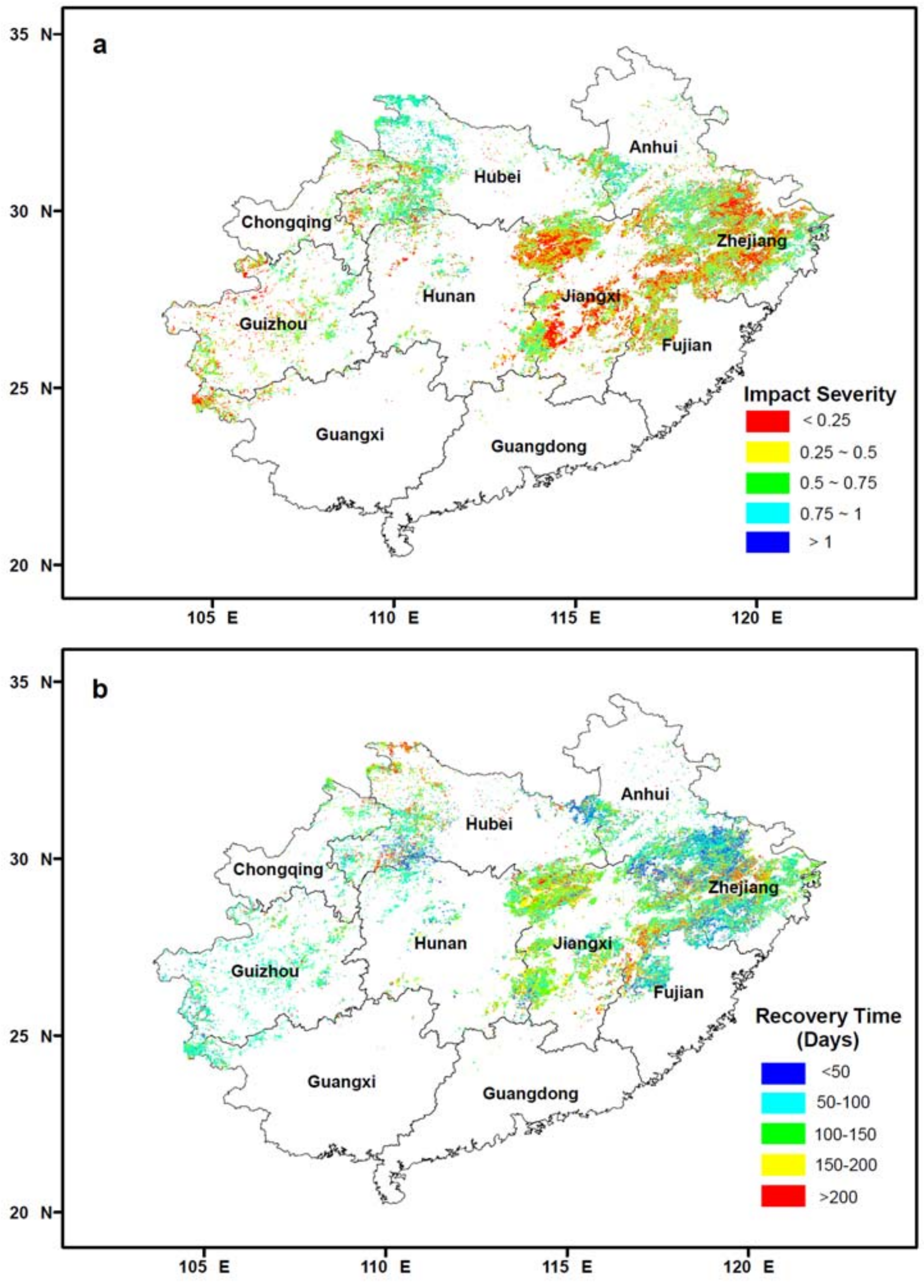

Figure 6.3. Spatial distribution of IS and GRT of impacted forests in areas with at least one freezing day.

Panel (a) the impact severity (IS) and (b) greenness rebound time (GRT).

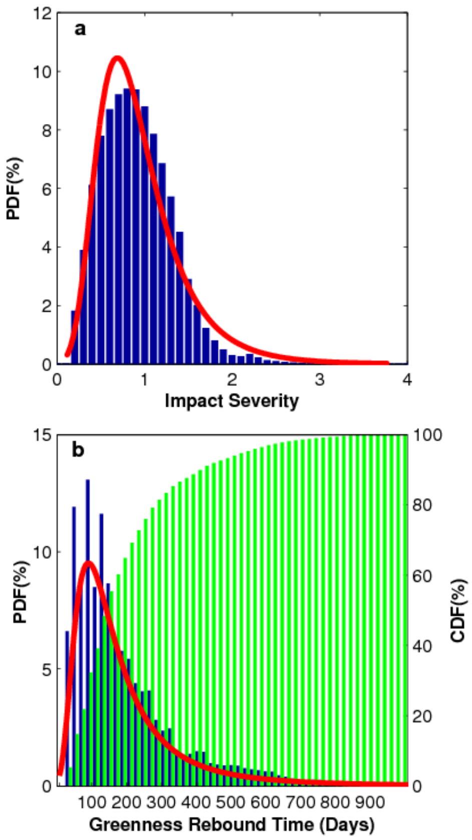

Figure 6.4. The probability density function (PDF) of IS and GRT.

Panel (a) impact severity and (b) greenness rebound time. Blue bars denote the spatial fraction of each bin, and the red curves represent the fitted PDF using a distribution of generalized extreme value. The cumulative distribution function (CDF) of greenness rebound time (green bars) is also shown in (b).

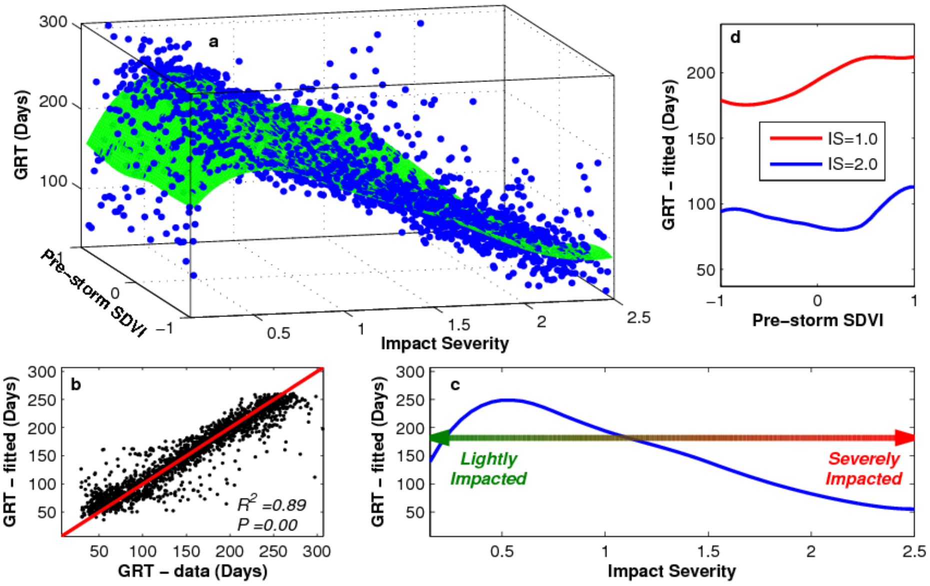

Figure 6.5. GRT as a function of IS and the mean SDVI for the main growing season prior to the storm (pre-storm SDVI).

Panel (a) The 3D scatter plot, surface-fitted with a local regression model (LOESS, green surface) with values of IS and pre-storm SDVI each binned at 0.05 intervals for clarity. (b) The goodness of surface fitting. (c) A slice in the GRT-IS plane at pre-storm SDVI = 0, showing GRT as a nonlinear function of IS. (d) A slice in the GRT - pre-storm SDVI plane at IS = 1.0 (red) and another at IS = 2.0 (blue), showing GRT as a nonlinear function of pre-storm SDVI.

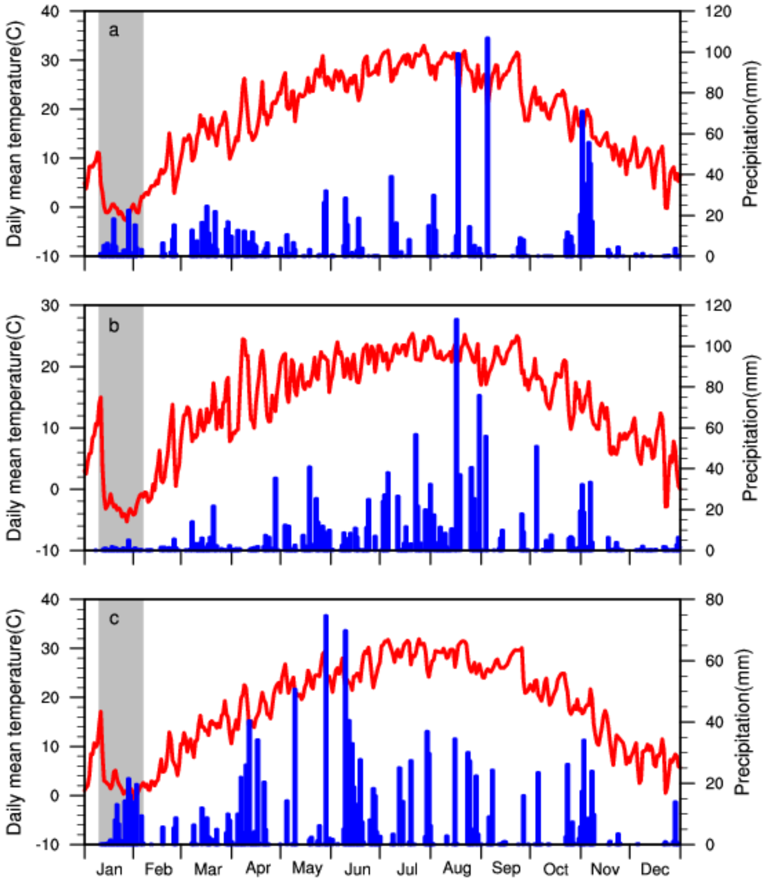

Figure 6.6. Daily mean surface temperature and precipitation accumulation of 2008 at the meteorological stations of Changsha, Guiyang, and Quzhou.

The daily mean surface temperature is shown in left ordinate (red curves) and precipitation accumulation shown in right ordinate (blue bars). Panel (a) Changsha (28°12'N, 112°58'E), (b) Guiyang (26°25'N, 106°44'E), and (c) Quzhou (28°58'N, 118°52'E). The shaded area indicates the occurrence of the ice storm.

Figure 6.7. Sprouts of fallen trees in the Nanling National Natural Reserve and the Jianglangshan Natural Reserve.

Pictures were taken at (a) the Nanling National Natural Reserve (24°55’N, 113°01’E) in the province of Guangdong, October 2008 and at (b) the Jianglangshan Natural Reserve (28°58’N, 118°52’E) in the province of Zhejiang, July 2010.

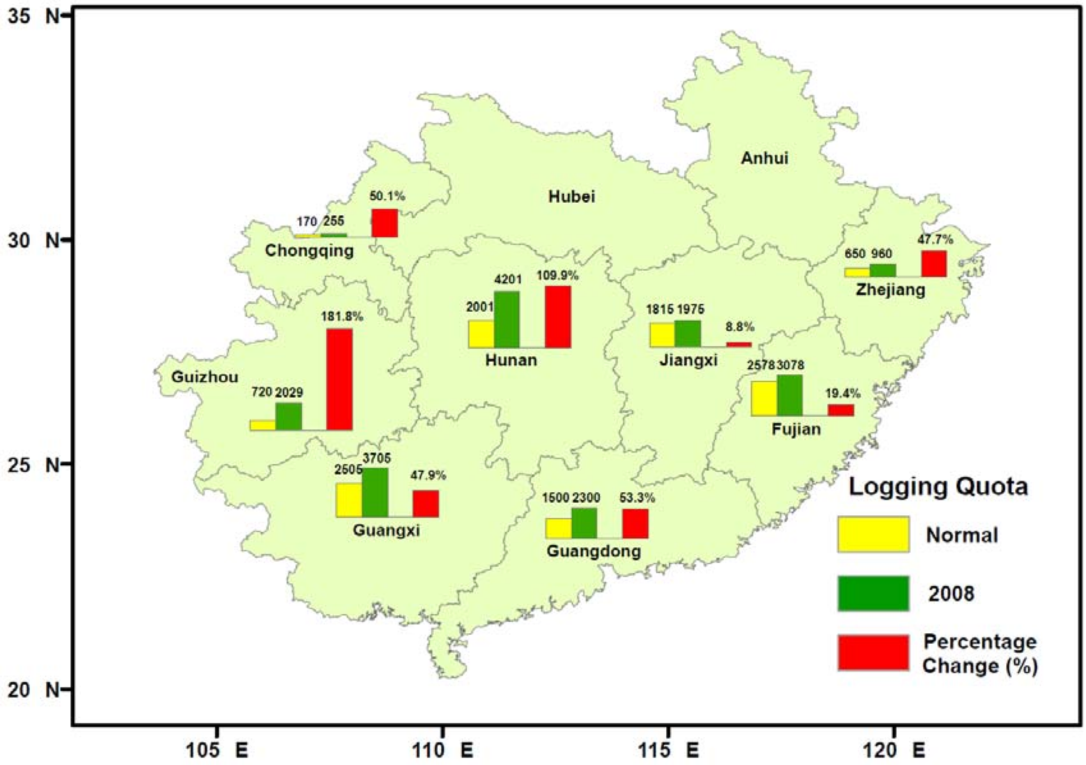

Figure 6.8. Changes of the 2008 logging quota approved by the State Forestry Administration of China for provinces to conduct salvage logging of forests impacted by the ice storm.

Yellow bars denote the originally planned annual quota ($\times 10^4$ m^3) for each province by the central government for the 11th five-year blueprint period (2006-2010); green bars denote the actual quota for 2008 to compensate for salvage logging. Red bars represent the percentage increase of the actual logging quota in 2008 over the originally planned. The central government's logging plan is reviewed every five years (complying with the five-year blueprint) and any unused quota rolls over from year to year during each five-year period. The provinces of Anhui and Hubei did not request for logging quota increase because the rollover of logging quota from previous years was sufficient to compensate for salvage logging. Data were provided by the State Forestry Administration of China.

Figure 6.9. Observed salvage logging in the aftermath of the ice storm.

The salvage logging was observed in Guiyang County, Hunan province on 28 April 2008. Note that a Masson's Pine (*Pinus massoniana* Lambert, B), whose bark was badly cut for oleoresin tapping, is still standing, indicating that ice load at this particular location was probably not very heavy and salvage logging may not be justifiable.

Chapter 7: Conclusions

7.1. SUMMARY

I have improved the plant physiology, ecology, and numerical treatments in the Community Land Model (CLM), one of the state-of-art land surface models for climate and carbon simulations. The research presented in Chapter 2, 3, 4 addresses the scientific questions related to the effects of mesophyll conductance of CO_2 inside leaves on global carbon cycles. I answered these questions by integrating leaf-level data analyses and modeling with global-scale simulations based on models I have developed or improved. Chapter 5 corrects a numerical deficiency with respect to the coupled calculations of photosynthesis and transpiration that has been overlooked previously by the land surface modeling community. Chapter 6 presents a quantitative framework to evaluate the impact of disturbances on ecosystems with a case study of the massive ice storm occurred in China in 2008. This framework sets a foundation for future representation of disturbances in large-scale models. The conclusions drawn, modeling framework developed, and general concepts proposed from this dissertation can be extended to other large-scale models for carbon cycle simulations. The research presented here informs potential avenues to reduce model uncertainties and to advance understanding carbon-climate coupling.

In an effort to integrate an explicit treatment of mesophyll conductance into LSMs in a way that is consistent with latest understanding of fundamental photosynthetic processes, I start with a meta-analysis of leaf-level gas exchanges measurements for C_3 plants to quantify the effect of mesophyll conductance on photosynthetic parameters and functional relationships among them (Chapter 2). The results show that the assumption of infinite value of g_m, which is commonly used by current LSMs, leads to substantial underestimation of key parameters in the photosynthesis model, i.e., V_{cmax} (up to 75%), J_{max} (up to 60%), and TPU (up to 40%). The three parameters show varying sensitivities to g_m variations (V_{cmax} the most and TPU the least). Because of such differential sensitivity, a biased estimation of interdependences among these parameters would occur under the assumption of infinite g_m with the net consequence of overestimating the slope between J_{max} and V_{cmax} and that between TPU and J_{max}. Moreover, this assumption limits the freedom of variation of estimated parameters and artificially constrains parameter relationships to stronger couplings. I further find a nonlinear model to link the parameters estimated under the infinite g_m assumption ("apparent" parameters) to proper values if an estimated g_m is available ("true" parameters), which can be applied to large-scale carbon cycle modeling. This research is reliant on extensive measurements worldwide and so provides a benchmark to quantify how g_m shapes photosynthetic parameters, and further paves ways for recalibration of parameters in LSMs that are compatible with g_m inclusion. To my knowledge, it is the first time such an analysis has been done.

Chapter 3 present a simple but realistic parameterization of g_m based on the synthesis of new advances in plant physiological studies. In this formulation, g_m is calculated from its association with plant functional types and its dependence on environmental conditions. We implement this parameterization in the Community Land Model version 4a (CLM4a), a representative land component of climate models. We also recalibrate the key photosynthetic parameters to maintain the consistency between model structure and associated parameters. To my knowledge, it is the first time a global mesophyll conductance model has been developed and implemented in a global land surface model. With the modified CLM4a, we investigate the impact of g_m on the global terrestrial gross primary production (GPP). Our simulations show that the inclusion of g_m slightly increases the estimated mean global annual GPP over the period of 1982-2004 by

~9 Pg C yr^{-1}. This increase in GPP is throughout the globe but particularly large in the tropics. We further found that omission of the mesophyll diffusion process can underestimate the potential of GPP stimulation to rising atmospheric CO_2. The trend of such discrepancy is about 27 Pg C y^{-1} per 1000 ppm, with the tropics playing the major role. This systematic trend is strongly influenced by climate variability. This study provides a benchmark to demonstrate the role of g_m in terrestrial carbon simulations at global scales.

With the global g_m modeling framework and benchmark simulations in Chapter 3, Chapter 4 quantifies the global consequence of g_m to the CO_2 fertilization effect on GPP. This underestimation occurs because tuned apparent parameters do not represent the underlying properties of limiting biochemical processes and they only work phenomenologically for narrow measurement conditions. From 1850 to 2004, the global gross primary production may be underestimated by a cumulative total of 113 to 148 Pg C, a magnitude equivalent to one full year's gross photosynthesis of the global terrestrial biosphere or to the entire global fossil CO_2 emissions from 1850 to the mid-1970s. The terrestrial biosphere may be more CO_2-limited and absorb more carbon with increased atmospheric CO_2 concentrations than previously thought.

Along the way to implement the global mesophyll conductance model in CLM4a, I serendipitously found a numerical "instability" of CLM in its iterative calculations of photosynthesis in the coupled photosynthesis-stomatal conductance model. Chapter 5 analyzes the cause of this issue and proposes a solution. The results demonstrate that the fixed-point iteration approach used to solve the coupled model cannot ensure convergence because a strict mathematical requirement, i.e., the fixed-point theorem, is violated. This iteration fails more frequently in some regions of the world than in others, leading to regionally varying uncertainty and global biases in the estimated carbon and water fluxes. Further, an artificial constraint to the water vapor pressure of canopy air was applied in CLM in its calculations of photosynthesis and stomatal conductance, which are shown to bias GPP and transpiration simulations. I designed a Newton-Raphson iteration scheme to replace the fixed-point approach and show that this new approach can ensure convergence, does not require an artificial constraint on the atmospheric water vapor pressure, and is computationally efficient. Finally, I estimate the global and regional bias arising from this numerical error and suggest replacement of the current fixed-point treatment in CLM, e.g., Newton-Raphson approach, and removal of the artificial constraint on the atmospheric water vapor pressure. To my knowledge, the CLM working group has a plan to adopt my recommendations in their future release of CLM model versions.

Chapter 6 presents a case study on the dynamic impact of a disturbance, the massive 2008 Chinese ice storm, by integrating a quantitative modeling framework, satellite observations of forest greenness, and ground measurements. I find that the greenness of forests rebounded surprisingly fast after the storm and that higher pre-storm vegetation growth corresponded to slower rebound of post-storm greenness. In particular, rebound of greenness was slowest in forests that were moderately impacted by the storm, resulting in a nonlinear relationship between greenness rebound time and the impact severity by the storm. Ground investigation revealed that the overall quick rebound of greenness is a consequence of resprouting of physically damaged trees and regrowth of understory vegetation. These biotic mechanisms also benefited from favorable post-storm environmental conditions, e.g., high temperature and sufficient moisture. The counterintuitive non-linear pattern between greenness rebound time and the storm impact severity was most likely attributable to the salvage logging, which may have selectively targeted lightly to moderately impacted forests due to their higher economic values and accessibility. The salvage logging adversely affected the greenness rebound of the damaged forests. Although gap-phase dynamics could have played a role in the faster rebound of severe damaged vegetation, it cannot explain the initial increase of the rebound time needed against the impact severity. This study demonstrates the integrated effects of large disturbance events and human intervention on forest ecosystems, which are often ignored in disturbance research. The framework developed can serve as the benchmark to objectively determine and quantify the dynamic impact of disturbances and help attribute the consequences to natural and anthropogenic factors.

7.2. FUTURE RESEARCH DIRECTIONS

Although I believe I have answered many scientific questions, more questions have been raised in nearly all segments of my dissertation research. With regards to studies on mesophyll conductance, I employ a simple modeling framework to represent the dependence of g_m on leaf traits and environmental conditions to obtain reliability for global simulations. However, more areas need to be explored, including:

1. Modeling of mesophyll conductance can be further improved in multiple ways. First, environmental modifiers in addition to temperature and moisture, e.g., salinity, ozone, seem also critical to regulate the magnitude of mesophyll conductance, but are not included in the current formulation. This is because these environmental influences have been much less quantified in process-based studies. Further refinement of the g_m model can be done as new advances in field studies emerge. Second, g_m not only responds to short-term variation but also acclimates to long-term changes of climate, in particular, temperature. The effect of the former has been embedded in the temperature response function in the g_m model; yet the latter is not accounted for. It is interesting to perform some

sensitivity tests to examine the long-term acclimation effect on g_m. Third, the parameter recalibration in current research relies on an empirical conversion function, though reasonable, it is an indirect way to formulate. More analyses can be done to link the "true" photosynthetic parameters, especially, V_{cmax}, to leaf traits, and thus to improve the linkage to carbon models.

2. Model validations are performed at a global scale, with statistical up-scaled flux measurements. More validation work is desirable at individual flux sites, with site-specific meteorological forcings. In this regard, photosynthetic parameters need to be finely tuned to accommodate to ecosystem specifics at each site.
3. Studies using flux data have found that mesophyll conductance imposes stronger limitations on productivity under drought stress. This arises from the regulation by soil moisture of the magnitude of mesophyll conductance. Mesophyll conductance can also modify water use efficiency to influence productivity (Keenan et al. 2010a). However, it is not clear whether models can do a reasonable job to simulate drought-induced reduction of GPP if mesophyll conductance is explicitly considered. This is an interesting direction to further pursue.
4. The ultimate objective of the mesophyll study is to determine to what extent it can influence the carbon sink strength and hence the atmospheric CO_2 concentration. Current Community Earth System Model (CESM) used in IPCC AR5 is found to underestimate the historical CO_2 trend by the same magnitude as to what I found in Chapter 4 (*Hoffman*, personal communication). I will perform fully coupled Earth System Model simulations with ocean, atmosphere, and sea-ice module all active, and with g_m considered, to test if this model can improve the simulation of the historical trend of atmospheric CO_2. A related question is whether the model

with g_m can simulate a reasonable seasonal cycle of atmospheric CO_2 if g_m is explicitly considered, the magnitude of which is currently underestimated. A further intriguing issue is can g_m influence carbon storage simulations in the future and if so, by how much? And also can mesophyll conductance modify carbon-climate feedbacks, regionally and globally?

In terms of the disturbance study, only one case study was conducted and more disturbance events can be applied to the conceptual framework to test its applicability and effectiveness. More promising research that can be done along this direction is:

1. I will incorporate this framework into CLM, to simulate the accumulated effects of historical disturbances on ecosystems. At present, only fires are dynamically simulated in the general framework of CLM, but representation of other disturbance agents is lacking. This is on the one hand, due to relatively smaller impacts and longer return frequency of other types of disturbance, and on the other, to highly diverse features of different events and hence it is infeasible to generically represent all of them. The framework developed in this dissertation is a unified approach, which can potentially be applied to various types of extreme events and disturbances and hence integrated into large-scale carbon models. The global effect of occurrence of individual disturbance may be minor, but the accumulated impacts over history may account for a large portion of CO_2 emission into atmosphere. Given the high possibility of more frequent occurrences of disturbances and extremes in the future, this framework can provide a benchmark for predicting dynamical impacts of disturbance.
2. Another interesting direction to explore is to develop historical disturbance indices using a modeling framework. Satellite products provide long-term, high-resolution observations for land, including vegetation indices, land cover change,

and albedo, etc. These are proxies of disturbance legacy and thus capable of capturing infrequently occurring and diverse episodes of disturbance. These dataset can be individually or jointly applied into the generic framework to construct large-scale and historical disturbance indices.

References

Allan, E., W. Weisser, A. Weigelt, C. Roscher, M. Fischer, and H. Hillebrand, 2011: More diverse plant communities have higher functioning over time due to turnover in complementary dominant species. *Proc. Natl. Acad. Sci. U. S. A.*, **108**, 1–6, doi:10.1073/pnas.1104015108.

Allen, C. D., and D. D. Breshears, 1998: Drought-induced shift of a forest–woodland ecotone: Rapid landscape response to climate variation. *Proc. Natl. Acad. Sci. U. S. A.*, **95**, 14839–14842.

Amiro, B. D. and Coauthors, 2010: Ecosystem carbon dioxide fluxes after disturbance in forests of North America. *J. Geophys. Res.*, **115**, G00K02, doi:10.1029/2010JG001390.

Angert, A., S. Biraud, C. Bonfils, W. Buermann, and I. Fung, 2004: CO 2 seasonality indicates origins of post-Pinatubo sink. *Geophys. Res. Lett.*, **31**, 1999–2002, doi:10.1029/2004GL019760.

Aubinet, M. ., T. Vesala, and D. Papale, 2012: *Eddy Covariance: A Pratical Guide to Measurement and Data Analysis*. Springer, Dordrecht, Netherlands,.

Bacastow, R., and C. D. Keeling, 1973: Atmospheric carbon dioxide and radiocarbon in the natural carbon cycle: II. Changes from A.D. 1700–2070 as deduced from a geochemical model. *Carbon and the biosphere* , Eds. G.M. Woodwell and E. V. Pecan, 86– 135, U.S. Department of Commerce, Springfield.

Baldocchi, D., 1994: An analytical solution for coupled leaf photosynthesis and stomatal conductance models. *Tree Physiol.*, **14**, 1069–1079, doi:10.1093/treephys/14.7-8-9.1069.

Ball, J. T., I. E. Woodrow, and J. A. Berry, 1987: A model predicting stomatal conductance and its contribution to the control of photosynthesis under different environmental conditions. *Progress in Photosynthesis Research*, Ed. J. Biggins, Vol. 4 of, 221–224, Martinus Nijhoff, Dordrecht, Netherlands.

Ballantyne, A. P., C. B. Alden, J. B. Miller, P. P. Tans, and J. W. C. White, 2012: Increase in observed net carbon dioxide uptake by land and oceans during the past 50 years. *Nature*, **488**, 70–72, doi:10.1038/nature11299.

Beer, C. and Coauthors, 2010: Terrestrial Gross Carbon Dioxide Uptake: Global Distribution and Covariation with Climate. *Science*, **329**, 834–838, doi:10.1126/science.1184984.

Bernacchi, C. J., A. R. Portis, H. Nakano, S. von Caemmerer, and S. P. Long, 2002: Temperature response of mesophyll conductance: Implications for the determination of Rubisco enzyme kinetics and for limitations to photosynthesis in vivo. *Plant Physiol.*, **130**, 1992–1998, doi:Doi 10.1104/Pp.008250.

Boden, T. A., G. Marland, and R. J. Andres, 2010: *Global, Regional, and National Fossil-Fuel CO2 Emissions*. Carbon Dioxide Information Analysis Center, Oak Ridge National Laboratory, U.S. Department of Energy, Oak Ridge, Tenn., U.S.A.,.

Bonan, G., 2008a: Carbon cycle: Fertilizing change. *Nat. Geosci.*, **1**, 645–646, doi:10.1038/ngeo328.

Bonan, G., 2008b: Disturbances and landscapes. *Ecological climatology: Concepts and Applications*, 347–363, Cambridge University Press, Cambridge.

Bonan, G. B., and S. Levis, 2010: Quantifying carbon-nitrogen feedbacks in the Community Land Model (CLM4). *Geophys. Res. Lett.*, **37**, L07401, doi:10.1029/2010GL042430.

Bonan, G. B., P. J. Lawrence, K. W. Oleson, S. Levis, M. Jung, M. Reichstein, D. M. Lawrence, and S. C. Swenson, 2011: Improving canopy processes in the Community Land Model version 4 (CLM4) using global flux fields empirically inferred from FLUXNET data. *J. Geophys. Res.*, **116**, G02014, doi:10.1029/2010JG001593.

Bonan, G. B., K. W. Oleson, R. A. Fisher, G. Lasslop, and M. Reichstein, 2012: Reconciling leaf physiological traits and canopy flux data: Use of the TRY and FLUXNET databases in the Community Land Model version 4. *J. Geophys. Res.*, **117**, G02026.

Bonan, G. B., M. D. Hartman, W. J. Parton, and W. R. Wieder, 2013: Evaluating litter decomposition in earth system models with long-term litterbag experiments: an example using the Community Land Model version 4 (CLM4). *Glob. Change Biol.*, **19**, 957–974.

Brantley, S. T., J. C. Zinnert, and D. R. Young, 2011: Application of hyperspectral vegetation indices to detect variations in high leaf area index temperate shrub thicket canopies. *Remote Sens. Environ.*, **115**, 514–523, doi:10.1016/j.rse.2010.09.020.

Burden, R. L., and J. D. Faires, 2011: *Numerical Analysis*. 9th ed. BROOKS/COLE CENGAGE Learning, Boston,.

Busch, F. A., T. L. Sage, A. B. Cousins, and R. F. Sage, 2013: C3 plants enhance rates of photosynthesis by reassimilating photorespired and respired CO2. *Plant Cell Environ.*, **36**, 200–212.

von Caemmerer, S., 2000: *Biochemical Models of Leaf Photosynthesis, Techniques in Plant Sciences* . 2nd ed. CSIRO Publishing, Collingwood, Australia,.

von Caemmerer, S., and J. R. Evans, 2010: Enhancing C3 Photosynthesis. *Plant Physiol.*, **154** , 589–592.

Cai, T., L. B. Flanagan, R. S. Jassal, and T. A. Black, 2008: Modelling environmental controls on ecosystem photosynthesis and the carbon isotope composition of ecosystem-respired CO2 in a coastal Douglas-fir forest. *Plant Cell Environ.*, **31**, 435–453.

Canadell, J. G. and Coauthors, 2007: Contributions to accelerating atmospheric CO2 growth from economic activity, carbon intensity, and efficiency of natural sinks. *Proc. Natl. Acad. Sci. U. S. A.*, **104**, 18866–18870.

Chambers, J. Q., J. I. Fisher, H. Zeng, E. L. Chapman, D. B. Baker, and G. C. Hurtt, 2007: Hurricane Katrina's carbon footprint on U.S. Gulf Coast forests. *Science*, **318**, 1107.

Changnon, S. A., 2003: Characteristics of Ice Storms in the United States. *J. Appl. Meteorol.*, **42**, 630–639, doi:10.1175/1520-0450(2003)042<0630:COISIT>2.0.CO;2.

Chazen, O., and P. M. Neumann, 1994: Hydraulic signals from the roots and rapid cell-wall hardening in growing maize (Zea mays L.) leaves are primary responses to polyethylene glycol-induced water deficits. *Plant Physiol.*, **104**, 1385–1392.

Chen, H. S., R. E. Dickinson, Y. J. Dai, and L. M. Zhou, 2011: Sensitivity of simulated terrestrial carbon assimilation and canopy transpiration to different stomatal conductance and carbon assimilation schemes. *Clim. Dyn.*, **36**, 1037–1054, doi:DOI 10.1007/s00382-010-0741-2.

Chen, J., and L. Sun, 2010: Using MODIS EVI to detect vegetation damage caused by the 2008 ice and snow storms in south China. *J. Geophys. Res.*, **115**, G00H04, doi:10.1029/2009JG001246.

Ciais, P. and Coauthors, 2005: Europe-wide reduction in primary productivity caused by the heat and drought in 2003. *Nature* , **437**, 529–533.

Collatz, G. J., J. T. Ball, C. Grivet, and J. A. Berry, 1991: Physiological and environmental regulation of stomatal conductance, photosynthesis and transpiration: a model that includes a laminar boundary layer. *Agric. For. Meteorol.*, **54**, 107–136, doi:10.1016/0168-1923(91)90002-8.

Collatz, G. J., M. Ribas-Carbo, and J. A. Berry, 1992: Coupled photosynthesis-stomatal conductance model for leaves of C4 plants. *Aust. J. Plant Physiol.*, **19**, 519–538.

Connell, J. H., 1978: Diversity in tropical rain forests and coral reefs. *Science*, **199**, 1302–1310.

Cox, P. M., R. A. Betts, C. D. Jones, S. A. Spall, and I. J. Totterdell, 2000: Acceleration of global warming due to carbon-cycle feedbacks in a coupled climate model. *Nature*, **408**, 184–187.

Cramer, W. and Coauthors, 2001: Global response of terrestrial ecosystem structure and function to CO 2 and climate change: results from six dynamic global vegetation models. *Glob. Change Biol.*, **7**, 357–373, doi:10.1046/j.1365-2486.2001.00383.x.

Dai, Y., R. E. Dickinson, and Y.-P. Wang, 2004: A Two-Big-Leaf Model for Canopy Temperature, Photosynthesis, and Stomatal Conductance. *J. Clim.*, **17**, 2281–2299, doi:10.1175/1520-0442(2004)017<2281:ATMFCT>2.0.CO;2.

Dale, V. H., C. M. Crisafulli, and F. J. Swanson, 2005: Ecology. 25 years of ecological change at Mount St. Helens. *Science*, **308**, 961–962.

Denman, K. L. and Coauthors, 2007: Couplings Between Changes in the Climate System and Biogeochemistry. *Climate Change 2007: The Physical Science Basis. Contribution of Working Group I to the Fourth Assessment Report of the Intergovernmental Panel on Climate Change*, Eds. S. Solomon, D. Qin, M. Manning, Z. Chen, M. Marquis, K.B. Averyt, M. Tignor, and H.L. Miller, Vol. 21 of, 499–587, Cambridge University Press, Cambridge, United Kingdom and New York, NY, USA.

Dickinson, R. E., 2012: Interaction Between Future Climate and Terrestrial Carbon and Nitrogen. *The Future of the World's Climate*, Eds. A. Henderson-Sellers and K. McGuffie, 289–308, Elsevier B.V., Oxford, UK.

Dickinson, R. E., A. Henderson-Sellers, and P. J. Kennedy, 1993: Biosphere-Atmosphere Transfer Scheme (BATS) version 1e as coupled to the NCAR Community Climate Model. *NCAR Tech. Note*, **TN-387+STR**, 1–72.

Dickinson, R. E. and Coauthors, 2002: Nitrogen Controls on Climate Model Evapotranspiration. *J. Clim.*, **15**, 278–295, doi:10.1175/1520-0442(2002)015<0278:NCOCME>2.0.CO;2.

Donato, D. C., J. B. Fontaine, J. L. Campbell, W. D. Robinson, J. B. Kauffman, and B. E. Law, 2006: Post-wildfire logging hinders regeneration and increases fire risk. *Science*, **311**, 352.

Dubois, J.-J. B., E. L. Fiscus, F. L. Booker, M. D. Flowers, and C. D. Reid, 2007: Optimizing the statistical estimation of the parameters of the Farquhar-von Caemmerer-Berry model of photosynthesis. *New Phytol.*, **176**, 402–414.

Duffy, J. E., 2009: Why biodiversity is important to the functioning of real-world ecosystems. *Front. Ecol. Environ.*, **7**, 437–444, doi:10.1890/070195.

Egea, G., A. Verhoef, and P. L. Vidale, 2011: Towards an improved and more flexible representation of water stress in coupled photosynthesis-stomatal conductance models. *Agric. For. Meteorol.*, **151**, 1370–1384, doi:DOI 10.1016/j.agrformet.2011.05.019.

Ehleringer, J. R., and T. E. Cerling, 1995: Atmospheric CO 2 and the ratio of intercellular to ambient CO 2 concentrations in plants. *Tree Physiol.*, **15**, 105–111.

Ellsworth, D. S., P. B. Reich, E. S. Naumburg, G. W. Koch, M. E. Kubiske, and S. D. Smith, 2004: Photosynthesis, carboxylation and leaf nitrogen responses of 16 species to elevated pCO2 across four free-air CO2 enrichment experiments in forest, grassland and desert. *Glob. Change Biol.*, **10**, 2121–2138.

Ethier, G. J., and N. J. Livingston, 2004: On the need to incorporate sensitivity to CO2 transfer conductance into the Farquhar-von Caemmerer-Berry leaf photosynthesis model. *Plant Cell Environ.*, **27**, 137–153, doi:10.1111/j.1365-3040.2004.01140.x.

Ethier, G. J., N. J. Livingston, D. L. Harrison, T. A. Black, and J. A. Moran, 2006: Low stomatal and internal conductance to CO2 versus Rubisco deactivation as determinants of the photosynthetic decline of ageing evergreen leaves. *Plant Cell Environ.*, **29**, 2168–2184, doi:10.1111/j.1365-3040.2006.01590.x.

Evans, J. R., and S. von Caemmerer, 2013: Temperature response of carbon isotope discrimination and mesophyll conductance in tobacco. *Plant Cell Environ.*, **36**, 745–756.

Evans, J. R., T. D. Sharkey, J. A. Berry, and G. D. Farquhar, 1986: Carbon isotope discrimination measured concurrently with gas-exchange to investigate CO2 diffusion in leaves of higher-plants. *Aust. J. Plant Physiol.*, **13**, 281–292.

Evans, J. R., R. Kaldenhoff, B. Genty, and I. Terashima, 2009: Resistances along the CO2 diffusion pathway inside leaves. *J. Exp. Bot.*, **60**, 2235–2248.

Farquhar, G. D., and S. von Caemmerer, 1982: Modelling of photosynthetic responses to environmental conditions. *Physiological plant ecology. II. Encyclopedia of plant physiology*, Eds. O. Lange, P. Nobel, C. Osmond, and H. Ziegler, 550–587, Springer Verlag, Heidelberg.

Farquhar, G. D., S. von Caemmerer, and J. A. Berry, 1980: A Biochemical-model of Photosynthetic Co2 Assimilation in Leaves of C-3 Species. *Planta*, **149**, 78–90.

Fisher, J., J. Mustard, and M. Vadeboncoeur, 2006: Green leaf phenology at Landsat resolution: Scaling from the field to the satellite. *Remote Sens. Environ.*, **100**, 265–279, doi:10.1016/j.rse.2005.10.022.

Flexas, J., M. Ribas-Carbó, A. Diaz-Espejo, J. Galmés, and H. Medrano, 2008: Mesophyll conductance to CO2: current knowledge and future prospects. *Plant Cell Environ.*, **31**, 602–621.

Flexas, J. and Coauthors, 2012: Mesophyll diffusion conductance to CO2: An unappreciated central player in photosynthesis. *Plant Sci.*, **193–194**, 70–84, doi:10.1016/j.plantsci.2012.05.009.

Foster, D. R., J. D. Aber, J. M. Melillo, R. D. Bowden, and F. A. Bazzaz, 1997: Forest response to disturbance and anthropogenic stress. *BioScience*, **47**, 437–445, doi:10.2307/1313059.

Fox, J. W., 2012: The intermediate disturbance hypothesis should be abandoned. *Trends Ecol. Evol.*, **28**, 86–92.

Franklin, J. F., H. H. Shugart, and M. E. Harmon, 1987: Tree Death as an Ecological Process. *BioScience*, **37**, 550–556, doi:10.2307/1310665.

Friedl, M. A. and Coauthors, 2002: Global land cover mapping from MODIS: algorithms and early results. *Remote Sens. Environ.*, **83**, 287–302, doi:10.1016/S0034-4257(02)00078-0.

Friedlingstein, P. and Coauthors, 2006: Climate-carbon cycle feedback analysis: Results from the C4MIP model intercomparison. *J. Clim.*, **19**, 3337–3353, doi:10.1175/jcli3800.1.

Frolking, S., M. W. Palace, D. B. Clark, J. Q. Chambers, H. H. Shugart, and G. C. Hurtt, 2009: Forest disturbance and recovery: A general review in the context of spaceborne remote sensing of impacts on aboveground biomass and canopy structure. *J. Geophys. Res.*, **114**, G00E02, doi:10.1029/2008JG000911.

Fung, I. Y., S. C. Doney, K. Lindsay, and J. John, 2005: Evolution of carbon sinks in a changing climate. *Proc. Natl. Acad. Sci. U. S. A.*, **102**, 11201–11206.

Girardin, M. P., A. A. Ali, C. Carcaillet, M. Mudelsee, I. Drobyshev, C. HÉly, and yves Bergeron, 2009: Heterogeneous response of circumboreal wildfire risk to climate change since the early 1900s. *Glob. Change Biol.*, **15**, 2751–2769.

Goetz, S., G. Fiske, and A. Bunn, 2006: Using satellite time-series data sets to analyze fire disturbance and forest recovery across Canada. *Remote Sens. Environ.*, **101**, 352–365, doi:10.1016/j.rse.2006.01.011.

Gu, L., D. D. Baldocchi, S. C. Wofsy, J. W. Munger, J. J. Michalsky, S. P. Urbanski, and T. A. Boden, 2003a: Response of a deciduous forest to the Mount Pinatubo eruption: enhanced photosynthesis. *Science*, **299**, 2035–2038.

Gu, L., W. M. Post, D. D. Baldocchi, T. A. Black, S. B. Verma, T. Vesala, and S. C. Wofsy, 2003b: Phenology of Vegetation Photosynthesis. *Phenology: An integrated environmental science*, Ed. M.D. Schwartz, p. 592, Kluwer Academic Publishers, Dordrecht, the Netherlands.

Gu, L. and Coauthors, 2006: Direct and indirect effects of atmospheric conditions and soil moisture on surface energy partitioning revealed by a prolonged drought at a temperate forest site. *J. Geophys. Res.*, **111**, D16102, doi:10.1029/2006JD007161.

Gu, L., P. J. Hanson, W. Mac Post, D. P. Kaiser, B. Yang, R. Nemani, S. G. Pallardy, and T. Meyers, 2008: The 2007 Eastern US Spring Freeze: Increased Cold Damage in a Warming World. *BioScience*, **58**, 253, doi:10.1641/B580311.

Gu, L., W. M. Post, D. D. Baldocchi, T. A. Black, A. E. Suyker, S. B. Verma, T. Vesala, and S. C. Wofsy, 2009: Characterizing the Seasonal Dynamics of Plant

Community Photosynthesis Across a Range of Vegetation Types. *Phenology of ecosystem processes: Applications in global change research*, Ed. A. Noormets, 35–58, Springer New York.

Gu, L., S. G. Pallardy, K. Tu, B. E. Law, and S. D. Wullschleger, 2010: Reliable estimation of biochemical parameters from C3 leaf photosynthesis-intercellular carbon dioxide response curves. *Plant Cell Environ.*, **33**, 1852–1874, doi:10.1111/j.1365-3040.2010.02192.x.

Gulden, L. E., E. Rosero, Z.-L. Yang, T. Wagener, and G.-Y. Niu, 2008: Model performance, model robustness, and model fitness scores: A new method for identifying good land-surface models. *Geophys. Res. Lett.*, **35**, L11404.

Gutschick, V. P., and H. BassiriRad, 2003: Extreme events as shaping physiology, ecology, and evolution of plants: toward a unified definition and evaluation of their consequences. *New Phytol.*, **160**, 21–42, doi:10.1046/j.1469-8137.2003.00866.x.

Han, Q., A. Iio, M. Naramoto, and Y. Kakubari, 2010: Response of internal conductance to soil drought in sun and shade leaves of adult. *Acta Silv. Lign. Hung.*, **6**, 123–134.

Hanba, Y. T., H. Kogami, and I. Terashima, 2002: The effect of growth irradiance on leaf anatomy and photosynthesis in Acer species differing in light demand. *Plant Cell Environ.*, **25**, 1021–1030.

Harley, P. C., F. Loreto, G. Dimarco, and T. D. Sharkey, 1992: Theoretical Considerations When Estimating the Mesophyll Conductance to Co2 Flux by Analysis of the Response of Photosynthesis to Co2. *Plant Physiol.*, **98**, 1429–1436.

Hikosaka, K., 2005: Nitrogen partitioning in the photosynthetic apparatus of Plantago asiatica leaves grown under different temperature and light conditions: Similarities and differences between temperature and light acclimation. *Plant Cell Physiol.*, **46**, 1283–1290.

Hubbell, S. P., 1999: Light-Gap Disturbances, Recruitment Limitation, and Tree Diversity in a Neotropical Forest. *Science*, **283**, 554–557, doi:10.1126/science.283.5401.554.

Huete, A., K. Didan, T. Miura, E. P. Rodriguez, X. Gao, and L. G. Ferreira, 2002: Overview of the radiometric and biophysical performance of the MODIS vegetation indices. *Remote Sens. Environ.*, **83**, 195–213, doi:10.1016/S0034-4257(02)00096-2.

Huete, A., K. Didan, W. van Leeuwen, T. Miura, and E. Glenn, 2011: MODIS Vegetation Indices. *Land Remote Sensing and Global Environmental Change*, Eds. B. Ramachandran, C.O. Justice, and M.J. Abrams, 579–602, Springer Science+Business Media LLC.

Huete, A. R. and Coauthors, 2006: Amazon rainforests green-up with sunlight in dry season. *Geophys. Res. Lett.*, **33**, L06405, doi:10.1029/2005GL025583.

Hughes, A. R., J. E. Byrnes, D. L. Kimbro, and J. J. Stachowicz, 2007: Reciprocal relationships and potential feedbacks between biodiversity and disturbance. *Ecol. Lett.*, **10**, 849–864, doi:10.1111/j.1461-0248.2007.01075.x.

Isbell, F. and Coauthors, 2011: High plant diversity is needed to maintain ecosystem services. *Nature*, **477**, 199–202, doi:10.1038/nature10282.

Jarque, C. M., and A. K. Bera, 1987: A test for normality of observations and regression residuals. *Int. Stat. Rev.*, **55**, 163–172.

Jentsch, A., J. Kreyling, and C. Beierkuhnlein, 2007: A new generation of climate-change experiments: events, not trends. *Front. Ecol. Environ.*, **5**, 365–374.

Kattge, J., W. Knorr, T. Raddatz, and C. Wirth, 2009: Quantifying photosynthetic capacity and its relationship to leaf nitrogen content for global-scale terrestrial biosphere models. *Glob. Change Biol.*, **15**, 976–991, doi:10.1111/j.1365-2486.2008.01744.x.

Keeling, C. D., T. P. Whorf, M. Wahlen, and J. Van Der Plichtt, 1995: Interannual extremes in the rate of rise of atmospheric carbon dioxide. *Nature*, **375**, 666–670.

Keeling, R. F., S. C. Piper, and M. Heimann, 1996: Global and hemispheric CO2 sinks deduced from changes in atmospheric O2 concentration. *Nature*, **381**, 218–221, doi:10.1038/381218a0.

Keenan, T., S. Sabate, and C. Gracia, 2010a: Soil water stress and coupled photosynthesis-conductance models: Bridging the gap between conflicting reports on the relative roles of stomatal, mesophyll conductance and biochemical limitations to photosynthesis. *Agric. For. Meteorol.*, **150**, 443–453, doi:DOI 10.1016/j.agrformet.2010.01.008.

Keenan, T., S. Sabate, and C. Gracia, 2010b: The importance of mesophyll conductance in regulating forest ecosystem productivity during drought periods. *Glob. Change Biol.*, **16**, 1019–1034, doi:DOI 10.1111/j.1365-2486.2009.02017.x.

Keenan, T. F. and Coauthors, 2012a: Terrestrial biosphere model performance for inter-annual variability of land-atmosphere CO2 exchange. *Glob. Change Biol.*, **18**, 1971–1987.

Keenan, T. F., E. Davidson, A. M. Moffat, W. Munger, and A. D. Richardson, 2012b: Using model-data fusion to interpret past trends, and quantify uncertainties in future projections, of terrestrial ecosystem carbon cycling. *Glob. Change Biol.*, **18**, 2555–2569.

Knorr, W., 2009: Is the airborne fraction of anthropogenic CO 2 emissions increasing? *Geophys. Res. Lett.*, **36**, 1–5, doi:10.1029/2009GL040613.

Kurz, W. A., C. C. Dymond, G. Stinson, G. J. Rampley, E. T. Neilson, A. L. Carroll, T. Ebata, and L. Safranyik, 2008: Mountain pine beetle and forest carbon feedback to climate change. *Nature*, **452**, 987–990.

Laisk, A., H. Eichelmann, V. Oja, B. Rasulov, E. Padu, I. Bichele, H. Pettai, and O. Kull, 2005: Adjustment of leaf photosynthesis to shade in a natural canopy: rate parameters. *Plant Cell Environ.*, **28**, 375–388.

Lasso, E., B. M. J. Engelbrecht, and J. W. Dalling, 2009: When sex is not enough: ecological correlates of resprouting capacity in congeneric tropical forest shrubs. *Oecologia*, **161**, 43–56.

Law, B. and Coauthors, 2002: Environmental controls over carbon dioxide and water vapor exchange of terrestrial vegetation. *Agric. For. Meteorol.*, **113**, 97–120, doi:10.1016/S0168-1923(02)00104-1.

Lewis, S. L. and Coauthors, 2009: Increasing carbon storage in intact African tropical forests. *Nature* , **457**, 1003–1006.

Lindenmayer, D. B., D. R. Foster, J. F. Franklin, M. L. Hunter, R. F. Noss, F. A. Schmiegelow, and D. Perry, 2004: Ecology-Salvage harvesting policies after natural disturbance. *Science*, **303**, 1303.

Lindroth, A., F. Lagergren, A. Grelle, L. Klemedtsson, O. Langvall, P. Weslien, and J. Tuulik, 2009: Storms can cause Europe-wide reduction in forest carbon sink. *Glob. Change Biol.*, **15**, 346–355, doi:10.1111/j.1365-2486.2008.01719.x.

Lintner, B. R., 2002: Characterizing global CO2 interannual variability with empirical orthogonal function/principal component (EOF/PC) analysis. *Geophys. Res. Lett.*, **29**, 2–5, doi:10.1029/2001GL014419.

Liu, J., Z. Ouyang, S. L. Pimm, P. H. Raven, X. Wang, H. Miao, and N. Han, 2003: Protecting China’s biodiversity. *Science*, **300**, 1240–1241.

Liu, J., S. Li, Z. Ouyang, C. Tam, and X. Chen, 2008: Ecological and socioeconomic effects of China’s policies for ecosystem services. *Proc. Natl. Acad. Sci. U. S. A.*, **105**, 9477–9482.

Liu, S. and Coauthors, 2011: Simulating the impacts of disturbances on forest carbon cycling in North America: Processes, data, models, and challenges. *J. Geophys. Res.*, **116**, G00K08, doi:10.1029/2010JG001585.

Lombardozzi, D., S. Levis, G. Bonan, and J. P. Sparks, 2012: Predicting photosynthesis and transpiration responses to ozone: decoupling modeled photosynthesis and stomatal conductance. *Biogeosciences* , **9**, 3113–3130.

Long, S. P., and C. J. Bernacchi, 2003: Gas exchange measurements, what can they tell us about the underlying limitations to photosynthesis? Procedures and sources of error. *J. Exp. Bot.*, **54**, 2393–2401, doi:10.1093/jxb/erg262.

Long, S. P., P. K. Farage, and R. L. Garcia, 1996: Measurement of leaf and canopy photosynthetic C0 2 exchange in the field 1. *J. Exp. Bot.*, **47**, 1629–1642, doi:10.1093/jxb/47.11.1629.

Luo, Y. and Coauthors, 2004: Progressive Nitrogen Limitation of Ecosystem Responses to Rising Atmospheric Carbon Dioxide. *BioScience*, **54**, 731–739, doi:10.1641/0006-3568(2004)054[0731:PNLOER]2.0.CO;2.

Luo, Y. Q. and Coauthors, 3857: A framework for benchmarking land models. *Biogeosciences*, **9**, 3857–3874.

Lyons, K. G., C. A. Brigham, B. H. Traut, and M. W. Schwartz, 2005: Rare Species and Ecosystem Functioning. *Conserv. Biol.*, **19**, 1019–1024, doi:10.1111/j.1523-1739.2005.00106.x.

Manter, D. K., and J. Kerrigan, 2004: A/Ci curve analysis across a range of woody plant species: influence of regression analysis parameters and mesophyll conductance. *J. Exp. Bot.*, **55**, 2581–2588.

Mao, J., P. E. Thornton, X. Shi, M. Zhao, and W. M. Post, 2012: Remote Sensing Evaluation of CLM4 GPP for the Period 2000–09. *J. Clim.*, **25**, 5327–5342.

McDowell, N. and Coauthors, 2008: Mechanisms of plant survival and mortality during drought: why do some plants survive while others succumb to drought? *New Phytol.*, **178**, 719–739.

Meehl, G. A. . and Coauthors, 2007: Global Climate Projections. *Climate Change 2007: The Physical Science Basis. Contribution of Working Group I to the Fourth Assessment Report of the Intergovernmental Panel on Climate Change*, Eds. S. Solomon, D. Qin, M. Manning, Z. Chen, M. Marquis, K.B. Averyt, M. Tignor, and H.L. Miller, 747–845, Cambridge University Press, Cambridge, United Kingdom and New York, NY, USA.

Mercado, L. M., N. Bellouin, S. Sitch, O. Boucher, C. Huntingford, M. Wild, and P. M. Cox, 2009: Impact of changes in diffuse radiation on the global land carbon sink. *Nature* , **458**, 1014–1017.

Miao, Z., M. Xu, R. G. Lathrop, and Y. Wang, 2009: Comparison of the A-Cc curve fitting methods in determining maximum ribulose 1.5-bisphosphate carboxylase/oxygenase carboxylation rate, potential light saturated electron transport rate and leaf dark respiration. *Plant Cell Environ.*, **32**, 109–122.

Mildrexler, D. J., M. Zhao, and S. W. Running, 2009: Testing a MODIS Global Disturbance Index across North America. *Remote Sens. Environ.*, **113**, 2103–2117, doi:10.1016/j.rse.2009.05.016.

Millward, A. A., and C. E. Kraft, 2004: Physical influences of landscape on a large-extent ecological disturbance: the northeastern North American ice storm of 1998. *Landsc. Ecol.*, **19**, 99–111, doi:10.1023/B:LAND.0000018369.41798.2f.

Miyazawa, S.-I., S. Yoshimura, Y. Shinzaki, M. Maeshima, and C. Miyake, 2008: Deactivation of aquaporins decreases internal conductance to CO2 diffusion in tobacco leaves grown under long-term drought. *Funct. Plant Biol.*, **35**, 553–564.

Montpied, P., A. Granier, and E. Dreyer, 2009: Seasonal time-course of gradients of photosynthetic capacity and mesophyll conductance to CO2 across a beech (Fagus sylvatica L.) canopy. *J. Exp. Bot.*, **60**, 2407–2418.

Nanami, S., H. Kawaguchi, R. Tateno, C. Li, and S. Katagiri, 2004: Sprouting traits and population structure of co-occurring Castanopsis species in an evergreen broad-leaved forest in southern China. *Ecol. Res.*, **19**, 341–348, doi:10.1111/j.1440-1703.2004.00643.x.

Neale, R. B. and Coauthors, 2010: Description of the NCAR Community Atmosphere Model (CAM 4 . 0). *NCAR Tech. Note*, **NCAR/TN-48**, 1–212.

Nemani, R. R., C. D. Keeling, H. Hashimoto, W. M. Jolly, S. C. Piper, C. J. Tucker, R. B. Myneni, and S. W. Running, 2003: Climate-Driven Increases in Global Terrestrial Net Primary Production from 1982 to 1999. *Science* , **300** , 1560–1563 .

Niinemets, Ü., 2007: Photosynthesis and resource distribution through plant canopies. *Plant Cell Environ.*, **30**, 1052–1071.

Niinemets, Ü., O. Kull, and J. D. Tenhunen, 1998: An analysis of light effects on foliar morphology, physiology, and light interception in temperate deciduous woody species of contrasting shade tolerance. *Tree Physiol.*, **18**, 681–696.

Niinemets, Ü., D. S. Ellsworth, A. Lukjanova, and M. Toblas, 2001: Site fertility and the morphological and photosynthetic acclimation of Pinus sylvestris needles to light. *Tree Physiol.*, **21**, 1231–1244.

Niinemets, Ü., A. Díaz-Espejo, J. Flexas, J. Galmés, and C. R. Warren, 2009a: Importance of mesophyll diffusion conductance in estimation of plant photosynthesis in the field. *J. Exp. Bot.*, **60**, 2271–2282.

Niinemets, Ü., A. Díaz-Espejo, J. Flexas, J. Galmés, and C. R. Warren, 2009b: Role of mesophyll diffusion conductance in constraining potential photosynthetic productivity in the field. *J. Exp. Bot.*, **60**, 2249–2270.

Niinemets, Ü., I. J. Wright, and J. R. Evans, 2009c: Leaf mesophyll diffusion conductance in 35 Australian sclerophylls covering a broad range of foliage structural and physiological variation. *J. Exp. Bot.*, **60**, 2433–2449.

Niinemets, Ü., J. Flexas, and J. Peñuelas, 2011: Evergreens favored by higher responsiveness to increased CO_2. *Trends Ecol. Evol.*, **26**, 136–142.

Nobel, P. S., 1977: Internal Leaf Area and Cellular CO2 Resistance: Photosynthetic Implications of Variations with Growth Conditions and Plant Species. *Physiol. Plant.*, **40**, 137–144.

Nobel, P. S., 2009: *Physicochemical and Environmental Plant Physiology*. 4th ed. Academic Press, Oxford, UK,.

Norby, R. J. and Coauthors, 2005: Forest response to elevated CO2 is conserved across a broad range of productivity 10.1073/pnas.0509478102. *Proc. Natl. Acad. Sci. U. S. A.*, **102**, 18052–18056.

Oleson, K. W. and Coauthors, 2010: Technical Description of version 4.0 of the Community Land Model (CLM). *NCAR Tech. Note*, **TN-478+STR**, 1–257.

Oliver, R. J., G. Taylor, and J. W. Finch, 2012: Assessing the impact of internal conductance to CO2 in a land-surface scheme:Measurement and modelling of photosynthesis in Populus nigra. *Agric. For. Meteorol.*, **152**, 240– 251.

Onoda, Y., K. Hikosaka, and T. Hirose, 2005a: The balance between RuBP carboxylation and RuBP regeneration: a mechanism underlying the interspecific variation in acclimation of photosynthesis to seasonal change in temperature. *Funct. Plant Biol.*, **32**, 903–910.

Onoda, Y., K. Hikosaka, and T. Hirose, 2005b: Seasonal change in the balance between capacities of RuBP carboxylation and RuBP regeneration affects CO2 response of photosynthesis in Polygonum cuspidatum. *J. Exp. Bot.*, **56**, 755–763.

Osborne, P. L., 2000: *Tropical Ecosystems and Ecological Concepts*. Cambridge University Press, Cambridge, United Kingdom,.

Pacala, S. W. and Coauthors, 2001: Consistent land- and atmosphere-based U.S. carbon sink estimates. *Science*, **292**, 2316–2320.

Page, S. E., F. Siegert, J. O. Rieley, H. D. V Boehm, A. Jaya, and S. H. Limin, 2009: The amount of carbon released from peat and forest fires in Indonesia during 1997. *Nature*, **1999**, 61–65.

Pan, Y. and Coauthors, 2011: A large and persistent carbon sink in the world’s forests. *Science*, **333**, 988–993.

Peterson, C. J., and S. T. A. Pickett, 1991: Treefall and resprouting following catastrophic windthrow in an old-growth hemlock-hardwoods forest. *For. Ecol. Manage.*, **42**, 205–217.

Phillips, O. L., S. L. Lewis, T. R. Baker, K.-J. Chao, and N. Higuchi, 2008: The changing Amazon forest. *Philos. Trans. R. Soc. B-Biol. Sci.*, **363**, 1819–1827.

Phillips, O. L. and Coauthors, 2009: Drought Sensitivity of the Amazon Rainforest. *Science* , **323** , 1344–1347.

Piao, S. and Coauthors, 2008: Net carbon dioxide losses of northern ecosystems in response to autumn warming. *Nature*, **451**, 49–52.

Piao, S., J. Fang, P. Ciais, P. Peylin, Y. Huang, S. Sitch, and T. Wang, 2009: The carbon balance of terrestrial ecosystems in China. *Nature*, **458**, 1009–1013.

Piao, S. and Coauthors, 2013: Evaluation of terrestrial carbon cycle models for their response to climate variability and to CO2 trends. *Glob. Change Biol.*, **accpted**.

Pickett, S. T. A., 1989: Space-for-time substitution as an alternative to long-term studies. *In LongTerm Studies in Ecology Approaches and Alternatives*, Ed. G.E. Likens, 110–135, Springer-Verlag.

Piel, C., E. Frak, X. Le Roux, and B. Genty, 2002: Effect of local irradiance on CO(2) transfer conductance of mesophyll in walnut. *J. Exp. Bot.*, **53**, 2423–2430.

Poorter, L., K. Kitajima, P. Mercado, J. Chubiña, I. Melgar, and H. H. T. Prins, 2010: Resprouting as a persistence strategy of tropical forest trees: relations with carbohydrate storage and shade tolerance. *Ecology*, **91**, 2613–2627.

Qian, T., A. Dai, K. E. Trenberth, and K. W. Oleson, 2006: Simulation of Global Land Surface Conditions from 1948 to 2004. Part I: Forcing Data and Evaluations. *J. Hydrometeorol.*, **7**, 953–975, doi:10.1175/JHM540.1.

Le Quéré, C. and Coauthors, 2009: Trends in the sources and sinks of carbon dioxide. *Nat. Geosci.*, **2**, 831 – 836.

Le Quéré, C., T. Takahashi, E. T. Buitenhuis, C. Rödenbeck, and S. C. Sutherland, 2010: Impact of climate change and variability on the global oceanic sink of CO2. *Glob. Biogeochem. Cycle*, **24**, 1–10.

Randerson, J. T. and Coauthors, 2006: The impact of boreal forest fire on climate warming. *Science*, **314**, 1130–1132, doi:10.1126/science.1132075.

Randerson, J. T. and Coauthors, 2009: Systematic assessment of terrestrial biogeochemistry in coupled climate–carbon models. *Glob. Change Biol.*, **15**, 2462–2484.

Roberts, M. R., 2004: Response of the herbaceous layer to natural disturbance in North American forests. *Can. J. Bot.*, **82**, 1273–1283, doi:10.1139/B04-091.

Le Roux, X., T. Bariac, H. Sinoquet, B. Genty, C. Piel, A. Mariotti, C. Girardin, and P. Richard, 2001: Spatial distribution of leaf water-use efficiency and carbon isotope discrimination within an isolated tree crown. *Plant Cell Environ.*, **24**, 1021–1032.

Running, S. W., 2008: Ecosystem disturbance, carbon, and climate. *Science*, **321**, 652–653, doi:10.1126/science.1159607.

Sabine, C. L. and Coauthors, 2004: The oceanic sink for anthropogenic CO2. *Science*, **305**, 367–371, doi:10.1126/science.1097403.

Sakaguchi, K., X. Zeng, B. J. Christoffersen, N. Restrepo-Coupe, S. R. Saleska, and P. M. Brando, 2011: Natural and drought scenarios in an east central Amazon forest: Fidelity of the Community Land Model 3.5 with three biogeochemical models. *J. Geophys. Res.*, **116**, G01029, doi:10.1029/2010JG001477.

Sarmiento, J. L., M. Gloor, N. Gruber, C. Beaulieu, A. R. Jacobson, S. E. Mikaloff Fletcher, S. Pacala, and K. Rodgers, 2010: Trends and regional distributions of land and ocean carbon sinks. *Biogeosciences*, **7**, 2351–2367, doi:10.5194/bg-7-2351-2010.

Scafaro, A. P., S. von Caemmerer, J. R. Evans, and B. J. Atwell, 2011: Temperature response of mesophyll conductance in cultivated and wild Oryzaspecies with contrasting mesophyll cell wall thickness. *Plant Cell Environ.*, **34**, 1999–2008, doi:10.1111/j.1365-3040.2011.02398.x.

Schimel, D. and Coauthors, 2000: Contribution of increasing CO2 and climate to carbon storage by ecosystems in the United States. *Science*, **287**, 2004–2006.

Schimel, D. S. and Coauthors, 2001: Recent patterns and mechanisms of carbon exchange by terrestrial ecosystems. *Nature*, **414**, 169–172.

Sellers, P. J. and Coauthors, 1996: A Revised Land Surface Parameterization (SiB2) for Atmospheric GCMS. Part I: Model Formulation. *J. Clim.*, **9**, 676–705, doi:10.1175/1520-0442(1996)009<0676:ARLSPF>2.0.CO;2.

Sellers, P. J. and Coauthors, 1997: Modeling the Exchanges of Energy, Water, and Carbon Between Continents and the Atmosphere. *Science*, **275**, 502–509, doi:10.1126/science.275.5299.502.

Shao, Q., L. Huang, J. Liu, W. Kuang, and J. Li, 2011: Analysis of forest damage caused by the snow and ice chaos along a transect across southern China in spring 2008. *J. Geogr. Sci.*, **21**, 219–234, doi:10.1007/s11442-011-0840-y.

Sharkey, T. D., 1985: Photosynthesis in intact leaves of C3 plants: Physics, physiology and rate limitations. *Bot. Rev.*, **51**, 53–105, doi:10.1007/BF02861058.

Sharkey, T. D., 2012: Mesophyll conductance: constraint on carbon acquisition by C3 plants. *Plant Cell Environ.*, **35**, 1881–1883.

Sharkey, T. D., C. J. Bernacchi, G. D. Farquhar, and E. L. Singsaas, 2007: Fitting photosynthetic carbon dioxide response curves for C(3) leaves. *Plant Cell Environ.*, **30**, 1035–1040.

Sinclair, T. R., J. Goudriaan, and C. T. de Wit, 1977: Mesophyll resistance and CO2 compensation concentration in leaf photosynthesis models. *Photosynthetica*, **11**, 56–65.

Sitch, S. and Coauthors, 2010: Evaluation of the terrestrial carbon cycle, future plant geography and climate-carbon cycle feedbacks using five Dynamic Global Vegetation Models (DGVMs). *Glob. Change Biol.*, **14**, 2015–2039.

Sokolov, A. P., D. W. Kicklighter, J. M. Melillo, B. S. Felzer, C. A. Schlosser, and T. W. Cronin, 2008: Consequences of Considering Carbon–Nitrogen Interactions on the Feedbacks between Climate and the Terrestrial Carbon Cycle. *J. Clim.*, **21**, 3776–3796, doi:10.1175/2008JCLI2038.1.

Solomon, S., G.-K. Plattner, R. Knutti, and P. Friedlingstein, 2009: Irreversible climate change due to carbon dioxide emissions. *Proc. Natl. Acad. Sci. U. S. A.*, **106**, 1704–1709, doi:10.1073/pnas.0812721106.

Stephens, B. B. and Coauthors, 2007: Weak Northern and Strong Tropical Land Carbon Uptake from Vertical Profiles of Atmospheric CO2 10.1126/science.1137004. *Science*, **316**, 1732–1735.

Sun, Y., L. Gu, and R. E. Dickinson, 2012a: A numerical issue in calculating the coupled carbon and water fluxes in a climate model. *J. Geophys. Res.*, **117**, D22103.

Sun, Y., L. Gu, R. E. Dickinson, and B. Zhou, 2012b: Forest greenness after the massive 2008 Chinese ice storm: integrated effects of natural processes and human intervention. *Environ. Res. Lett.*, **7**, 035702, doi:10.1088/1748-9326/7/3/035702.

Syvertsen, J. P., J. . Lloyd, C. McConchie, P. E. Kriedemann, and G. D. Farquhar, 1995: On the relationship between leaf anatomy and CO2 diffusion through the mesophyll of hypostomatous leaves. *Plant Cell Environ.*, **18**, 149–157.

Tang, Z., Z. Wang, C. Zheng, and J. Fang, 2006: Biodiversity in China's mountains. *Front. Ecol. Environ.*, **4**, 347–352, doi:10.1890/1540-9295(2006)004[0347:BICM]2.0.CO;2.

Terashima, I., Y. T. Hanba, Y. Tazoe, P. Vyas, and S. Yano, 2006: Irradiance and phenotype: comparative eco-development of sun and shade leaves in relation to photosynthetic CO2 diffusion. *J. Exp. Bot.*, **57**, 343–354.

Tholen, D., and X.-G. Zhu, 2011: The Mechanistic Basis of Internal Conductance: A Theoretical Analysis of Mesophyll Cell Photosynthesis and CO2 Diffusion. *Plant Physiol.*, **156**, 90–105.

Tholen, D., G. Ethier, B. Genty, S. Pepin, and X.-G. Zhu, 2012: Variable Mesophyll Conductance Revisited. Theoretical Background and Experimental Implications. *Plant Cell Environ.*, **35**, 2087–2103, doi:10.1111/j.1365-3040.2012.02538.x.

Thompson, J. R., T. A. Spies, and L. M. Ganio, 2007: Reburn severity in managed and unmanaged vegetation in a large wildfire. *Proc. Natl. Acad. Sci. U. S. A.*, **104**, 10743–10748.

Thornton, P. E. and Coauthors, 2009: Carbon-nitrogen interactions regulate climate-carbon cycle feedbacks: results from an atmosphere-ocean general circulation model. *Biogeosciences*, **6**, 2099–2120, doi:10.5194/bg-6-2099-2009.

Tilman, D., 1996: Biodiversity: population versus ecosystem stability. *Ecology*, **77**, 350–363, doi:10.2307/2265614.

Turner, M. G., 2010: Disturbance and landscape dynamics in a changing world. *Ecology*, **91**, 2833–2849.

Turner, M. G., and V. H. Dale, 1998: Comparing large, infrequent disturbances: what have we learned? *Ecosystems*, **1**, 493–496.

Violle, C., Z. Pu, and L. Jiang, 2010: Experimental demonstration of the importance of competition under disturbance. *Proc. Natl. Acad. Sci. U. S. A.*, **107**, 12925–12929.

Wang, Y. P., R. M. Law, and B. Pak, 2010: A global model of carbon, nitrogen and phosphorus cycles for the terrestrial biosphere. *Biogeosciences*, **7**, 2261–2282.

Wang, Y.-P., C. M. Trudinger, and I. G. Enting, 2009: A review of applications of model–data fusion to studies of terrestrial carbon fluxes at different scales. *Agric. For. Meteorol.*, **149**, 1829–1842, doi:10.1016/j.agrformet.2009.07.009.

Warren, C. R., 2008: Stand aside stomata, another actor deserves centre stage: the forgotten role of the internal conductance to CO(2) transfer. *J. Exp. Bot.*, **59**, 1475–1487, doi:Doi 10.1093/Jxb/Erm245.

Warren, C. R., and E. Dreyer, 2006: Temperature response of photosynthesis and internal conductance to CO2: results from two independent approaches. *J. Exp. Bot.*, **57**, 3057–3067, doi:Doi 10.1093/Jxb/Erl067.

Warren, C. R., E. Dreyer, and M. A. Adams, 2003: Photosynthesis-Rubisco relationships in foliage of Pinus sylvestris in response to nitrogen supply and the proposed role of Rubisco and amino acids as nitrogen stores. *Trees*, **17**, 359–366.

Warren, C. R., M. Low, R. Matyssek, and M. Tausz, 2007: Internal conductance to CO2 transfer of adult Fagus sylvatica: Variation between sun and shade leaves and due to free-air ozone fumigation. *Environ. Exp. Bot.*, **59**, 130–138, doi:10.1016/j.envexpbot.2005.11.004.

Welp, L. R. and Coauthors, 2011: Interannual variability in the oxygen isotopes of atmospheric CO2 driven by El Niño. *Nature*, **477**, 579–582, doi:10.1038/nature10421.

Williams, M. and Coauthors, 1996: Modelling the soil-plant-atmosphere continuum in a Quercus-Acer stand at Harvard Forest: the regulation of stomatal conductance by light, nitrogen and soil/plant hydraulic properties. *Plant Cell Environ.*, **19**, 911–927, doi:10.1111/j.1365-3040.1996.tb00456.x.

Wullschleger, S. D., 1993: Biochemical Limitations to Carbon Assimilation in C 3 Plants—A Retrospective Analysis of the A/C i Curves from 109 Species. *J. Exp. Bot.*, **44**, 907–920, doi:10.1093/jxb/44.5.907.

Xia, J., Y. Luo, Y.-P. Wang, and O. Hararuk, 2013: Traceable components of terrestrial carbon storage capacity in biogeochemical models. *Glob. Change Biol.*, **Accepted**.

Xu, C., R. Fisher, S. D. Wullschleger, C. J. Wilson, M. Cai, and N. G. McDowell, 2012: Toward a Mechanistic Modeling of Nitrogen Limitation on Vegetation Dynamics. *PLoS ONE*, **7**, e37914.

Xu, L., A. Samanta, M. H. Costa, S. Ganguly, R. R. Nemani, and R. B. Myneni, 2011: Widespread decline in greenness of Amazonian vegetation due to the 2010 drought. *Geophys. Res. Lett.*, **38**, L07402, doi:10.1029/2011GL046824.

Yamori, W., K. Noguchi, Y. T. Hanba, and I. Terashima, 2006: Effects of internal conductance on the temperature dependence of the photosynthetic rate in spinach leaves from contrasting growth temperatures. *Plant Cell Physiol.*, **47**, 1069–1080.

Yang, X., T. K. Richardson, and A. K. Jain, 2010: Contributions of secondary forest and nitrogen dynamics to terrestrial carbon uptake. *Biogeosciences*, **7**, 3041–3050.

Yin, X., P. C. Struik, P. Romero, J. Harbinson, J. B. Evers, P. E. L. Van Der Putten, and J. Vos, 2009: Using combined measurements of gas exchange and chlorophyll fluorescence to estimate parameters of a biochemical C-3 photosynthesis model: a critical appraisal and a new integrated approach applied to leaves in a wheat (Triticum aestivum) canopy . *Plant Cell Environ.*, **32**, 448–464.

Zaehle, S., and D. Dalmonech, 2011: Carbon–nitrogen interactions on land at global scales: current understanding in modelling climate biosphere feedbacks. *Curr. Opin. Environ. Sustain.*, **3**, 311–320.

Zaehle, S., P. Friedlingstein, and A. D. Friend, 2010a: Terrestrial nitrogen feedbacks may accelerate future climate change. *Geophys. Res. Lett.*, **37**, 1–5, doi:10.1029/2009GL041345.

Zaehle, S., A. D. Friend, P. Friedlingstein, F. Dentener, P. Peylin, and M. Schulz, 2010b: Carbon and nitrogen cycle dynamics in the O-CN land surface model: 2. Role of the nitrogen cycle in the historical terrestrial carbon balance. *Glob. Biogeochem. Cycle*, **24**, GB1006, doi:10.1029/2009GB003522.

Zeng, H., J. Q. Chambers, R. I. Negrón-Juárez, G. C. Hurtt, D. B. Baker, and M. D. Powell, 2009: Impacts of tropical cyclones on U.S. forest tree mortality and carbon flux from 1851 to 2000. *Proc. Natl. Acad. Sci. U. S. A.*, **106**, 7888–7892.

Zeng, W., G. S. Zhou, B. R. Jia, Y. L. Jiang, and Y. Wang, 2010: Comparison of parameters estimated from A/Ci and A/Cc curve analysis. *Photosynthetica*, **48**, 323–331.

Zhang, Q., Y. P. Wang, A. J. Pitman, and Y. J. Dai, 2011: Limitations of nitrogen and phosphorous on the terrestrial carbon uptake in the 20th century. *Geophys. Res. Lett.*, **38**, 1–5, doi:10.1029/2011GL049244.

Zhang, X., M. A. Friedl, C. B. Schaaf, A. H. Strahler, J. C. F. Hodges, F. Gao, B. C. Reed, and A. Huete, 2003: Monitoring vegetation phenology using MODIS. *Remote Sens. Environ.*, **84**, 471–475, doi:10.1016/S0034-4257(02)00135-9.

Zhao, M., and S. W. Running, 2010: Drought-Induced Reduction in Global Terrestrial Net Primary Production from 2000 Through 2009. *Science*, **329**, 940–943, doi:10.1126/science.1192666.

Zhou, B. and Coauthors, 2011a: Impact of the 2008 ice storm on moso bamboo plantations in southeast China. *J. Geophys. Res.*, **116**, G00H06, doi:10.1029/2009JG001234.

Zhou, B. and Coauthors, 2011b: The Great 2008 Chinese Ice Storm: Its Socioeconomic–Ecological Impact and Sustainability Lessons Learned. *Bull. Amer. Meteorol. Soc.*, **92**, 47–60, doi:10.1175/2010BAMS2857.1.

Vita

Ying Sun was born in Yangquan, Shanxi, China. She earned the B.S. in Remote Sensing from Beijing Normal University, Beijing, China in 2008. Then she joined the University of Texas at Austin. She will continue as a scientist in academia.

Permanent address: No. 28 Dalian Road, Yangquan, Shanxi, China, 045000
This dissertation was typed by the author.